1989

Secondary Ion Mass Spectrometry And Its Application To Studies In Geochemistry

Ian Joseph Muir

NOTICE

The quality of this microform is heavily dependent upon the quality of the original thesis submitted for microfilming. Every effort has been made to ensure the highest quality of reproduction possible.

If pages are missing, contact the university which granted the degree.

Some pages may have indistinct print especially if the original pages were typed with a poor typewriter ribbon or if the university sent us an inferior photocopy.

Reproduction in full or in part of this microform is governed by the Canadian Copyright Act, R.S.C. 1970, c. C-30, and subsequent amendments.

AVIS

La qualité de cette microforme dépend grandement de la qualité de la thèse soumise au microfilmage. Nous avons tout fait pour assurer une qualité supérieure de reproduction.

S'il manque des pages, veuillez communiquer avec l'université qui a conféré le grade.

La qualité d'impression de certaines pages peut laisser à désirer, surtout si les pages originales ont été dactylographiées à l'aide d'un ruban usé ou si l'université nous a fait parvenir une photocopie de qualité inférieure.

La reproduction, même partielle, de cette microforme est soumise à la Loi canadienne sur le droit d'auteur, SRC 1970, c. C-30, et ses amendements subséquents.

SECONDARY ION MASS SPECTROMETRY AND ITS APPLICATION TO STUDIES IN GEOCHEMISTRY

by

Ian Joseph Muir

Department of Chemistry

Submitted in partial fulfillment
of the requirements for the degree of
Doctor of Philosophy

Faculty of Graduate Studies
The University of Western Ontario
London, Ontario
January, 1989

ISBN 0-315-49331-3

ABSTRACT

Secondary ion mass spectrometry (SIMS) with specimen isolation conditions (an extreme form of energy filtering) is useful in geochemical studies. The presence of molecular ion interferences in SIMS spectra is greatly reduced when analyzing high energy secondary ions (i.e. specimen isolation conditions), thus simplifying the interpretation of mass spectra.

High energy secondary ions were found to be less susceptible to the dramatic changes in ionization yield reulting from the effect of the matrix in secondary ion production. Correlation of ion intensities for glass and crystalline materials of identical composition is possible for most elements when using some form of energy filtering, and thus the use of glass standards for SIMS analysis of minerals is possible. Some matrix effects are still present in the high energy ion population. However, in a given concentration range with a reliable set of standards, quantitative analysis down to the ppm level is available with specimen isolation or conventional energy filtering methods. This has been demonstrated for the rare-earth elements at both trace and major element concentration levels in various mineral grains.

The ionization probability of high energy ions was studied as a function of kinetic energy, first ionization potential, and oxide bond strength. A simple mechanism for the production of high energy secondary ions could not be obtained from these results.

Besides the elimination of molecular ion interferences, the method of specimen isolation is an excellent technique for the analysis of non-conducting samples. Leached, or altered zones up to several hundreds of angstroms in thickness have been observed in SIMS depth profiles of naturally and laboratory dissolved plagioclase. Dissolution of plagioclase in relatively simple laboratory experiments (pH 3.5 and 5.7) forms altered zones depleted of sodium, calcium and aluminum, and enriched (residually) in silicon. For specimens undergoing a more complex set of reactions (dissolution in nature), layers enriched in aluminum were observed in the SIMS profiles. Each of these layers are believed to form during the dissolution process. Qualitatively similar results were obtained using X-ray photoelectron spectroscopy, while SEM analysis has shown the sample surfaces to be "clean" and free of secondary precipitates.

ACKNOWLEDGEMENTS

I would like to thank my research supervisor, Prof. G.M. Bancroft, for his enthusiasm, encouragement and insight throughout the course of this work. I am also grateful for the occasional tennis lesson.

Special thanks go to Prof. H.W. Nesbitt (Dept. of Geology) for his comments and suggestions during the latter stages of this thesis.

I would also like to thank Darlene Johnston, Jim Metson, and Bill Chauvin for the valuable lessons on the operation of the CAMECA (SIMS) instrument. Special thanks are also extended to Dietmar Fichter for keeping the instrument up and running. Prof. N.S. McIntyre and his staff at Surface Science Western have also made important contributions throughout the course of this study.

Prof. N.D. MacRae (Dept. of Geology) kindly supplied the augite analyses presented in chapter 4. Prof. J.B. Metson (University of Auckland) and his graduate student D.L. Tui were responsible for fitting the experimental data presented in chapter 3.

Leighton Coatsworth's one on one seminars were greatly appreciated. The inside workings of high vacuum instruments now seem somewhat clearer to me.

Special thanks go to Prof. R.R. Martin and Dr. Bill Shotyk for their friendship and helpful discussions. I would also like to acknowledge the other members of the research group for their help and friendship. John Bozek, Steve Bushby, Margaret Hyland, Brian Yates, Ralph Jonasson, Lisa Dignard-Bailey, Dong Sheng Yang, Jeff Cutler, Jamie Price, Jo-Ann Bice, Jay Mycroft, Dr. Masoud Kasrai and Zhifeng Liu have all contributed to many good times. I wish you all well.

I am grateful to Anne Leaist and Suzanne Boatman for helping me along with my typing, and the printing of this thesis.

I would also like to acknowledge the support and friendship of the many friends and co-workers associated with the Department of Chemistry who have been the source of many enjoyable moments over the past five years.

Part of this work was made possible through scholarships from the Ontario government and the University of Western Ontario. A portion of the instrument costs were met by the Ontario Ministry of the Environment (grant to Prof. H.W. Nesbitt). I also extend my appreciation to all of those who donated specimens along the way. These people have been mentioned thorughout the course of the text.

Finally, I owe a great deal of thanks to my father, Lachlan Muir, who has been very supportive throughout the course of this work. This thesis is dedicated to you Dad.

TABLE OF CONTENTS

LIST OF TABLES

LIST OF FIGURES

PART I

CHAPTER 1

INTRODUCTION TO SECONDARY ION MASS SPECTROMETRY

1.1 Introduction

Secondary ion mass spectrometry (SIMS) is an analytical technique based upon the collection and mass analysis of charged atomic and/or molecular species resulting from the sputtering process. Sputtering of surface material is one of the many processes occurring during bombardment of a target material by an energetic (on the order of a few keV) particle (ion or neutral) beam.[1]

The incoming primary particles (in this study ions) impart energy and momentum to the sample surface, leading to changes in the lattice structure and loss of surface material. The emitted surface material is composed of charged, and uncharged (and possibly some in excited states) surface particles, both atomic and molecular in nature, as well as photons and electrons. Secondary ions are defined as all those ionized surface particles in both the ground and excited states.[1] The SIMS technique is based upon the separation and analysis of these secondary ions (see Figure 1.1-1). The secondary ions observed carry information regarding both the elemental and isotopic nature of the surface from which they originate.

Figure 1.1-1

Principles of the SIMS technique.

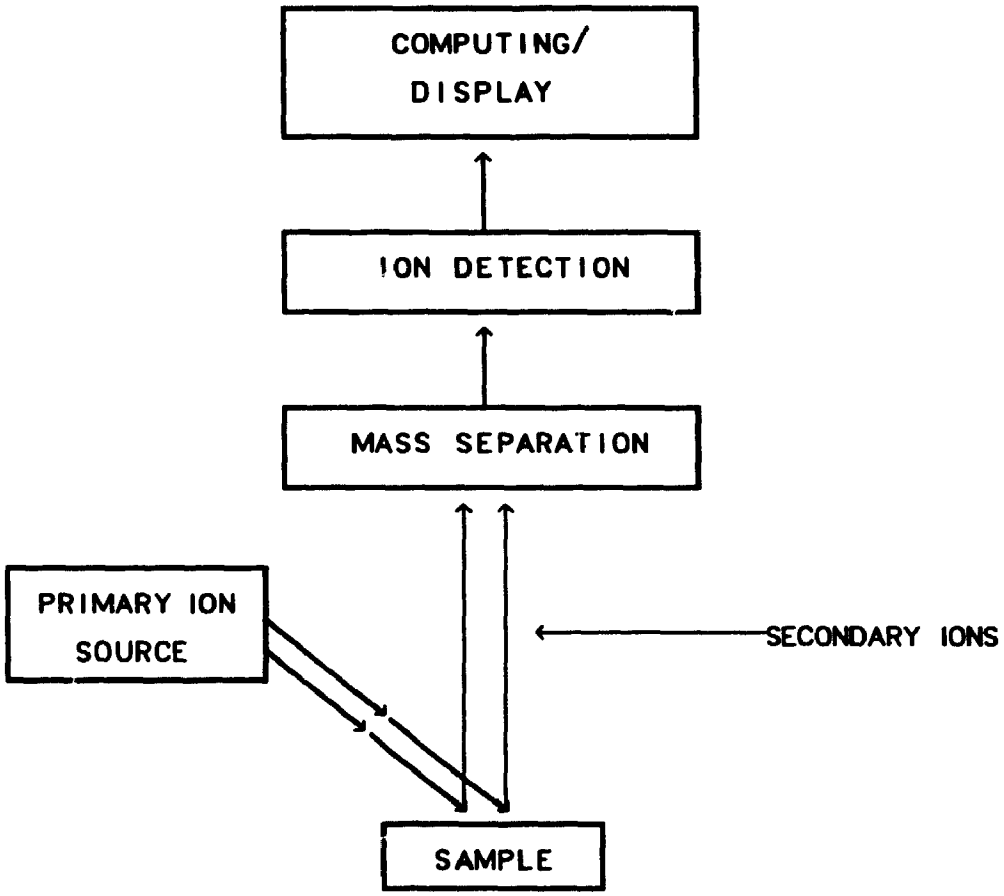
COMPUTING/
DISPLAY
ION DETECTION
MASS SEPARATION
PRIMARY ION
SOURCE
SECONDARY IONS
SAMPLE

One of the major advantages of the SIMS technique is that almost all of the secondary ion population originates from the upper few atomic layers of the analyzed surface, making SIMS a technique with excellent surface sensitivity. It is important to note however, that a vast majority of the sputtered surface particles are uncharged, while only a few percent are ionized. This leads to problems in the interpretation of spectra since changes in the ionization yields of up to a few orders of magnitude often result from changes in the chemical environment of the target material.[2,3]

1.2 Historical Background

In 1910 Sir Joseph John Thomson became the first to observe and identify secondary ions. In his experiments with "Canalstrahlen", Thomson reported that: "I had occasion in the course of the work to investigate the secondary Canalstrahlen produced when primary Canalstrahlen strike against a metal plate. I found that the secondary rays which were emitted in all directions were for the most part uncharged, but that a small fraction carried a positive charge."[4]

The first known negative secondary ion spectra were recorded by Woodcock[5] and Thompson[6] in 1931. These spectra were obtained by bombarding NaF and CaF_2 targets with 500 eV Li^+ primary ions. In 1936 and 1937, Arnot and Milligan[7,8]

reported the formation of negative secondary ions from positive primary ions.

The next major advance towards a SIMS instrument as we know it today was not until 1949 when Herzog and Viehöck[9] published a paper regarding the use of electric fields to accelerate the primary and secondary ions. It was approximately 10 years later that the next generation of secondary ion mass spectrometers was constructed. Honig[10] (1958) was the first to build a complete secondary ion mass spectrometer. Shortly after the construction of Honig's instrument there were a number of reports of other instruments,[11-15] and the field of secondary ion mass spectrometry began to grow rapidly.

The first commercially available SIMS instruments were built by Liebl and Herzog[16] in 1963. The purpose of this instrument was to be able to analyze for isotopic variations and spatial distributions for the complete periodic table of the elements. This instrument evolved into three basic types of instruments. Firstly there are the mass analyzers with moderate (<10 μm) lateral resolution.[9,10,15-18] These systems are generally used for trace element analysis and depth profiling. The primary ion current densities used for these types of analysis are usually on the order of $>10^{-6}$ A cm^{-2}. This mode of operation is referred to as "Dynamic SIMS." "Static SIMS", which uses much lower primary current densities is a powerful tool for surface analysis. Development of static

SIMS by Benninghoven[19] and the application of static SIMS to organic materials has lead to the development of "Organic SIMS" by Benninghoven and co-workers.[20]

The other two forms of SIMS instruments deal with higher lateral resolution (0.02 to 10 μm). These two forms are the ion microscope and the ion microprobe. The ion microscope[21-23] uses a defocussed primary ion beam in conjunction with secondary optics and mass analysis to form a high spatial resolution (~1 μm) magnified image of the specimen. In the case of the ion microprobe,[24] a finely focussed primary ion beam (formed from a duoplasmatron) and a mass analyzer are used to obtain spatial resolution on the order of 1 μm. Better resolution has been obtained by improvements in primary ion sources. The development of liquid metal ion sources,[25,26] has lead to ion beams with a lateral resolution in the range of 20 nm to 0.1 μm.

A detailed account of the history and development of secondary ion mass spectrometry may be found in articles by Liebl,[27] Robinson[28] and Honig.[29]

1.3 Applications of SIMS to Geochemistry and Cosmochemistry

1.3.1 General Applications

The application of SIMS to geochemistry and cosmochemistry has been discussed by many authors. For example, see references 30 to 39 and the references within. Analysis of trace elements in both lunar and terrestrial

materials has been the more publicized use of the ion microprobe. Other applications, such as isotopic analysis of both terrestrial and extraterrestrial materials, and the analysis of light elements (hydrogen to fluorine) in minerals have also been widely publicized. Some accounts of diffusion studies in minerals have also been documented.

The attractive features of SIMS for the geochemist are: 1) a complete mass range analysis from hydrogen to uranium; 2) micron scale resolution; and 3) detection limits down to the sub-ppm level with six or seven orders of magnitude range for most elements.[31,35] The practical application of secondary ion mass spectrometry to the earth sciences has met with some difficulties due to the complex nature of the samples analyzed and the sputtering process. Serious problems such as a plethora of complex molecular and multiply charged species[31] that obscure the observation of singly charged elemental ions, and the strong influence of the target matrix on the production of secondary ions[2,3] have made the interpretation of SIMS spectra of mineral specimens somewhat difficult.

1.3.2 Molecular Ion Suppression

The suppression of molecular ions is typically done by either high mass resolution[40] or kinetic energy filtering (see references 32, 35, 41 and 59). High mass resolution is based upon the mass defect between elemental and molecular ions. When tuning SIMS instruments for high mass resolution

conditions, a drop in secondary ion intensity is always observed. Kinetic energy filtering uses the differences in the kinetic energy distributions between the molecular and elemental ions in order to eliminate molecular ions from the mass spectra. Even though the signal from the elemental ions is reduced when using energy filtering techniques, the reduction of the molecular ion intensity is far greater (see section 1.6 and the figures within). The result is an increased elemental to molecular ion ratio. Both methods of molecular ion suppression have been used with a large degree of success.

In general, high mass resolution is most beneficial for the analyses of light elements, whereas kinetic energy filtering methods are preferred for the analyses of heavier elements (and hence a complete mass range analysis). The mass resolution necessary to resolve some of the interferences at high mass numbers would in turn be accompanied by a severe loss of secondary ion intensity. For a more complete description of kinetic energy filtering techniques the reader is referred to section 1.6 and references 32, 35, 41 and 59.

1.3.3 Surface Contamination

Specimens for SIMS analysis are generally required to have smooth flat surfaces such that the yield of sputtered material will be a maximum. Geologic specimens for the ion probe are usually in the form of highly polished thin

sections or thick slabs. For surface analysis, clean sample surfaces are required. Sources of surface contamination are: 1) the polishing process; 2) the condensation of material onto the surface from the laboratory atmosphere and/or the vacuum system of the instrument. These types of problems are usually avoided by precleaning the area of analysis (or a slightly larger area) using the primary ion beam to erode away several hundred angstroms of the sample surface. This precleaning step is not applicable in cases where surface analysis studies are a priority.

1.3.4 Analysis of Insulating Materials

Another potential problem with the analysis of geologic materials arises from to the insulating nature of most mineral specimens. Specimens for analysis are usually given a conductive metal coating (~20 to 30 nm thickness) to prevent the buildup of electrical charge. However, once the metal layer has been sputtered away, the potential at the uncovered surface (i.e. the point of analysis) is somewhat different from that of the conductive coating. This can lead to variations in the extraction efficiency of secondary ions from point to point in the analysis. The buildup of electric charge at the point of analysis can also cause instability such that the extraction of secondary ions is again altered, and in some instances the analysis site may be lost. While some instruments flood the analysis area with low energy electrons to help stabilize charge buildup

on insulating samples, the use of negatively charged primary ion beams is generally favoured for geochemical analysis. Andersen et al.[42] propose that the incoming negative charge from the primary beam is stabilized by the outgoing secondary electrons. Others prefer to use positive primary beams when extracting positive secondary ions and negative primary beams for negative secondary ions so that sample charging may be controlled by adjustment of the primary beam current such that the incoming charge is balanced by the outgoing charge.[38]

When exposing the specimen to the primary beam for analysis there is also a rise in temperature at the sample surface. The rise in temperature at the point of analysis will be dependent on such factors as the thermal conductivity of the specimen and the primary ion current density. If the temperature at the point of analysis becomes high enough some of the volatile elements will be lost. This has been reported for glasses with high Na_2O concentrations by Lovering.[30] This effect is presumably similar to that observed in electron probe analyses of sodium rich specimens.[43]

1.3.5 Analytical Considerations

In any type of SIMS analysis it is generally favorable to work with a stable high level of sputtered ion intensity. Reactive species such as oxygen and cesium have

been favoured for use as primary ion beams over inert gases such as argon. Use of these reactive species leads to stable, high secondary ion intensities through the formation of surface compounds (for example, oxides).[44,45] When using electronegative gases such as oxygen, the production of positive secondary ions is increased. The effect of the electronegative species is to increase the electronic work function necessary for the electrons to escape the surface. This in turn leads to greater emission of positive ions. The converse of this also holds true for the enhancement of negative secondary ions when using electropositive species (i.e. cesium) to bombard the surface. Since elements that readily form positive ions are generally of interest to geochemists, primary ion beams of oxygen are most widely used.[31,44,45]

Due to the complex chemistry of many mineral specimens the resulting secondary ion spectra are often quite complex. The secondary ion mass spectra commonly contain peaks at each and every mass position through the mass range 0 to 250.[31] The use of reactive primary ion beams will generally reduce the number of molecular ions, however not all molecular species are extinguished. Instruments with low mass resolving powers (M/ΔM) experience more problems with molecular ion contaminants. Selected vacuum pumping to reduce the hydrogen contamination in the sample chamber and mass filtering of the primary ion source

also aid in the reduction of molecular ion interferences.[31] Methods of molecular ion suppression have been discussed earlier.

1.4 Quantification of SIMS Data

1.4.1 Factors Affecting Quantification

The attractive features of the SIMS technique make it an excellent choice for acquiring qualitative or semiquantitative analyses of surfaces. However, the inability to correlate secondary ion intensities with the chemical composition of the surface in the form of a quantitative analysis is the major drawback of the SIMS technique. Many factors contribute to the difficulty of obtaining quantitative SIMS analyses. The general approach to a quantitative analysis is first, the interpretation of the spectrum, and second, the quantification of that spectrum.[1] Spectral interpretation involves the assignment of peaks and/or portions of peak intensities to elemental and molecular ions. Quantification of the spectrum is the calculation of elemental concentrations from the elemental (isotopic) and sometimes molecular ion intensities.

Matrix effects have been found to have the greatest effect on secondary ion intensities.[2,3] The ionization probability of certain elements may change by as much as a few orders of magnitude depending on the chemical nature of the host matrix. For a binary alloy A-B, the increasing presence of the species (for instance A) that forms the

stronger oxide bond will enhance the ionization of B, while the ionization of A is depressed by the increasing presence of B.[46-48]

Crystallographic orientation of the specimens and the impact angle of the primary ion beam[1] have been found to have an effect on the yield of sputtered material. This makes the comparison of absolute secondary ion intensities from standards to unknown specimens somewhat difficult. Referencing the ion intensities to an "internal reference" (i.e. one of the more intense elemental ion signals in the spectrum) will reduce problems when comparing ion intensities from the sample with the standards.

Coverage of the specimen surface by reactive species will also affect the yield of secondary ions[1]. Similar to using an oxygen primary ion beam for improved secondary ion production, flooding of the sample surface with oxygen gas to enhance and stabilize the yield of positive secondary ions is common.

There is also a mass dependence on the transmission of the mass spectrometer that must be taken into consideration for quantitative analysis[1]. This results in isotopic fractionation (i.e. the isotope effect) of the elements within the SIMS instrument. Thus, certain corrections for the fractionation of isotopes must be made when calculating elemental compositions from isotopic intensities in the secondary ion spectra. This is also an

important consideration in studies of the isotopic composition of various materials.

Other factors such as the angle of emission of the detected secondary ions,[1] the energy bandpass of the spectrometer[1] and the residual gas pressure around the primary beam/specimen interaction area[1] must also be considered if one desires a quantitative analysis. As a final commment on the quantification of SIMS data, the properties of the detection system such as the detector background and the detector dead-time must also be understood.[31]

1.4.2 Approaches to Quantification

For geologic analysis, one of the more common methods for obtaining quantitative information is through the use of calibration curves. When using standards of matching chemical composition (major element chemistry) and an exact set of standardized operating conditions it becomes possible to extract quantitative information from the secondary ion mass spectra. In these analyses it may also be necessary to account for the isotope effect.[49,50] If the calibration curves are linear, as is the case for small ranges in concentration, the use of calibration curves may be extended to "relative sensitivity factors."[50,51] Knowing the ionization yield of a certain element (A) with respect to a reference element (R) in the same matrix simplifies the determination of elemental concentrations. In this case,

the ratio of the two ion intensities (both A^+ and R^+) is measured and the concentration of the reference element must be known from previous (other methods) determinations.

Another method of avoiding the influence of matrix effects in deriving quantitative information is the use of implanted standards.[53-55] In this instance, an isotope of the element of interest (assume that two or more isotopes are present) is implanted into the specimen at a known dose. By measuring the signals of the implanted (known) and unknown isotope(s) and making corrections for the isotopic fractionation due to the instrument, quantification of the element of interest is possible. For example, the determination of potassium in plagioclase minerals using $^{41}K^+$ as the implant and $^{39}K^+$ as the unknown has been reported by Striet et al.[53] Using ^{107}Ag as the implanted isotope, Chryssoulis et al.[54] have made determinations of silver in sulphide minerals down to the ppb level. For monoisotopic elements this exact procedure is not applicable. However, measuring the signal from the implant (same mass as the element) against the background level of the element (unknown) will lead to quantitative measurements of these elements. The determination of gold in sulphide ores in the sub-ppm range has been performed by Chryssoulis et al.[55]

Another to quantitative analysis is the use of ionization models. One such example is the "Local Thermal Equilibrium Theory" (LTE) presented in 1970 by Andersen and

Hinthorne.[45,56,57] The LTE theory assumes that the sputtering source is a dense plasma containing positive and negative ions, neutral atoms and oxide molecules (an $^{16}O^-$ primary ion beam is used) all in thermodynamic equilibrium. Using the intensities of the singly charged positive secondary ions, it is possible to calculate the surface composition (i.e. that of the sputtering source) if the temperature (T), electron density (N_e) and the free oxygen concentration in the plasma are known.[31,45,56,57] The application of the LTE theory to mineral analysis is discussed in reference 31 and the references within.

1.5 The CAMECA IMS 3f Secondary Ion Microscope

All of the SIMS data obtained during the course of this work (parts I and II) were obtained using a CAMECA IMS 3f Secondary Ion Microscope. The CAMECA instrument was housed and maintained at the Surface Science Western Laboratory located on the campus of the University of Western Ontario. Besides operation as an ion microscope, the IMS 3f may also be operated as an ion microprobe as was the case for this study. The IMS 3f is an electrostatic sector/magnetic sector instrument with a double focussing geometry, thus making it capable of both high mass resolution ($M/\Delta M$ ~10,000) and kinetic energy filtering of secondary ions. The CAMECA IMS 3f instrument (see Figure 1.5-1) was introduced in 1980 by Rouberol et al.[23]

Other descriptions of the IMS 3f are found in references 1 and 58.

Two primary ion sources are available on the IMS 3f. A hollow cathode duoplasmatron source is used to produce primary beams of O^-, O_2^+, Ar^+ and Xe^+ for the study of electropositive elements (other gases have been tried by other research groups). For the study of electronegative elements, a Cs^+ ion source (liquid metal ion source) is also available. After acceleration (typically to 5 to 20 kV), the primary beam is mass filtered by the primary magnet and directed into the primary ion column (see Figure 1.5-1). The primary beam mass filter is a magnet set up with two entrance ports (one for each source) and a common exit port at the entrance to the primary column. In the primary column there are three electrostatic lenses used to focus the beam to a spot a few to a few hundred microns in diameter on the sample surface. As an option to the analyst, raster plates permit the rastering of the primary beam over the sample surface.

The secondary ions (either positive of negative) are extracted from the specimen using a potential difference (i.e. the secondary accelerating voltage) of ±4.5 kV between the specimen holder and the "immersion lens." The secondary ions are then focussed to the entrance of the spectrometer by the "transfer optics." Secondary ion kinetic energies are analyzed by a 90°, 86 mm radius electrostatic analyzer (ESA 1) tuned to 4500 eV. The electrostatic analyzer is

Figure 1.5-1

The CAMECA IMS 3f secondary ion microscope.

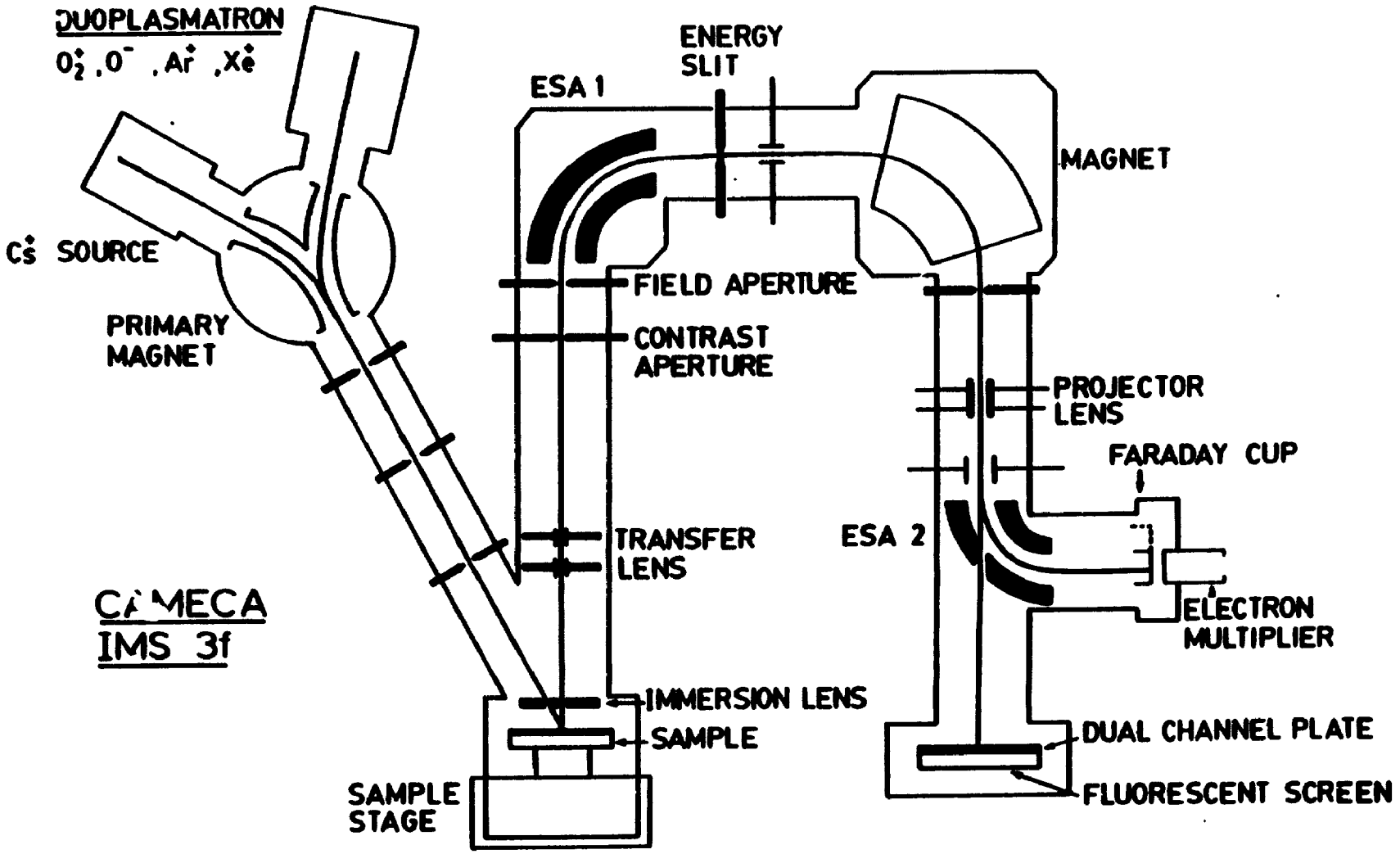
DUOPLASMATRON
O_2^+ , O^- , Ar^+ , Xe^+
Cs^+ SOURCE
PRIMARY MAGNET
ENERGY SLIT
ESA 1
MAGNET
FIELD APERTURE
CONTRAST APERTURE
PROJECTOR LENS
FARADAY CUP
TRANSFER LENS
ESA 2
ELECTRON MULTIPLIER
CAMECA IMS 3f
IMMERSION LENS
SAMPLE
DUAL CHANNEL PLATE
SAMPLE STAGE
FLUORESCENT SCREEN

coupled to a variable energy window referred to as the "energy slit." For the passage of secondary ions through the electrostatic analyzer the following equation must be satisfied:

$$\frac{1/2\ mv^2}{q} = 1/2\ R_E\varepsilon$$

where $\frac{mv^2}{R_E}$ = the force required for a particle of mass (m) and velocity (v) to move in the circular path of radius R_E.

$q\varepsilon$ = force on a particle of charge (q).

$$\varepsilon = \frac{V}{R_E \ln\left(\frac{R_1}{R_2}\right)}$$

where V = voltage drop between the two cylinders.
R_E = the radius of the path for the ions to pass through the analyzer.
R_1 = radius of the outer cylinder.
R_2 = radius of the inner cylinder.

A "spectrometer lens" is then used to focus the secondary beam into the 90°, 127 mm radius magnetic sector. Mass

analysis of the secondary ions is achieved according to the following equation:

$$\frac{mv}{q} = R_m B$$

where $q(vB)$ = the force on an ion of charge (q).
where B = the applied magnetic field.

$\frac{mv^2}{R_m}$ = the force required for a particle of mass (m) and velocity (v) to move in the circular path of radius R_m.
where R_m = the radius of the path for the ions to pass through the magnetic analyzer.

In the IMS 3f, ε is fixed (4500 eV) while the magnetic field (B) is scanned, leading to the measurement of m/q (mass/charge) for the secondary ions.

When operating the IMS 3f as an ion microprobe, the secondary beam is then deflected by a second electrostatic analyzer (ESA 2) (tunned for maximum secondary ion signal) for detection by either an electron multiplier or a Faraday cup. If the ion microscope mode of operation is desired, the electrostatic analyzer (ESA 2) is turned off and the secondary beam is focussed onto a channnel plate/phosphorus screen arrangement where a secondary ion image of the sputtered sample surface is formed.

1.6 Kinetic Energy Filtering and the Method of Specimen Isolation

1.6.1 Kinetic Energy Filtering

Two methods of molecular ion suppression, high mass resolution and kinetic energy filtering were introduced in section 1.3.2. For the work in this study, a variation of kinetic energy filtering, the so called "Specimen Isolation Method" was chosen.

Kinetic energy filtering exploits the differences in the kinetic energy distributions of atomic and molecular secondary ions. Molecular ions are almost exclusively confined to the low energy region (see Figure 1.6-1). Although the majority of the elemental secondary ions are also at lower energies, a tail extending to relatively higher energies is found (see Figure 1.6-1). Using these differences in energy distributions, it is possible to suppress the molecular ion interferences, and hence discriminate in favour of the atomic species through the analysis of high energy secondary ions. Complete descriptions of kinetic energy filtering methods are found in references 32, 35, 41 and 59.

In the IMS 3f, energy selection is acheived through the use of the energy slit and a "voltage offset" to the secondary ion extraction voltage (see Figure 1.6-2). With the electrostatic analyzer set to accept ions of energy equal to 4500 eV, the accelerating voltage at the sample holder is reduced by some voltage α (generally 50 to 100 V)

Figure 1.6-1

Typical secondary ion energy distributions of atomic (solid line) and molecular (dashed line) ions. The shaded areas represent the energy regions used for both conventional kinetic energy filtering (left) and the method of specimen isolation (right).

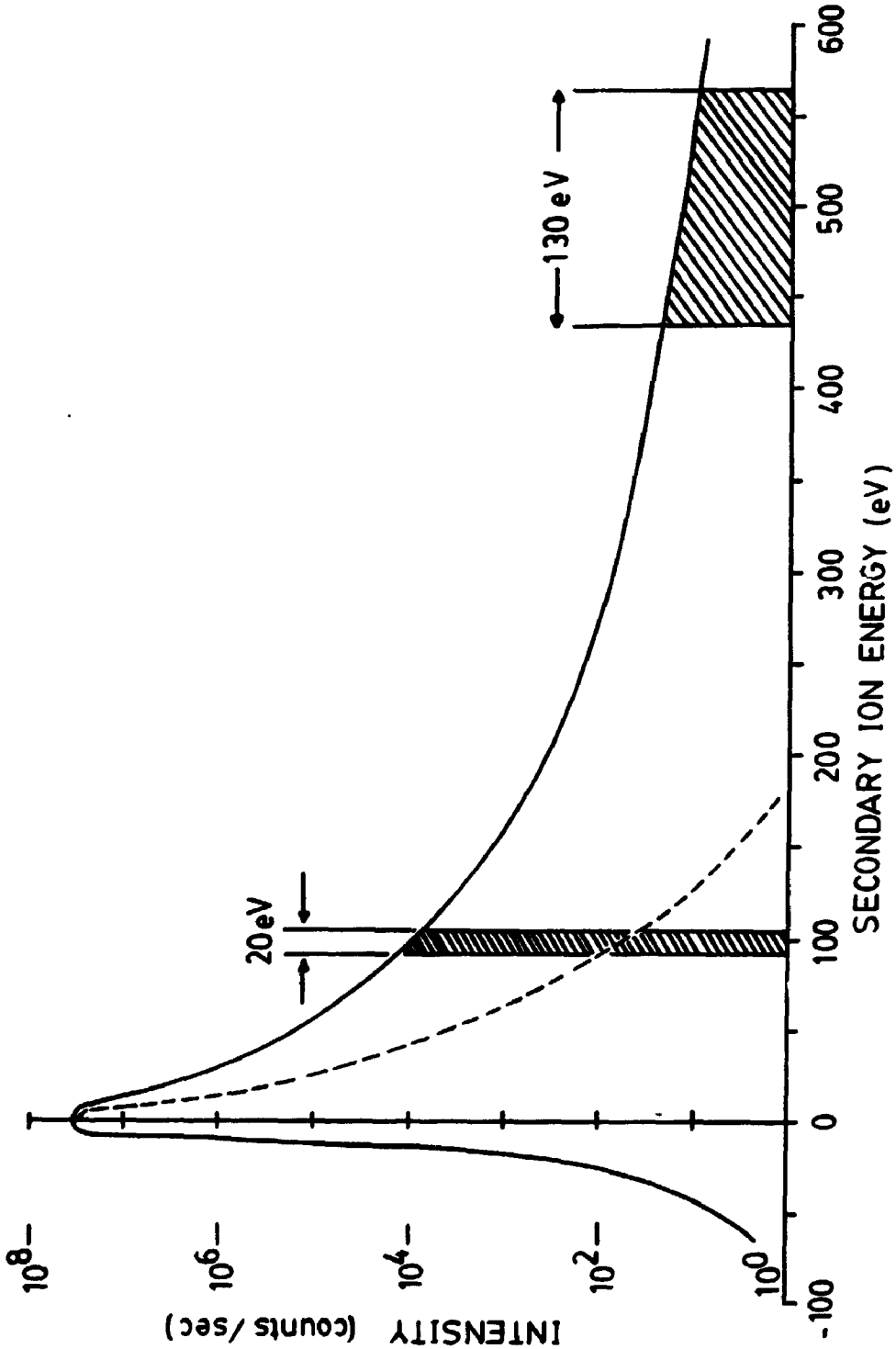
INTENSITY (counts/sec)
10^8
10^6
10^4
10^2
10^0
-100
0
100
200
300
400
500
600
SECONDARY ION ENERGY (eV)
20eV
130 eV

Figure 1.6-2

Conditions for energy filtering. A voltage offset is applied to the secondary accelerating voltage and the energy slit accepts a certain energy bandpass (dependent upon setting). Taken from reference 59.

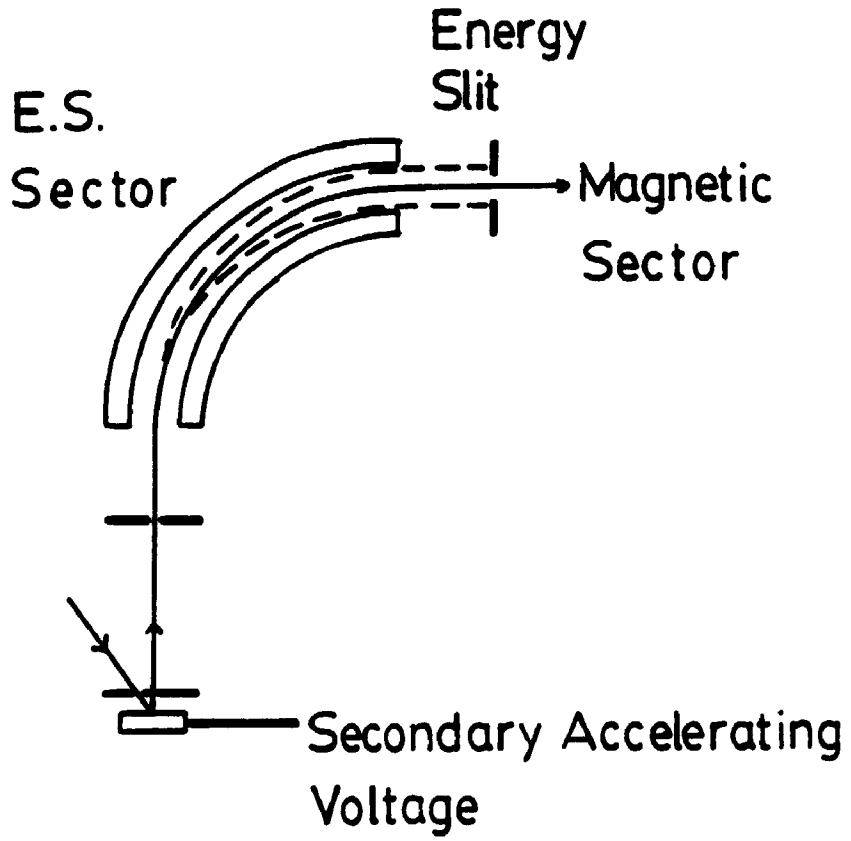
Energy
Slit
E.S.
Sector
Magnetic
Sector
Secondary Accelerating
Voltage

such that the low energy (~0 eV) ions will be accelerated with energy equal to 4500 - α eV and therefore will not pass through the electrostatic analyzer and on into the magnetic sector. However, higher energy ions (those of α eV) that are also accelerated with 4500 - α eV of energy will pass through the electrostatic sector (4500 eV) since they posses 4500 eV of energy.

In order to assess the necessary voltage offset required, the ratio of two isotopes is examined with respect to the voltage offset applied[35,59] (see Figure 1.6-3). By applying a voltage offset, the molecular ion interferences are reduced. This results in an isotope ratio similar to the natural abundance of the isotopes. In general, offset voltages required for sufficient suppression of molecular ion interferences are typically on the order of 50 to 100 V. However, most hydrides[38] and the oxides of the rare-earth elements[41] (REE) are not completely removed from the mass spectra when voltage offsets of 50 to 100 V are used. For this reason, either more extreme energy filtering (see Figure 1.6-1) is required, or the use of high mass resolution and/or some method of peak stripping to remove molecular ion interferences is necessary.

1.6.2 The Method of Specimen Isolation

The technique of specimen isolation is essentially an extreme form of kinetic energy filtering where secondary ions of energies in the range of 500 eV are used for

Figure 1.6-3

Suppression of molecular ions by kinetic energy filtering. The isotope ratio (A/B) (ordinate) is plotted against the applied voltage offset. The effect of increasing the voltage offset is seen as a reduction in the intensity of the interference (int.) at A until the true value for the isotope ratio (A/B) is obtained. Taken from reference 59.

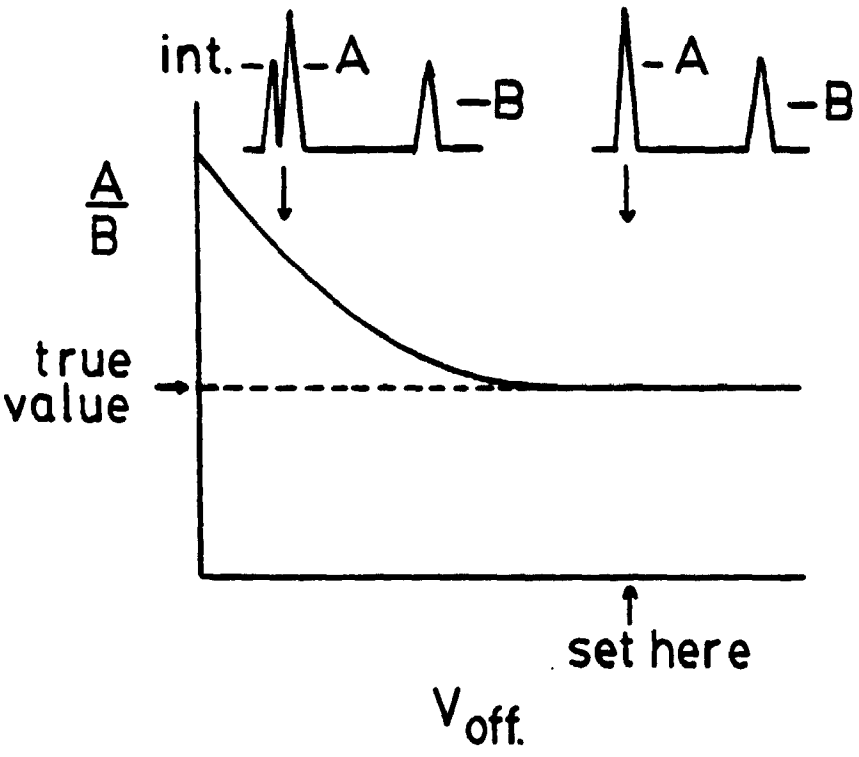
int.
A
B
A
B
A
B
true value
set here
$V_{off.}$

Figure 1.6-4

(a) Secondary ion mass spectrum (m/e from 1 to 100) of a crystalline titanite from Bear Lake Road obtained without any degree of energy filtering. The energy slit has been closed to reduce the secondary ion signal (primary beam: 15 to 16 kV and ~5 nA).

(b) Secondary ion mass spectrum (m/e from 1 to 100) of a crystalline titanite from Bear Lake Road obtained using specimen isolated conditions (primary beam: 15 to 16 kV and ~100 nA).

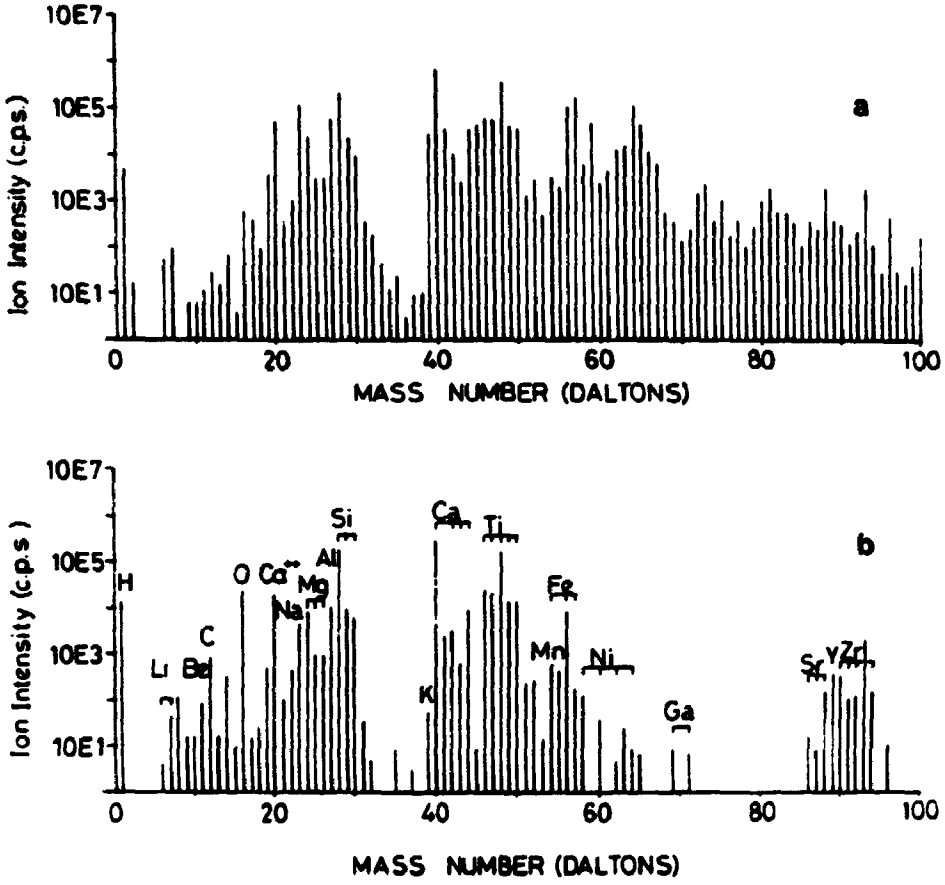
10E7
10E5
10E3
10E1
Ion Intensity (c.p.s.)
a
0
20
40
60
80
100
MASS NUMBER (DALTONS)
10E7
10E5
10E3
10E1
Ion Intensity (c.p.s.)
b
H
Li
Be
C
O
Ca
Na
Mg
Al
Si
K
Ca
Ti
Fe
Mn
Ni
Ga
Sr
Y
Zr
0
20
40
60
80
100
MASS NUMBER (DALTONS)

analysis (see Figure 1.6-1). This results in the almost complete removal of all molecular ion interferences from the mass spectra (see Figure 1.6-4). The specimen isolated method was developed at the Surface Science Western Laboratory by J.B. Metson and co-workers.[39,60-65]

Sample preparation in order to achieve specimen isolated conditions is minimal. In most cases (including mineral specimens) a flat (polished) specimen surface is all that is necessary. No conductive metal coating on the specimen surface is needed. In the sample holder, the specimen surface is covered by a charged (4500 eV) metallic plate (actually a thin tantalum sheet) with various areas (3 mm in diameter) of the specimen exposed for analysis (see Figure 1.6-5). In the case of conducting specimens, Teflon® spacers are used to electrically insulate the sample from the specimen holder (see Figure 1.6-5). With either type of specimen, conductor or insulator, the specimen is electrically isolated (insulated) from the sample holder and hence the name "Specimen Isolation." The sample holder/aperture arrangement is kept at 4.5 kV relative to the immersion lens (kept at ground) such that an extraction voltage of 4.5 kV is applied to the secondary ions.

The specimen isolation technique requires the use of O^- primary ions and the detection of positive secondary ions (i.e. a +4.5 kV extraction voltage). During bombardment of the target by the primary beam, the O^- ions (at a net energy of 15 to 16 kV) continue to deposit negative charge at the

Figure 1.6-5

The specimen holder arrangement for specimen isolated conditions with the CAMECA IMS 3f. Taken from reference 63.

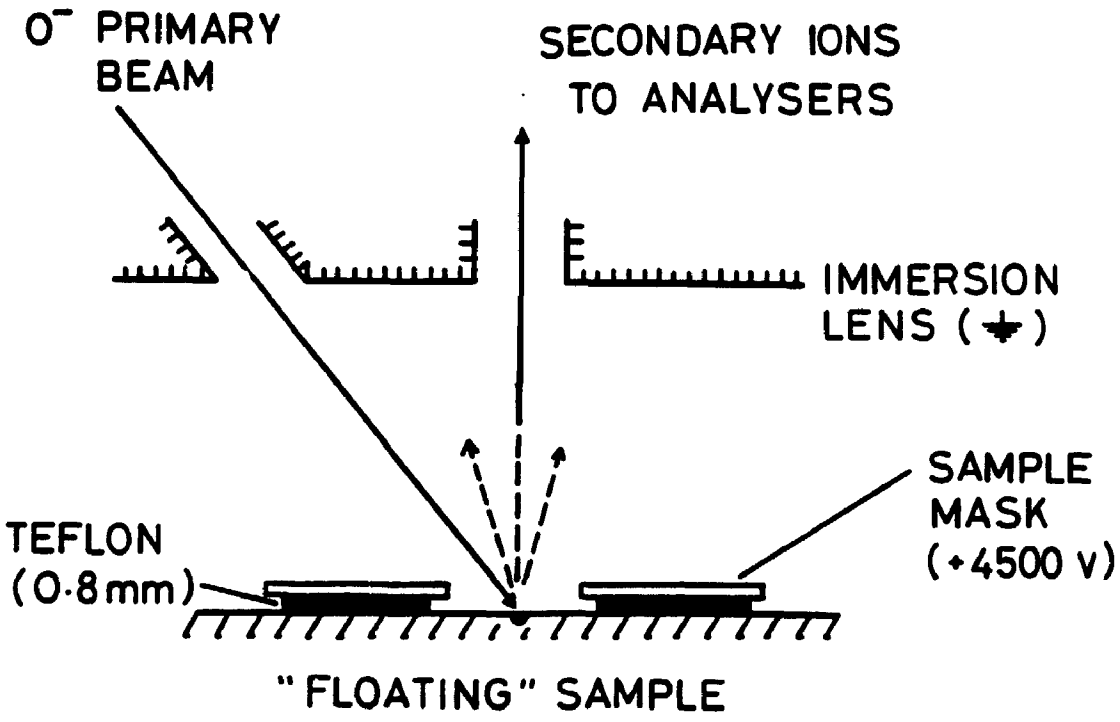
O⁻ PRIMARY BEAM
SECONDARY IONS TO ANALYSERS
IMMERSION LENS (+)
SAMPLE MASK (+4500 V)
TEFLON (0·8mm)
"FLOATING" SAMPLE

sample surface until this charge is stabilized by the flow of secondary electrons to the more positively charged (4500 eV) cover plate.[65] Thus, the area of analysis on the insulating specimen, previously at a potential of 4.5 kV is now charged in the negative direction due to bombardment by the O^- primary beam. Typically, charges in the range of -500 eV are produced by the primary beam. The net result is an extraction voltage of -4000 V, while the electrostatic analyzer is still set to accept ions having 4500 eV of energy. Thus, a voltage offset of -500 eV is produced. It is this large voltage offset that is responsible for the extreme form of energy filtering as displayed by mass spectra that are essentially free of molecular ion interferences (see Figure 1.6-4).

As well as an efficient form of molecular ion discrimination, the method of specimen isolation is well suited to the analysis of non-conducting materials. This is especially useful when surface analysis is of interest, since no surface coatings are required.

Figure 1.6-1 indicates a considerable reduction of intensity with increasing secondary ion energy. To compensate for the low intensity of high energy ions such that detection limits down to sub-ppm levels are possible, all of the slits and apertures in the secondary column (i.e. the spectrometer) are fully opened. This leads to minimum mass resolution ($M/\Delta M$ ~250) and maximum transmission of the secondary ions. Also, high primary ion currents are used to

obtain as much secondary ion intensity as possible. The high current density and some defocussing of the beam due to the charge on the insulating surface lead to large primary beam diameters (≥70 μm). These large primary beam diameters impose severe limitations on the sizes of specimens for analysis.

The method of specimen isolation has been successfully applied to the analysis of trace elements in various mineral phases.[66-69] Chapters 2 and 3 discuss the advantages and disadvantages of high energy secondary ions (i.e. the specimen isolation method) for use in quantitative SIMS analyses. Chapter 4 presents analyses for rare-earth elements in various mineral grains using the method of specimen isolation, whereas part II of this thesis deals with the application of the depth profiling capability of SIMS instruments to the study of altered plagioclase surfaces.

CHAPTER 2

INVESTIGATION OF MATRIX EFFECTS ON HIGH ENERGY SECONDARY IONS

2.1 Comparison of Glass Standards with Crystalline Minerals

2.1.1 Introduction

Micron scale resolution, ppm sensitivity and a complete mass range analysis are the features of SIMS that make it a powerful tool for the in situ analysis of geologic materials.[31,35] However, quantitative analysis of mineral (and other) specimens has been hampered by serious problems. First, molecular ions often obscure elemental ions. Second, the production of secondary ions is heavily influenced by the nature of the host matrix.[2,3] These problems make the correlation between secondary ion intensities and chemical compostions very difficult. And finally, since the majority of minerals are non-conducting, further problems arise due to the uncontrolled charging of the sample surface.

In certain cases, high mass resolution has been successfully used (for example, see reference 40). The use of kinetic energy filtering has been more widespread (for example, see references 32, 35, 41, 60, and 67), especially for removing molecular ion interferences at high mass

numbers where large mass resolving powers (M/ΔM) are commonly needed. Since molecular ions have a much narrower energy distribution than elemental ions,[32,35] analysis of high energy ions considerably reduces the relative intensity of molecular ions. Two distinct forms of energy filtering have been used, the "conventional" form of energy filtering (CEF) and the method of "specimen isolation." In conventional energy filtering methods, the sample surface is coated with a thin metal film or grid in contact with the sample holder. The accelerating potential of the secondary ions is then offset, usually by ~100 ± 10 V.[32,35,41] With the specimen isolation technique, an insulating sample is electrically isolated from the specimen holder and the sample charges negatively under bombardment from the O^- primary ion beam. Geologic specimens have shown stable, reproducible, charges of between 450 and 600 V below the secondary accelerating voltage (SAV) (when covered by a 3 mm diameter aperture).[65] It is this large voltage offset that produces an extreme form of kinetic energy filtering.

In a previous publication, McIntyre et al.[64] used an external power supply connected to the secondary ion extraction system of the CAMECA IMS 3f in order to analyze secondary ions of energy equal to 4500 eV. With a similar set of conditions to those of the specimen isolation method (maximum primary beam currents and a wide open secondary column) the results presented by McIntyre et al.[64] indicate

that when using a sample offset voltage of 450 V, secondary ion intensities similar to those obtained in the specimen isolation mode are observed. Therefore, with similar primary currents and hence similar beam dimensions, there is no clear advantage to the use of an external power supply to generate an offset voltage in the range of 500 V. As for the method of specimen isolation, the technique is very well suited to the analysis of non-conducting specimens without the need for conductive surface coatings. It could be argued however, that surface charging may be more accurately controlled when using conductive coatings and hence the external power supply.

Although several brief comments have appeared in the literature comparing the two energy filtering techniques (see references 41, 62, and 67), a quantitative study between the two for geologic specimens was necessary.[70] That is, while it seems to be generally recognized that the specimen isolation technique leads to greater molecular ion suppression but one is restricted by the large primary beam dimensions, there had been no study on geologic specimens comparing relative intensities, molecular ion and multiply charged ion intensities, relative structural matrix effects,[71] or stability and reproducibility. Reasoning that the surface charging is poorly controlled and that a large beam diameter is needed in the specimen isolation technique, Crozaz and Zinner[41,72] chose to use the CEF method coupled with the need for corrections of the light rare-earth

element (REE) oxides to analyze the heavy REE in order to determine REE concentrations in meteoritic phosphate grains. In contrast, MacRae and Metson[66] were successful in measuring REE concentrations at the sub-ppm level without the need for molecular ion corrections when using the specimen isolation method.

This section (as well as a previous publication[70]) presents a detailed comparison of the specimen isolation and conventional energy filtering techniques using natural and synthetic titanite samples. In light of the larger primary beam dimensions for the specimen isolation technique, the important advantages of the specimen isolation method for general geologic analyses will be discussed.

2.1.2 Experimental

A massive crystalline natural titanite sample from Bear Lake Road near Bancroft, Ontario and a titanite ceramic WP10 were used in this study. The titanite ceramic was supplied by Dr. P.J. Hayward of the Atomic Energy of Canada Limited (A.E.C.L.). The analyses of these two materials are given in Table 2.1-1. In order to investigate variations in relative ion intensities caused by differences in the structure of the target matrix, a portion of the natural titanite was melted in a platinum crucible at 1400 °C and then quenched in air to form a glass. A sample of this glass was crushed and then sintered at 1100 °C in a platinum

Table 2.1-1

Composition of titanite samples.*

Specimen	Bear Lake	AECL-WP10
SiO_2	33.64	33.33
CaO	33.02	31.58
TiO_2	30.14	32.08
Al_2O_3	0.64	0.50
FeO	1.79	-
Na_2O	0.32	0.25
MgO	0.32	-
K_2O	0.01	-
MnO	0.06	-
Nb_2O_5	0.07	-
SrO	NA†	0.50
Y_2O_3	NA	0.25
ZrO_2	NA	0.25
MoO_2	NA	0.25
SnO_2	NA	0.25
Cs_2O	NA	0.125
La_2O_3	NA	0.125
ThO_2	NA	0.25
UO_2	NA	0.25
Total	100.01	99.99

* Mole % oxides.

** Analysis by electron probe and conversion from weight % oxides to mole % oxides. Qualitative analysis by SIMS shows the presence of Y, Zr, La, Ce, U, Th, Pb and F in significants amounts (≥0.1 %).

† Not analyzed by electron probe.

crucible to produce a polycrystalline ceramic. Therefore, three samples of very similar chemistry but varying matrix structure were available.

A CAMECA IMS 3f secondary ion microscope[1,23,58] was used in this study. Modifications to the sample holder (to obtain specimen isolation conditions) and improvements to the electron multiplier pre-amplification system were made according to references 61 and 62. The total dead time of the counting circuit was ~70 ns. The maximum count rates observed were on the order of 10^6 counts per second, and therefore corrections for the dead time of the counting circuit were not necessary. A mass-filtered primary beam of $^{16}O^-$ ions at a net 15 to 16 kV and 5 to 300 nA was used. The primary beam diameters were on the order of ~25 and ~100 μm for measurements with the CEF and specimen isolation methods respectively. For energy filtering a voltage offset of -100 V was used and the energy window was narrowed to approximately ±10 eV while the remaining slits and apertures in the secondary column remained fully opened. Primary beam currents of 5 to 50 nA were used for analyses in the CEF mode. For measurements in the specimen isolated mode, the primary current was maximized (up to 300 nA) and the energy slit (±65 eV energy acceptance) along with the rest of the slits and apertures of the secondary column were fully opened. This resulted in a large primary beam diameter (≥70 μm) and maximum transmission of the secondary ions.[61] With the high primary beam current and the open energy window,

the ion intensities obtained in the specimen isolated mode become comparable to those from conventional energy filtering methods.[60-62,67] Thus, ppm sensitivity is easily obtainable using either method of energy selection. It is conceded that the large primary beam imposes serious limitations for in situ analyses of fine-grained geologic samples.

In order to obtain steady-state charging at the sample surface using specimen isolated conditions, it is necessary to use an uncoated insulating sample or a Teflon®-insulated conducting sample. A major factor in determining the degree of sample charging under specimen isolated conditions is the size of the charged aperture covering the surface.[65] When using a 3 mm (diameter) aperture, geologic samples often reach a potential some 450 to 600 V below the secondary accelerating voltage.[65,67] It is this large offset that is used for the extreme energy selection observed. More detailed descriptions of these methods of energy selection are contained in chapter 1 and the references sited therein.

2.1.3 Results and Discussion

Molecular Ion and Multiply Charged Ion Intensities

It has been previously demonstrated with conducting specimens that the ion intensities from specimen isolation conditions are comparable to those from conventional forms of energy filtering.[62] It is also well known that the

amount of molecular ion suppression (as given by M^+/MO^+ ratios) is increased by employing greater amounts of kinetic energy filtering.[32,60] These points are shown for SIMS spectra of mineral samples in Figure 2.1-1 (a and b) and Figure 2.1-2. Figure 2.1-1 (a and b) are secondary ion mass spectra of the mass range from 1 through 70 for the Bear Lake titanite sample obtained with specimen isolation and conventional energy filtering methods respectively. Figure 2.1-2 shows SIMS bar graph spectra (mass spectra) of the heavy elements contained in the synthetic titanite specimen. In Figure 2.1-1(a) (specimen isolation), the intensities of the $^{40}Ca^+$ and $^{48}Ti^+$ peaks are 1.6×10^5 and 1.8×10^4 counts respectively. The same peaks in Figure 2.1-1(b) (conventional energy filtering) have 1.7×10^4 and 9.6×10^3 counts respectively. The primary beam currents chosen (80 and 5 nA respectively) and the width of the energy slit will determine some of the intensity loss. However, what is most striking is the increased molecular ion suppression gained when using specimen isolation. This is seen in Table 2.1-2 and by the oxide peaks of titanium in Figure 2.1-1. In spectrum (a) of Figure 2.1-1 there is only one oxide peak of titanium present ($^{48}TiO^+$), and $^{48}Ti^+/^{48}Ti^{16}O^+ = 1.94\times10^4$. This is in marked contrast to spectrum (b) where oxide peaks appear for all of the titanium isotopes, and $^{48}Ti^+/^{48}Ti^{16}O^+ = 4.77\times10^2$, almost two orders of magnitude difference. Table 2.1-3 lists the measured abundances for the titanium isotopes and the oxides of titanium in the

Figure 2.1-1

(a) Secondary ion mass spectrum of a crystalline titanite from Bear Lake Road obtained using specimen isolated conditions (primary beam: 15 to 16 kV and 80 nA).
(b) Secondary ion mass spectrum of a crystalline titanite from Bear Lake Road obtained using a -100 V sample offset voltage and a ±10 eV energy slit (primary beam: 15 to 16 kV and 5 nA). Taken from reference 70.

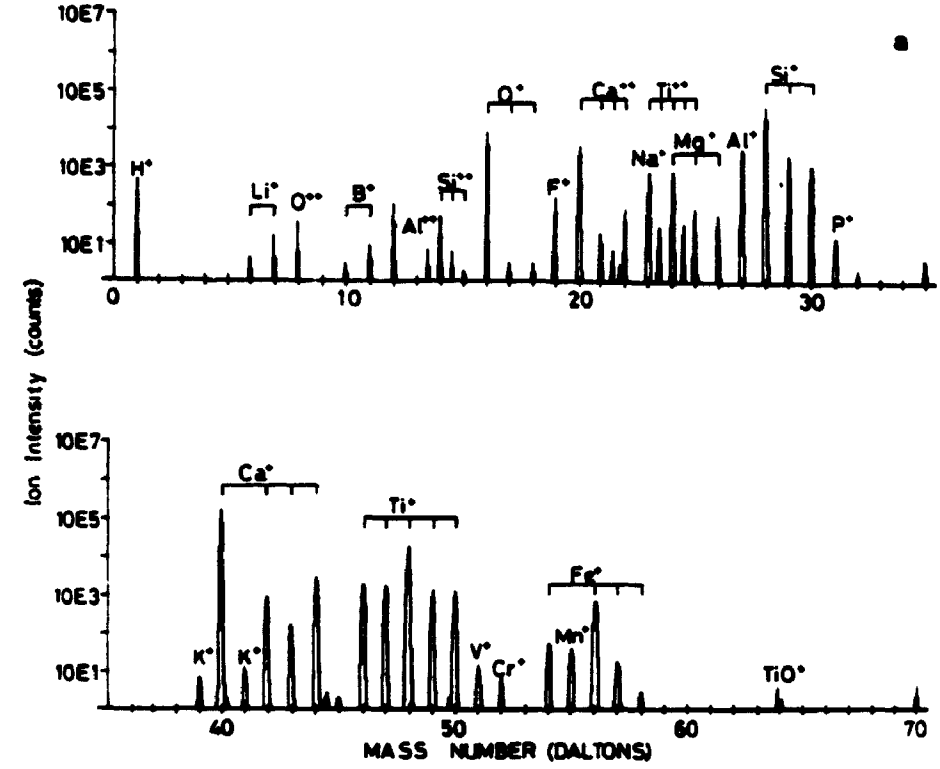
a
10E7
10E5
10E3
10E1
H°
Li°
O°°
B°
Al°°
Si°°
O°
Ca°°
Ti°°
F°
Na°
Mg°
Al°
Si°
P°
0
10
20
30
Ca°
Ti°
Fe°
K°
K°
V°
Cr°
Mn°
TiO°
40
50
60
70
Ion Intensity (counts)
MASS NUMBER (DALTONS)

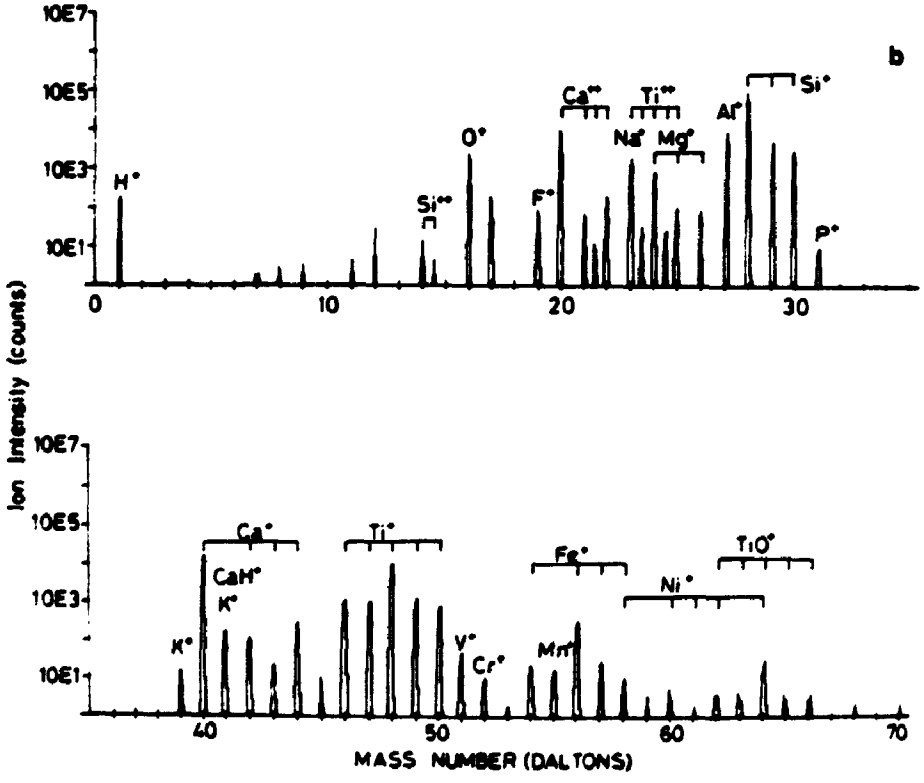
b
10E7
10E5
10E3
10E1
H°
Si°°
O°
Ca°°
Ti°°
F°
Na°
Mg°
Al°
Si°
P°
0
10
20
30
Ca°
CaH°
K°
K°
Ti°
V°
Cr°
Mn°
Fe°
Ni°
TiO°
40
50
60
70
Ion Intensity (counts)
MASS NUMBER (DALTONS)

Table 2.1-2

Molecular ion suppression ratios (M^+/MO^+) obtained using specimen isolation and CEF conditions on the Bear Lake titanite showing the decrease in the suppression ratio with increasing mass and the greater molecular ion suppression obtained by using specimen isolation conditions.

Isotope	CEF		Specimen Isolation	
	M^+ (counts s^{-1})	M^+/MO^+	M^+ (counts s^{-1})	M^+/MO^+
$^{29}Si^+$	3.24×10^4	1.80×10^2	1.01×10^4	1.12×10^3
$^{48}Ti^+$	9.34×10^5	4.77×10^2	1.74×10^5	1.94×10^4
$^{93}Nb^+$	1.37×10^4	6.64×10^1	2.21×10^3	$\geq2\times10^3$
$^{139}La^+$	1.33×10^4	1.35×10^1	4.67×10^3	1.90×10^2

Table 2.1-3

Percent abundances of Ti^+ and TiO^+ ions in the SIMS mass spectra of Figure 2.2-1 (a and b) (Bear Lake titanite) obtained under specimen isolation and CEF conditions (±0.1 %).

Isotope	Natural abundance of isotope[a]	Specimen Isolation	CEF	CEF (TiO^+ ions)
$^{46}Ti^+$	7.9	7.5	7.7	8.1
$^{47}Ti^+$	7.3	7.5	7.5	9.1
$^{48}Ti^+$	73.9	74.2	70.5	71.0
$^{49}Ti^+$	5.5	5.6	8.9[b]	5.9
$^{50}Ti^+$	5.3	5.2	5.4	5.9

[a] The National Bureau of Standards, November, 1967.

[b] Note the presence of $^{48}Ti^1H^+$ when using CEF conditions.

Figure 2.1-2

Mass spectra of WP-10 titanite ceramic obtained using specimen isolated and CEF conditions showing the presence of LaO^+ and ThO^+. Using specimen isolated conditions, $La^+/LaO^+ = 1.90\times10^2$ and $Th^+/ThO^+ = 6.8\times10^1$. Using a 100 V energy offset, $La^+/LaO^+ = 1.35\times10^1$ and $Th^+/ThO^+ = 8.6$ (primary beam: 15 to 16 kV and 200 nA). Taken from reference 70.

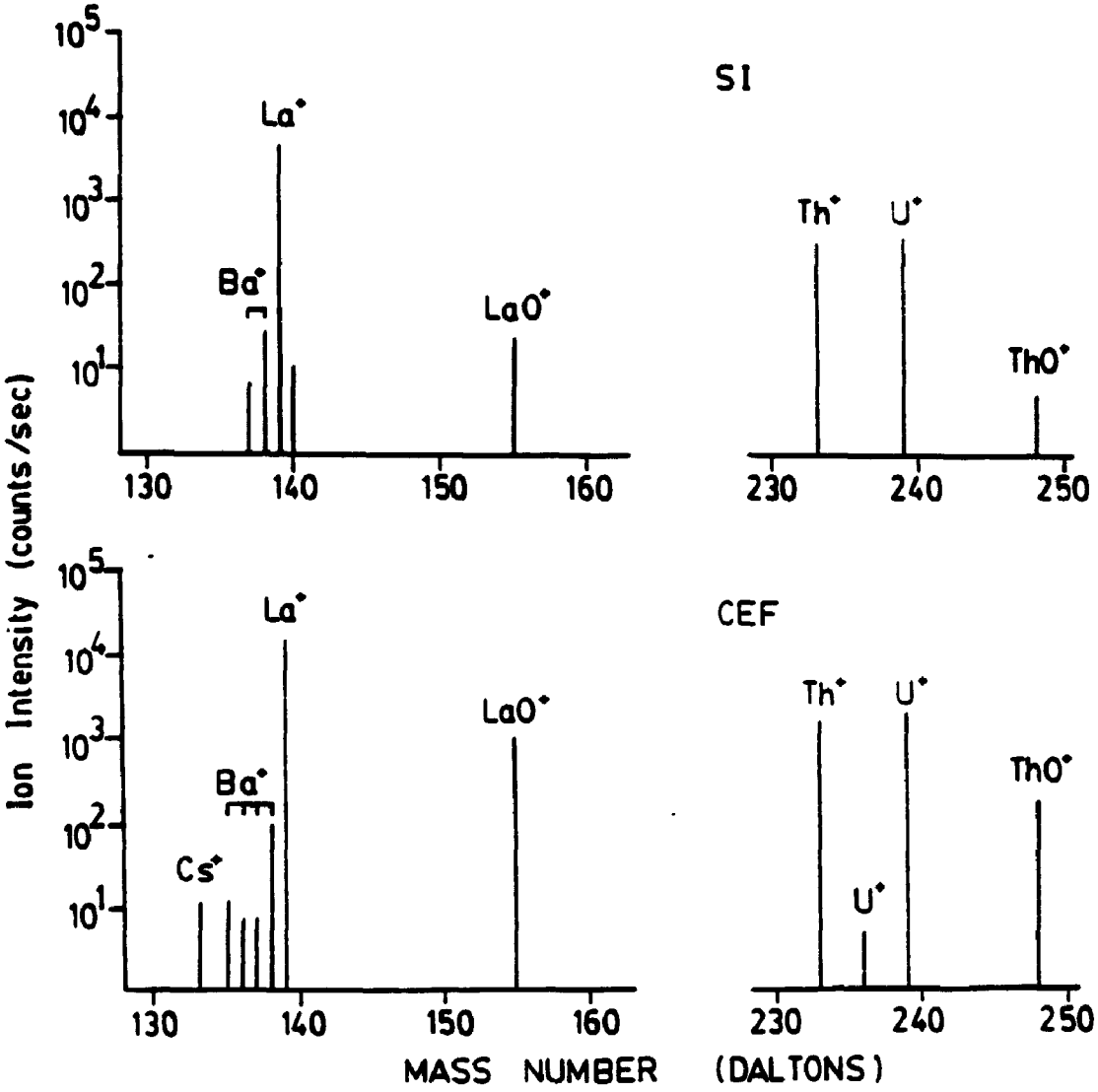
SI
CEF
Ion Intensity (counts/sec)
MASS NUMBER (DALTONS)
La+
Ba+
LaO+
Th+
U+
ThO+
Cs+
10^5
10^4
10^3
10^2
10^1
130
140
150
160
230
240
250

natural titanite using both forms of energy filtering. With specimen isolation, the abundances of the titanium isotopes resemble the natural abundances of the isotopes, while $^{49}Ti^+$ is significantly overestimated when using the CEF mode. An appreciable contribution from $^{48}Ti^1H^+$ to the $^{49}Ti^+$ peak in spectrum (b) of Figure 2.1-1 is responsible for the greater than expected intensity at mass 49. The results from Figures 2.1-1 and 2.1-2 and Tables 2.1-2 and 2.1-3 show that oxides as well as hydrides are suppressed much more effectively when using the specimen isolation technique.

The increased molecular ion suppression is of particular value when elements of high mass number such as the rare-earth elements are of interest. As the mass of the element (M) increases, the energy distribution of the element oxide (MO^+) broadens,[41,73] therefore making the suppression of these oxide ions increasingly more difficult. The decrease in suppression of the element oxide peaks with increasing atomic number of the element is shown in Table 2.1-2 and Figure 2.1-2. In the conventional form of energy filtering, the $^{139}La^+/^{139}La^{16}O^+$ and $^{232}Th^+/^{232}Th^{16}O^+$ ratios decrease sharply to 13.5 and 8.6 respectively, whereas in the specimen isolation mode, the $^{139}La^+/^{139}La^{16}O^+$ and $^{232}Th^+/^{232}Th^{16}O^+$ ratios are 190 and 68 respectively. As reported by Reed,[73] lanthanum and cerium have the greatest oxide intensities of the rare-earths. Thus, when using the method of specimen isolation, the $REE^+/REEO^+$ ratios for all of the rare-earths are ≥200 (and usually ≥500) and no

correction of light rare-earth oxides in the heavy REE region is necessary for complete rare-earth analysis. Therefore, provided that the samples are greater than 70 μm in diameter,[61,66] the specimen isolation technique is an ideal method for the analyses of REE in mineral specimens. In contrast, corrections for the heavy rare-earth region of the mass spectrum is necessary with the CEF mode since not all molecular ion interferences are eliminated from the mass spectra. With the oxides of the light rare-earths still present in appreciable intensity, deconvolution of the peaks corresponding to the heavy REE using assumed light rare-earth M^+/MO^+ ratios must be made in order to obtain a complete rare-earth analysis in mineral grains.[41,72,74]

It is also important to examine the relative intensities of the multiply charged species with the two forms of kinetic energy filtering. In an earlier report by Nesbitt et al.[67] it was noted that the "yield of multiply charged ions is apparently enhanced with the specimen isolation technique", but there had been no comment in the literature on the yield of multiply charged species when using conventional energy filtering methods. In this study it was somewhat suprising to find large M^{2+} peaks in the spectra obtained with conventional energy filtering methods (see Figure 2.1-1(b)). Table 2.1-4 summarizes the $M^{2+}/^{28}Si^+$ ratios found when using both forms of energy filtering. Depending on the element of interest, the amount of doubly charged species (M^{2+}) varies without trend between the two

Table 2.1-4

Multiply charged ion intensities relative to $^{28}Si^{+}$ ($M^{2+}/^{28}Si^{+}$) for the specimen isolation and CEF techniques.

Isotope	CEF	Specimen	$\frac{\text{Specimen Isolation}}{\text{CEF}}$
$^{40}Ca^{2+}$	8.55×10^{-2}	7.40×10^{-2}	0.847
$^{44}Ca^{2+}$	1.89×10^{-3}	1.52×10^{-3}	0.804
$^{47}Ti^{2+}$	2.76×10^{-4}	6.89×10^{-4}	2.50
$^{49}Ti^{2+}$	2.38×10^{-4}	5.94×10^{-4}	2.50

forms of energy filtering (see Table 2.1-4). As previously noted,[67] these multiply charged ions lead to rather few interferences. In addition, since many of the M^{2+} peaks occurring at half-integral masses are unique, they may, in some cases, be useful for elemental analyses.

As noted earlier,[67] there is generally a "clean" interference-free isotope available for most elements, including the rare-earths. However, in some cases, corrections are still necessary. For example, in the case of titanite, both $^{23}Na^{+}$ and $^{46}Ti^{2+}$ contribute to the intensity of the peak at mass 23. To determine the intensity due to $^{23}Na^{+}$, the contribution of $^{46}Ti^{2+}$ can be estimated from the $^{46}Ti^{+}/^{47}Ti^{+}$ ratio, and the $^{47}Ti^{2+}$ intensity at mass 23.5.

Charging and Reproducibility

For quantitative analyses with the method of specimen isolation, constant reproducible charging is of the greatest importance. The results using the specimen isolation technique presented here are intended to show that charging for different samples is very similar and that the reproducibility of the data is just as good as, if not better than, that obtained when using conventional energy filtering.

A proposed mechanism of charge stabilization in the specimen isolation method has been presented by Lau et al.[65] The degree of sample charging at the sample surface may

easily be measured by scanning the electrostatic analyzer (ESA 1) in the secondary column of the CAMECA IMS 3f.[65] An energy distribution of the secondary ions is obtained by adjusting the voltages to the electrostatic plates such that the measurements of ion intensities are recorded at various kinetic energies (see Figure 2.1-3). Making the assumption that the peak of the energy distribution is representative of zero energy (0 eV) ions, it is possible to assess the surface charging by working back through the energy curve.[65] Since the transmission of the spectrometer varies with the energy of the ions sampled, it was necessary to make adjustments to the secondary column in order to obtain the plots illustrated in Figure 2.1-3. These adjustments involve the immersion and transfer lenses along with the magnetic field and deflectors (ESA 2) to the electron multiplier-counting system. In almost all cases, it was necessary to close down the contrast aperture in order to accommodate the increased intensity of the lower energy ions. It is realized that changing the size of the contrast aperture will alter the angle of acceptance of the secondary ions and thus will result in some distortion of the apparent kinetic energy distribution of the secondary ions. However, this will only affect the total observed intensity and not the position of the intensity peak and thus the determined voltage offset.

Figure 2.1-3 shows the energy distribution curves that were recorded for the three various structures of the

Figure 2.1-3

Energy distribution diagrams for the $^{28}Si^{+}$ ion in the three titanite samples (▲, crystalline; ●, ceramic; and O, glass) obtained by scanning the electrostatic analyzer in the secondary column of the CAMECA IMS 3f (primary beam: 15 t0 16 kV and 130 nA). Taken from reference 70.

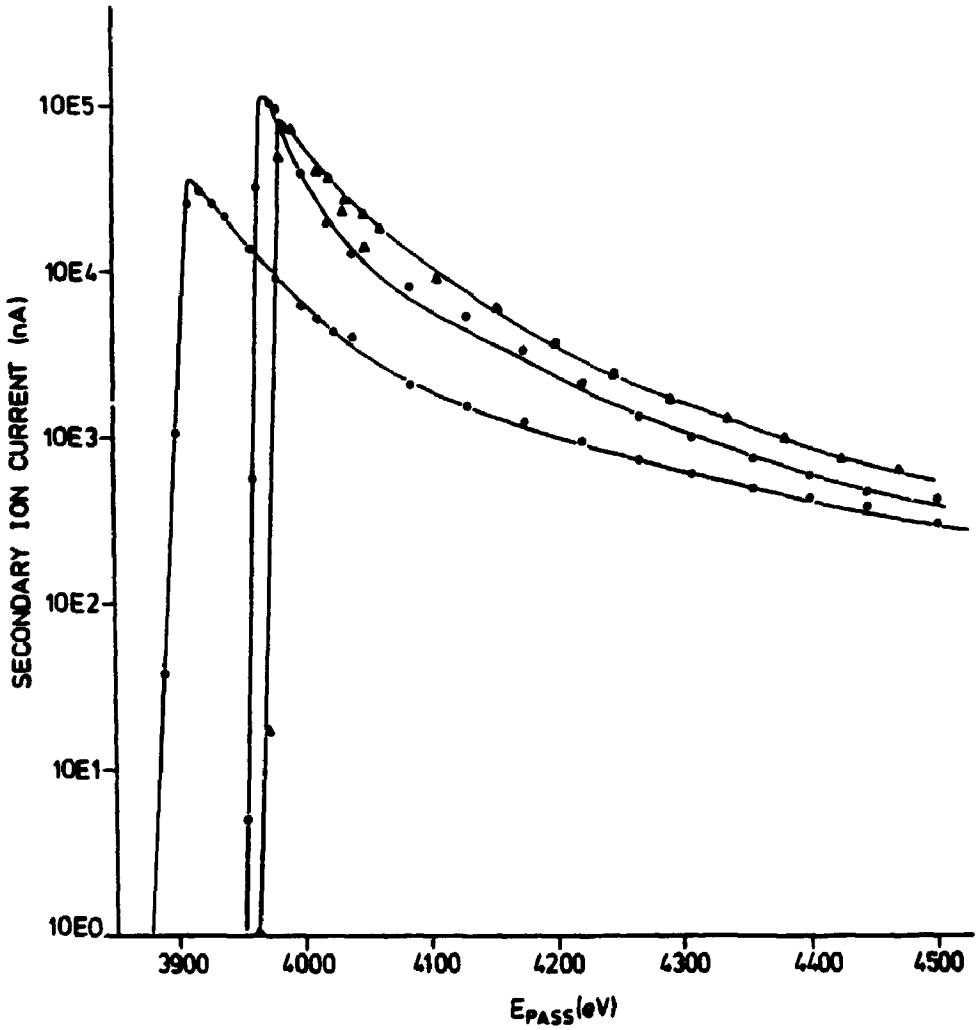
10E5
10E4
10E3
10E2
10E1
10E0
SECONDARY ION CURRENT (nA)
3900
4000
4100
4200
4300
4400
4500
EPASS(eV)

titanite sample. The primary beam current used in all three measurements was 130 nA. The results from Figure 2.1-3 show that the crystalline, glass and ceramic samples charge to similar potentials (513 ± 10, 580 ± 10, and 527 ± 10 V below the SAV, respectively). Furthermore, when using different beam currents of 30 and 300 nA on different days and presumably slightly different operating conditions, the voltage offsets obtained for the glass sample were 475 ± 10 and 493 ± 10 V, respectively. Minor differences in the primary beam energy from day to day may be responsible for these small differences in charging potentials between the two experiments. These results show that the charging potential under specimen isolated conditions for different structural types and different primary beam currents will fall within approximately ±10 %. Since the ion yield curves are flat and parallel[41,71,72] at high kinetic energies (see Figure 2.1-3), the small differences in charging potential should not be a problem for quantitative analyses. This point is also made by Crozaz and Zinner[41,72] who show that the ion yields of the REE are insensitive to changes in the sample offset voltage when sampling ions with kinetic energies of 80 eV or greater. The similar charging of glass and crystalline samples would suggest that glass standards of similar chemical composition could be used for quantitative mineral analysis.

The results in Table 2.1-5 confirm these predictions. Table 2.1-5 gives the ion intensities (relative to $^{28}Si^{+}$) of

fourteen major and trace elements for the three forms of titanite analyzed with both methods of energy filtering (specimen isolation and CEF). A number of points emerge from this table. First, the standard deviations for each individual sample are generally less than 10 % for both techniques, with the CEF method often giving somewhat smaller deviations on the heavier elements (the heavier elements are generally in trace amounts) due to higher count rates. Second, the intensities relative to $^{28}Si^{+}$ can be very different between the two methods. Thus, the $^{93}Nb^{+}/^{28}Si^{+}$ ratios obtained with specimen isolation and conventional energy filtering are ~9×10^{-3} and ~2×10^{-3}, respectively, reflecting the different relative shapes of the $^{93}Nb^{+}$ and $^{28}Si^{+}$ ion yield curves at different kinetic energies. Obviously, similar offset voltages are essential for both unkonwn and standard samples if quantitative results are desired. Third, and most importantly, the results for the three different structural types usually show very similar relative intensities. The standard deviations on the average of the three samples are comparable with the standard deviation on one of the samples. Quite often the standard deviation for the average using specimen isolated conditions is smaller than that when using conventional energy filtering. The similar relative intensities for both glass and crystals are of particular advantage for quantitative analysis of geologic materials since one may use glass standards (of similar major element

Table 2.1-5

(a) Ion intensities relative to $^{28}Si^{+}$ of the three titanite samples (crystalline, glass, and ceramic) obtained using specimen isolation conditions using an $^{16}O^{-}$ primary ion beam at a net 15 to 16 kV and 100 nA. Each mass unit was counted for 5 s and the masses were cycled through 8 times. The standard deviations are represented as a percentage of the ion intensities and are found in parentheses. The standard deviations generally ranged from 2 to 10 %, while reasons for deviations greater than 10 % are not well understood.

Isotope	Crystalline	Glass	Ceramic	Deviation (%)
^{23}Na	1.87×10^{-2} (4.7)	1.91×10^{-2} (4.2)	2.23×10^{-2} (5.1)	9.8
^{26}Mg	4.07×10^{-3}(18)	1.91×10^{-3} (3.9)	3.48×10^{-3} (9.4)	35
^{27}Al	1.01×10^{-1} (2.0)	1.05×10^{-1} (1.4)	0.93×10^{-1} (5.8)	6.1
^{39}K	1.03×10^{-4}(43)	2.80×10^{-4} (9.3)	1.05×10^{-3}(24)	105
^{40}Ca	1.89×10^{0} (1.6)	1.95×10^{0} (4.8)	2.16×10^{0} (2.1)	7.0
^{47}Ti	0.97×10^{-1} (2.1)	1.02×10^{-1} (6.0)	1.10×10^{-1} (5.6)	6.4
^{51}V	1.12×10^{-3} (5.2)	1.12×10^{-3} (5.8)	1.17×10^{-3} (6.2)	2.6
^{52}Cr	2.89×10^{-4}(17)	2.61×10^{-4}(12)	2.65×10^{-4} (6.6)	5.5
^{55}Mn	2.54×10^{-3} (6.3)	2.42×10^{-3} (7.0)	2.59×10^{-3} (4.2)	3.6
^{56}Fe	3.58×10^{-2} (2.9)	3.62×10^{-2} (7.4)	3.81×10^{-2} (5.0)	3.3
^{88}Sr	5.04×10^{-4} (4.6)	5.22×10^{-4}(15)	5.42×10^{-4} (7.9)	3.6
^{89}Y	1.76×10^{-3} (5.7)	1.96×10^{-3}(19)	1.91×10^{-3} (5.5)	5.3
^{90}Zr	1.87×10^{-3} (6.7)	2.03×10^{-3}(22)	1.99×10^{-3} (6.3)	4.1
^{93}Nb	8.99×10^{-3} (4.7)	9.28×10^{-3}(28)	9.38×10^{-3} (7.4)	2.2

Table 2.1-5 continued

(b) Ion intensities relative to $^{28}Si^{+}$ of the three titanite samples (crystalline, glass, and ceramic) obtained using the CEF mode and an $^{16}O^{-}$ primary ion beam at a net 15 to 16 kV and 50 nA. Each mass unit was counted for 5 s and the masses were cycled through 8 times. The standard deviations are represented as a percentage of the ion ion intensities and are found in parentheses. The standard deviations generally ranged from 2 to 10 %, while reasons for deviations greater than 10 % are not well understood.

Isotope	Crystalline	Glass	Ceramic	Deviation (%)
^{23}Na	2.78×10^{-2} (6.9)	2.75×10^{-2} (6.5)	4.28×10^{-2} (9.3)	27
^{26}Mg	1.62×10^{-3} (9.0)	2.24×10^{-3}(16)	4.05×10^{-3}(12)	48
^{27}Al	1.43×10^{-1} (1.7)	1.30×10^{-1} (3.2)	1.30×10^{-1} (6.8)	6.0
^{39}K	5.56×10^{-5}(12)	1.37×10^{-3}(26)	1.95×10^{-3} (7.1)	86
^{40}Ca	3.33×10^{0} (2.6)	3.37×10^{0} (5.4)	2.96×10^{0} (6.5)	7.1
^{47}Ti	1.60×10^{-1} (1.9)	1.64×10^{-1} (4.0)	1.43×10^{-1} (4.7)	7.7
^{51}V	1.93×10^{-3} (3.2)	1.90×10^{-3} (3.3)	2.18×10^{-3} (8.6)	7.5
^{52}Cr	4.08×10^{-4} (3.4)	3.68×10^{-4} (5.5)	3.96×10^{-4} (7.6)	5.4
^{55}Mn	3.36×10^{-3} (3.6)	3.33×10^{-3} (5.0)	3.87×10^{-3} (6.7)	8.5
^{56}Fe	5.29×10^{-2} (2.7)	5.29×10^{-2} (4.8)	6.15×10^{-2} (5.2)	9.0
^{88}Sr	1.44×10^{-3} (3.4)	1.40×10^{-3} (4.1)	1.49×10^{-3} (3.0)	3.1
^{89}Y	4.72×10^{-3} (3.4)	4.10×10^{-3} (2.6)	4.21×10^{-3} (9.8)	7.6
^{90}Zr	4.49×10^{-3} (3.9)	4.01×10^{-3} (2.9)	4.32×10^{-3} (7.5)	5.6
^{93}Nb	2.07×10^{-2} (3.4)	1.85×10^{-2} (4.9)	1.93×10^{-2} (5.6)	5.6

chemistry to the unknown sample in order to reduce any chemical matrix effects) to obtain calibration curves for the trace element analysis in minerals when using either form of kinetic energy filtering. The so-called structural matrix effect discussed by Ray and Hart[71] may therefore be neglected for most elements when using some form of energy filtering.

As a final comment on the results presented, the results for the alkalis and magnesium for both types of energy selection show large deviations between the three samples. These deviations are presumably due to a migration effect[38] caused by the "charging-up effect" being different for glass and crystalline samples. Havette[38] used $^{23}Na^{+}$ as an example of the migration effect and our relatively poor agreement for Na, K and Mg may well be caused by the slightly different charging potentials[38] and possibly even temperatures[30] at the surface of the three analyzed samples. For these elements and possibly others not studied here, further results and understanding are necessary before one can use glass standards for quantitative anlaysis of minerals.

2.1.4 Conclusions

The major advantage of the extreme form of energy filtering given by the specimen isoaltion technique is the increased molecular ion suppression. This gain in molecular ion suppression makes it possible to analyze, for example,

for all the rare-earth elements without the need for the corrections that are required when using conventional energy filtering techniques. This increase in molecular ion suppression is obtained without any significant loss of sensitivity, reproducibility, or increase in multiply charged ions. However, the limitation of using a large primary beam (≥70 μm diameter as in the specimen isolated method) versus a smaller beam (~10 μm diameter for the CEF mode) is obvious in that fine-grained minerals cannot be analyzed at the present time with the specimen isolated method.

Energy distribution curves show that samples of similar chemistry and varying matrix structure charge up to similar potentials when similar primary beam conditions are used in the method of specimen isolation. The primary beam current was not found to have any significant effect on the charging potential of the sample. Since samples of various structures commonly charge to similar potentials, it must follow that the secondary ions entering the spectrometer are from similar regions of the energy distribution curves. Hence, the resultant relative ion intensities show considerable correlation for the three samples studied. These principles will, in turn, allow one to use calibration curves established from glass standards for the purpose of determining quantitative analysis of crystalline minerals. To fully accomplish a complete quantitative mineral analysis with the ion microprobe, an understanding of the migration of light elements due to varying charging potentials

("charging-up effect")[38] or surface temperatures[30] must be gained. Further studies on the migration of such elements are thus required.

2.2 Relative Ion Intensities from the Olivine Series

2.2.1 Introduction

Another problem encountered in quantitative analyses with the SIMS technique relates to the chemical composition of the host matrix from which the secondary ions result.[1-3,35] This is due to the differing ionization potentials, binding energies and work functions of the various elements,[35] resulting in a complication of the interelement ratios of ionization probabilities, and therefore leading to different interelement intensit; (secondary ion) ratios.[35] Changes in the ionization probability of as much as a few orders of magnitude due to changes in the chemical composition of the target have been discussed.[1-3] In discussing secondary ion intensities from polycomponent materials, Shimizu and and Hart[35] also write about problems due to preferential sputtering.

Preferential sputtering is the more efficient removal of certain material from the surface. Preferential sputtering is thought to occur for either the lower mass component, and/or the component that forms the weaker bond with the neighbouring atoms (see reference 35 and the references within). Changes in the surface composition as sputtering proceeds is seen as a result of preferential

sputtering. The effects of preferential sputtering are generally observed early in the sputtering process, and then disappear with time. Initially, a certain component (A) is enriched in the sputtered population, while the other component(s) (B) are concentrated in the residue at the surface, and thus the composition of the surface is no longer representative of the bulk specimen. With time, the amount of A in the sputtered population decreases, while that of B increases. After further time, the system will reach a steady-state of sputtering. At steady-state, the sputtered population is said to have the same composition as the bulk of the specimen.[35] Since the chemical composition of the sputtered material is the same as that of the surface (and hence the interior), but the secondary ion intensity is not easily related to the sample composition, the differences may therefore be a result of the ionization part of the sputtering process.[35] The effects of preferential sputtering are generally ignored during quantitative (and isotope) analysis since these measurements are made after a steady-state of sputtering has been obtained. However, it is realized that when depth profiling the surfaces of materials, preferential sputtering makes the interpretation of the near surface regions of the profiles somewhat tricky.

Although preferential sputtering may be neglected, the problems of fluctuating secondary ion yields still exists. In chapter 1 the matrix effects for a binary alloy (A-B) were introduced. In the case where A forms a stronger

oxide bond than B does, the presence of A will increase the ionization of B, whereas the presence of B will decrease the ionization of A.[46-48] The following mechanism is given by Shimizu[48] for the effect of A (or B) on the secondary ion intensity of B (or A):

$$MO + Si^+ \longrightarrow SiO + M^+$$

The olivine solid solution series is a common mineral system used to show the change in secondary ion yield of one element as a function of the composition of the concentration of another.[35,75]

In 1981, Steele et al.[75] reported the variations in Mg^+, Fe^+ and Si^+ secondary ion intensities within the olivine series and low-Ca pyroxenes using an AEI SIMS instrument. Figure 2.2-1 (Figure 3 (a) from Steele et al.[75]) is a plot of the secondary ion intensities for Mg^+, Fe^+, and Si^+ against the values obtained from the electron probe for an olivine solid solution series. In order to eliminate molecular ion interferences, Steele et al.[75] used high mass resolution, and thus low energy (~0 eV) ions were analyzed. In Figure 2.2-1, the intensity of Si^+ passes through a minimum near Fo = 65, whereas the Fe^+ signal shows a near-linear decrease from fayalite (iron end member) through to forsterite (magnesium end member). The Mg^+ secondary ion signal is quite interesting. As the magnesium content of the sample increases, the Mg^+ signal increases to a maximum near Fo = 80, and then decreases with increasing magnesium content (see Figure 2.2-1). As for the

Figure 2.2-1

Variation of secondary ion count rates for Si^+, Mg^+, and Fe^+ in olivi..es as a function of forsterite content. Taken from reference 75 (Figure 3(a)).

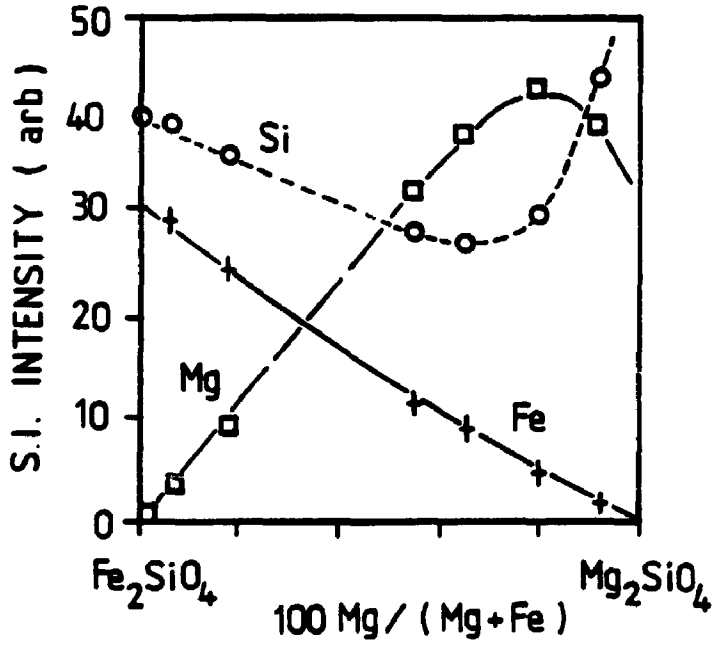
50
40
30
20
10
0
S.I. INTENSITY (arb)
Si
Mg
Fe
Fe_2SiO_4
Mg_2SiO_4
100 Mg / (Mg + Fe)

low-Ca pyroxenes studied by Steele et al.,[75] the iron displayed similar behavior to the olivines, whereas the magnesium signal did not show a maximum, but rather considerable scatter about a line.

Using a CAMECA IMS 3f instrument, Shimizu and Hart[35] were able to confirm the results of Steele et al.[75] for the olivine series with the exception that the Si^+ signal was linear (did not pass through a minimum) and therefore a linear Fe/Si relationship was obtained. Shimizu and Hart[35] used high mass resolution ($M/\Delta M = 4400$) and kinetic energy filtering (90 ± 20 eV) methods in two separate experiments to demonstrate the Mg^+ dependence on the presence of iron. The results from the two experiments (~0 and 90 eV secondary ions sampled) are qualitatively similar, although the Si^+ signal relative to the Fe^+ and Mg^+ signals was greater when analyzing higher energy ions. These data suggest that the Mg^+ and Fe^+ ions behave as a binary system described by Shimizu and Hart.[35] The differences in the Si^+ signals reported by the two groups were attributed to the different instruments used (CAMECA IMS 3f and an AEI instrument).[35]

Studying kinetic energy distributions of various elements, Shimizu and Hart[35] observed that the ionic abundances from the high energy population are much closer to the atomic abundances when compared to the low energy population. From this, the suggestion that higher energy ions are less chemically fractionated followed,[35] and thus a reduction in the differences in ionization probability for

the various elements should occur for the higher energy ions. Shimizu and Hart[35] thus concluded that energy filtering not only serves to eliminate molecular ion interferences but also allows the study of higher energy ions and thus the energy dependent nature of the ionization probability of elements.

From the work of Shimizu and Hart[35] on ionization probabilities at low (~0 eV) and high (90 ± 20 eV) energies, it follows that a study of still higher energy (~500 eV) ions would be of value. Using the method of specimen isolation where geologic specimens charge to ~500 V below the secondary accelerating voltage, one is then able to analyze ions of relatively high energy (~500 eV). In this section the analyses of high energy ions (i.e. the specimen isolation method was used) from a series of olivine samples is presented.

2.2.2 Experimental

Eight polished olivine samples varying in composition from fayalite to forsterite supported in a epoxy resin were used in this study. The olivine samples were on loan from Dr. G. Wilson of the University of Toronto. Table 2.2-1 summarizes the electron probe analyses of the olivine samples used, and Table 2.2-2 shows the Mg/Si and Fe/Si atomic ratios.

Again a CAMECA IMS 3f secondary ion microscope was used in this study. References to the CAMECA instrument

Table 2.2-1

Composition of olivine samples.*

Specimen	1	2	3	4	5	6	7	8
MgO	0.00	1.96	16.25	20.61	40.65	43.15	49.01	50.12
SiO_2	29.69	31.39	33.20	33.79	38.28	39.22	40.49	40.54
FeO	66.62	60.75	46.36	43.54	20.47	17.99	8.86	7.43
MnO	2.59	3.08	4.71	1.92	0.37	0.21	0.13	0.12
NiO	0.32	0.24	0.21	0.28	0.22	0.32	0.33	0.10
Na_2O	-	-	-	-	-	-	0.01	0.01
Al_2O_3	-	0.01	-	-	-	-	-	-
K_2O	0.05	0.07	0.05	0.05	0.02	0.03	0.01	-
CaO	0.13	0.09	0.11	0.07	0.05	0.03	0.08	0.05
TiO_2	0.15	0.12	0.09	0.09	0.04	0.02	-	0.01
CrO	0.12	0.08	0.10	0.08	0.01	0.06	0.03	0.05
Total	99.67	98.04	101.08	100.43	100.11	101.03	98.95	98.43

* Weight % oxides determined by electron probe analysis.

Table 2.2-2

Mg/Si and Fe/Si atomic ratios for the olivine samples.*

Specimen No.	Mg/Si	Fe/Si	Fo. Content	Sample Locality
1	0.00	1.88	0.00	Rockport, Mass.
2	0.09	1.60	5.46	Kenora, Ont.
3	0.73	1.17	38.4	Orange County, N.Y.
4	0.91	1.09	45.7	Orange County, N.Y.
5	1.58	0.45	81.0	Rousemont, Qué.
6	1.64	0.38	81.0	Ilmen Mnts., U.S.S.R.
7	1.81	0.18	90.7	Globe, Az.
8	1.84	0.18	91.3	Hintereifel, Germany.

* Determined from the electron probe analyses listed in Table 2.2-1.

have been given in chapter 1. A mass filtered $^{16}O^-$ primary ion beam at a net 15 to 16 kV and ~90 nA was rastered over a 250 × 250 μm area on the sample surface. No conductive coatings were used with the olivine samples and thus the conditions for specimen isolation were easily met. The remainder of the analytical conditions for the method of specimen isolation are discussed earlier in this chapter (sub-section 2.2.1).

For analysis, all of the isotopes for each element, magnesium, silicon and iron (^{24}Mg, ^{25}Mg, ^{26}Mg, ^{28}Si, ^{29}Si, ^{30}Si, ^{54}Fe, ^{56}Fe, and ^{57}Fe) were analyzed with the exception of ^{58}Fe (0.31 % natural abundance). Each isotope was counted for 10 seconds and the set of isotopes was cycled through six times for each point of analysis. In some cases, instability of the primary ion beam caused significant fluctuations in the secondary ion signal. For this reason, each cycle was inspected for anomalous results and those cycles showing anomalous results were omitted from the analysis. On the whole, problems with primary beam stability were infrequent.

2.2.3 Results and Discussion

The increase in molecular ion suppression (M^+/MO^+) with increased kinetic energy filtering has been presented in references 32 and 60, and in section 2.1 of this chapter (specimen isolation versus CEF). As well as using energy filtering to suppress molecular ions, it has also been

postulated that higher energy ions may be less dependent on the host matrix and thus may be quite useful in quantitative analysis.[35]

The SIMS results obtained for the olivine specimens are given in Table 2.2-3. For these analyses, $^{28}Si^{+}$ was used as an internal reference such that the counts from the magnesium and iron isotopes are referenced to those from $^{28}Si^{+}$. The results for $^{26}Mg^{+}$ and $^{56}Fe^{+}$ relative to $^{28}Si^{+}$ have been illustrated in Figures 2.2-2 and 2.2-3. Examination of Figure 2.2-2 ($^{26}Mg^{+}/^{28}Si^{+}$) shows that the $^{26}Mg^{+}$ signal (relative to $^{28}Si^{+}$) passes through a maximun near Fo ~80. This was also the case for the results presented by Steele et al.[75] and Shimizu and Hart,[35] where secondary ions of much lower energy (~0 and 90 eV) were used for analysis.

Examination of the $^{56}Fe^{+}$ signal (relative to $^{28}Si^{+}$), revealed no differences with the results previously observed[35,75] (see Figure 2.2-3). In other words, a linear or near-linear relationship between the $^{56}Fe^{+}/^{28}Si^{+}$ secondary ion intensity and the iron abundance measured by the electron probe is evident. However, it should be pointed out that a line of best fit (solid line) does not pass through the origin and that the intercept is negative. Closer examination of Figure 2.2-3 suggests that a second line of lesser slope (dashed line) that passes very close to the origin may be fitted to the data in the regin of low iron concentration. This effect has been observed by

Table 2.2-3

SIMS ion intensities for the magnesium and iron isotopes relative to $^{28}Si^+$ for the olivine series.*

Sample No.	Fo. Content	$\frac{^{24}Mg^+}{^{28}Si^+}$	$\frac{^{25}Mg^+}{^{28}Si^+}$	$\frac{^{26}Mg^+}{^{28}Si^+}$	$\frac{^{54}Fe^+}{^{28}Si^+}$	$\frac{^{56}Fe^+}{^{28}Si^+}$	$\frac{^{57}Fe^+}{^{28}Si^+}$
1	0.00	0.00178	0.00217	0.00205	1.28	1.89	4.11
2	5.46	0.291	0.318	0.340	1.14	1.66	3.77
3	38.4	1.67	2.20	2.20	0.692	1.02	2.30
4	45.7	1.59	2.60	2.75	0.628	0.933	2.15
5	78.0	2.89	3.78	3.91	0.205	0.301	0.697
6	81.0	2.21	3.30	3.71	0.113	0.180	0.390
7	90.7	2.61	3.09	3.13	0.0447	0.00669	0.147
8	91.3	2.24	3.10	3.19	0.00309	0.00572	0.127

* Average of six cycles.

Figure 2.2-2

Plot of secondary ion intensity for $^{26}Mg^{+}$ relative to $^{28}Si^{+}$ (ordinate) versus the Mg/Si abundance determined by electron probe analysis. The curve has been fitted using a fourth order polynomial.

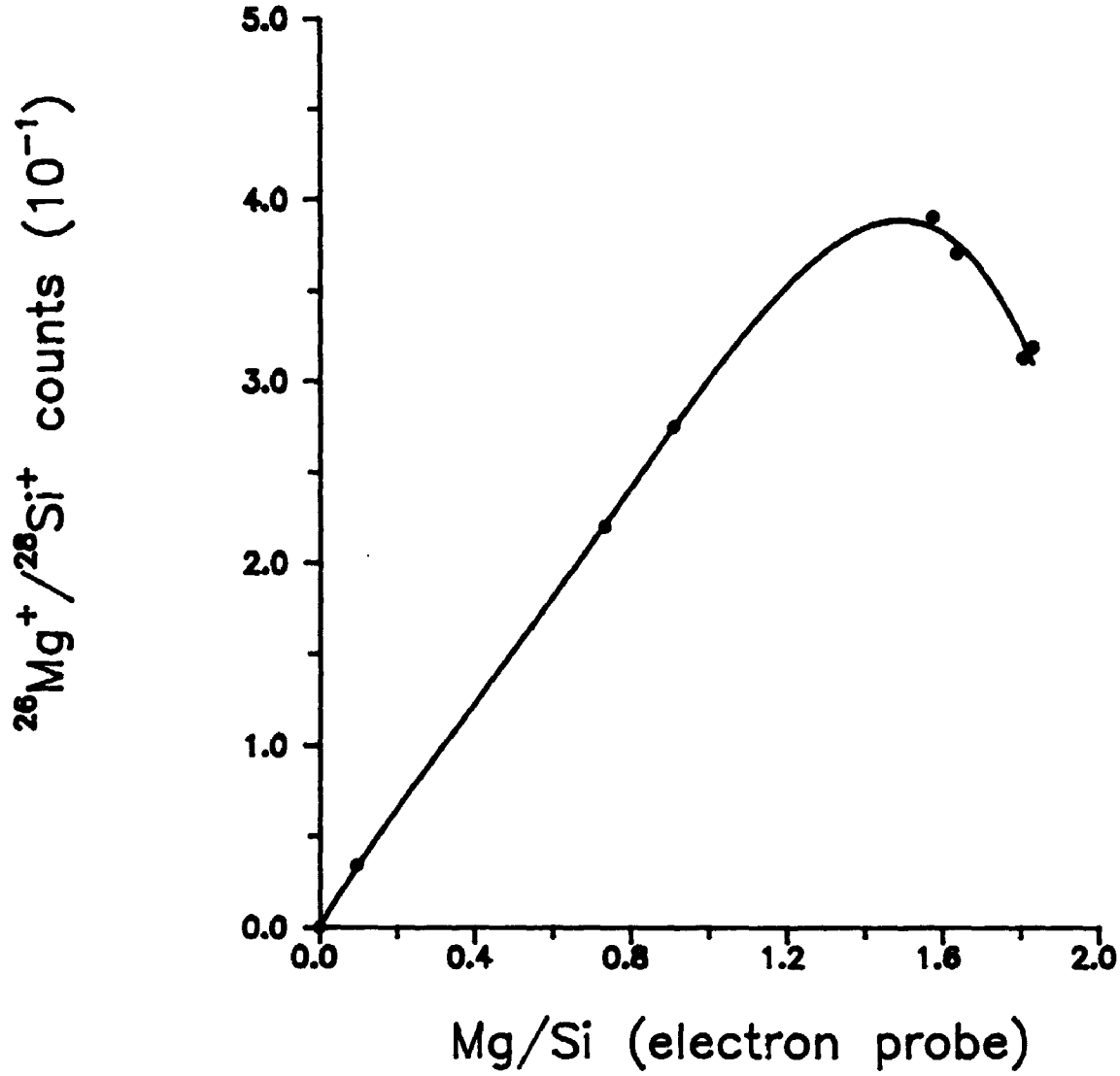
$^{26}Mg^{+}/^{28}Si^{+}$ counts (10^{-1})
5.0
4.0
3.0
2.0
1.0
0.0
0.0
0.4
0.8
1.2
1.6
2.0
Mg/Si (electron probe)

Figure 2.2-3

Plot of secondary ion intensity for $^{56}Fe^{+}$ relative to $^{28}Si^{+}$ (ordinate) versus the Fe/Si abundance determined by electron probe analysis.

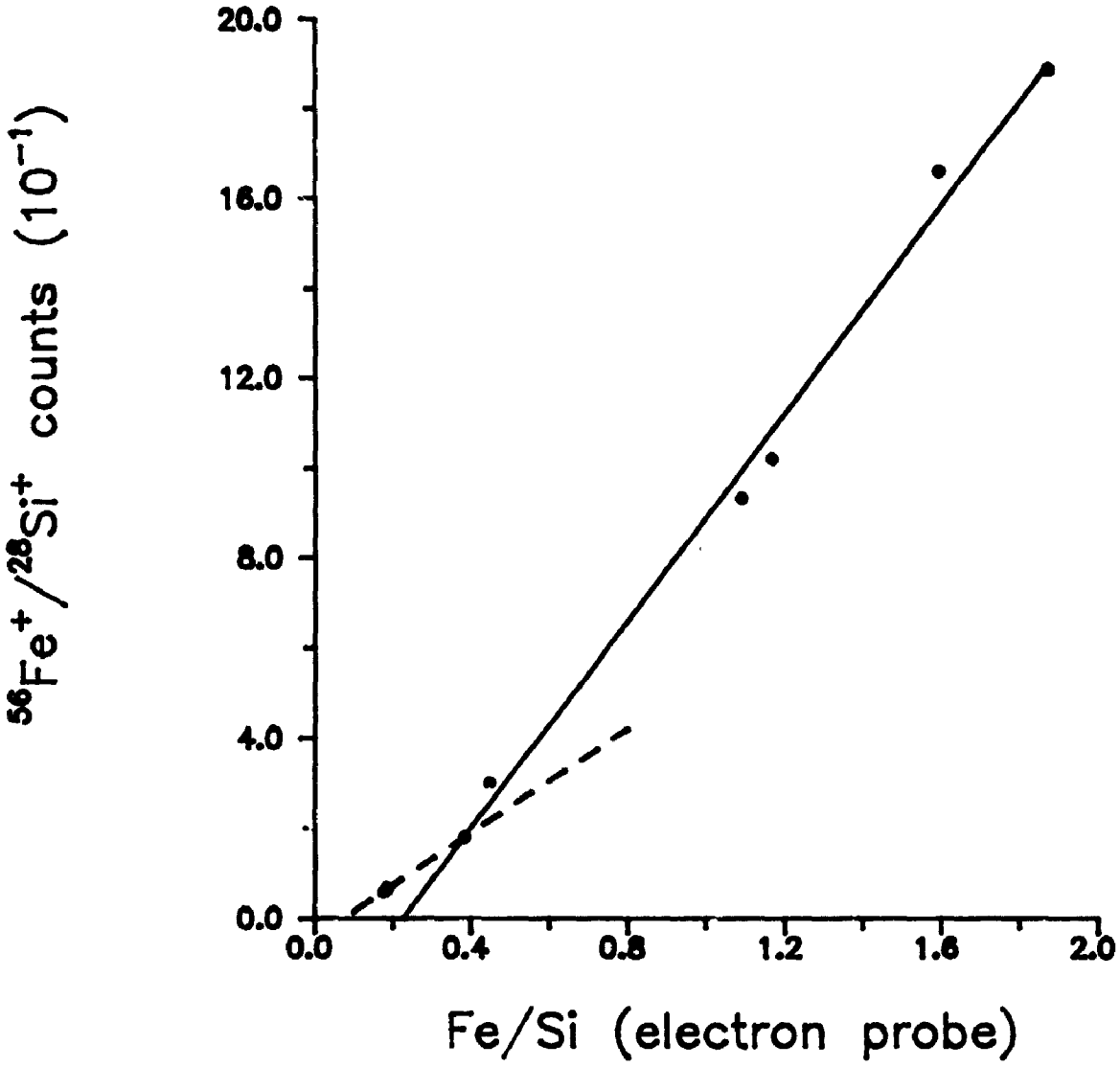
20.0
16.0
12.0
8.0
4.0
0.0
0.0
0.4
0.8
1.2
1.6
2.0
$^{56}Fe^{+}/^{28}Si^{+}$ counts (10^{-1})
Fe/Si (electron probe)

SECONDARY ION MASS SPECTROMETRY AND ITS APPLICATION TO STUDIES IN GEOCHEMISTRY

by

Ian Joseph Muir

Department of Chemistry

Submitted in partial fulfillment
of the requirements for the degree of
Doctor of Philosophy

Faculty of Graduate Studies
The University of Western Ontario
London, Ontario
January, 1989

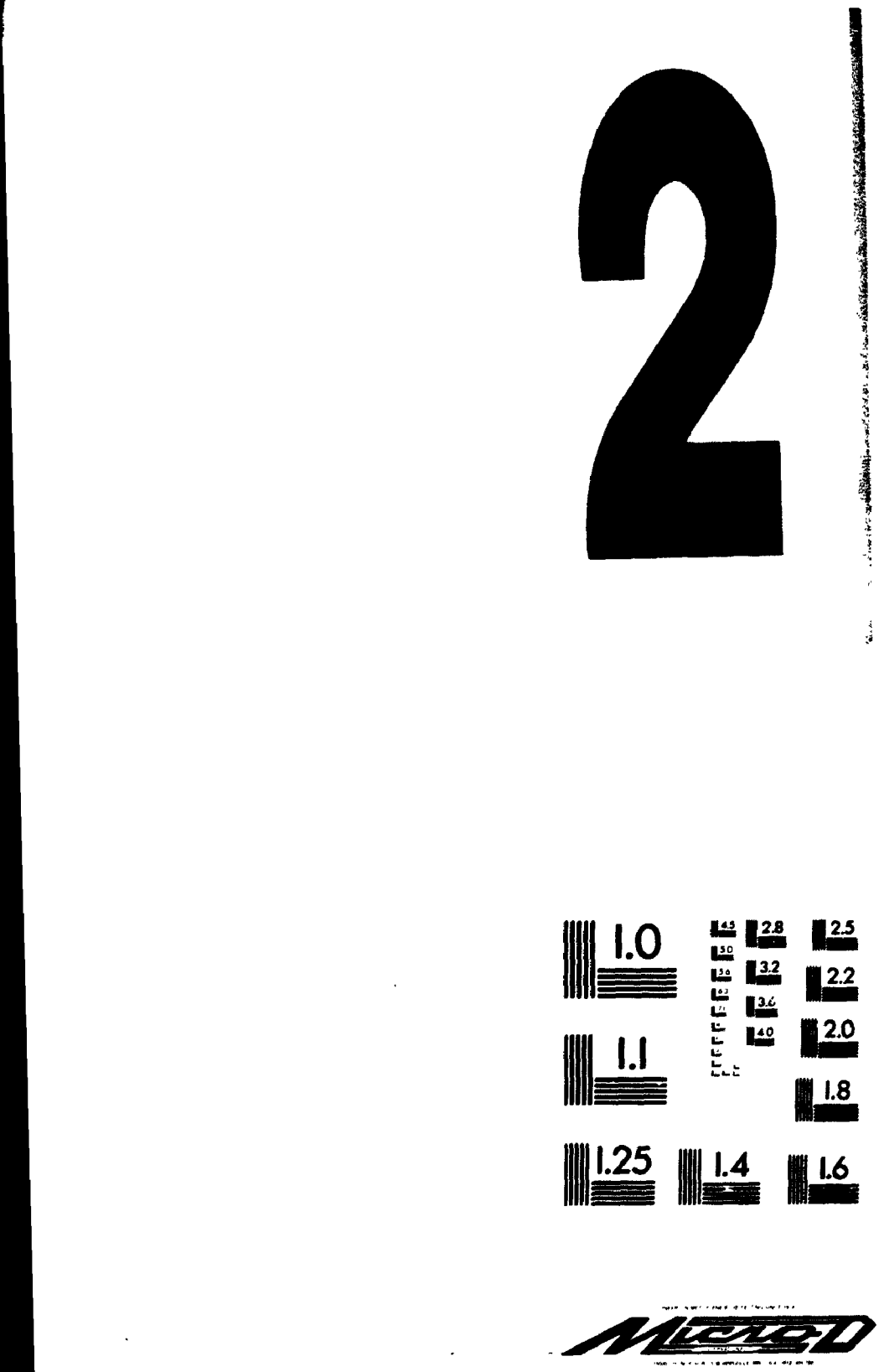

Nesbitt et al.[67] who diluted samples for analysis in a common (Pb_2SiO_4) matrix in an effort to eliminate matrix effects. Nesbitt and his co-workers observed that when the concentration of the element of interest spans over a fairly large range (greater than 10-fold for major elements and greater than 100-fold for trace elements) the calibration curves become distinctly non-linear and the line of best fit does not pass through the origin and its intercept was negative in all cases.

From the results given here, it is obvious that by analyzing high energy (~500 eV) secondaries, one is not able to fully reduce fluctuations in ionization probability due to the influence of the matrix. However, although the curves presented here are non-linear, they are still useful for the accurate determination of forsterite composition for the olivine series.

2.2.4 Conclusions

From the results presented in Figures 2.2-2 and 2.2-3 and Table 2.2-3 it is clear that the Mg^+ and Fe^+ signals (relative to Si^+) are not simply based upon the chemical compostition of each element. It has been proposed before[35,75] that in the case of olivines the effect of the presence of iron is an increase in the secondary ion yield of magnesium (similar to the binary alloy (A-B) discussed by Yu and Reuter[46,47] and Shimizu[48]). These results show the Mg^+/Si^+ ratio passing through a maximum near Fo ~80 where

the iron concentration is becoming low, and then decreasing with further reductions in iron concentrations. These observations suggest the same relationship between iron concentration and magnesium ionization that was proposed earlier.[35,75]

Although the Mg^+ and Fe^+ secondary ion signals relative to Si^+ are not a simple function of the magnesium and iron concentration in the sample respectively, it is still possible to accurately determine olivine compostitions using the curves presented here (see Figures 2.2-2 and 2.2-3) and in references 35 and 75. Similar to the olivine system, Shimizu[76] was able to determine anorthite contents using Al^+/Si^+ intensity ratios and atomic ratios. As for trace element analysis, once the major element chemistry has been determined, closely matching standards are easily used to determine trace element levels.

Even though the probability of ionization for certain elements is dependent on energy,[35] the reduction of matrix effects through the analysis of higher energy (~500 eV) secondary ions was not evident in these experiments. A further investigation into the ionization probabilities for high energy secondary ions is presented in the following chapter.

CHAPTER 3

DISCUSSION OF IONIZATION PROBABILITIES FOR HIGH ENERGY SECONDARY IONS

3.1 Introduction

The application of secondary ion mass spectrometry to a variety of analytical problems ranging from materials science to biology and geology has met with a fair degree of success. Many of the applications of SIMS have dealt with depth profiling of materials and the identification and quantification of trace element contaminants. Since the comparison of secondary ion signals is all that is necessary for these types of analysis, they have in turn become routine. On the other hand, mineral analysis with SIMS is still difficult and has not been widely accepted.

Although mineral analysis with SIMS has been almost exclusively based upon comparison with standards of similar matrix, it would be beneficial to develop a theory of secondary ion emission which one may use to predict ion yields for given elements and/or isotopes. Much interest in secondary ion emission has developed in the physics community and the majority of this interest is concentrated towards low energy secondary ions. Low energy secondary ions are the obvious choice for most analyses since their

abundance far outweighs that for higher energy ions. The use of higher energy ions (anywhere from say 80 to 500 eV) in SIMS analysis of minerals has been shown to have definite advantages. However, within the mineral analysis community there has been little effort to develop a theory describing the emission of high energy secondary ions from mineral targets.

Many authors have discussed the applicability of high energy (~500 eV) secondary ions to the SIMS analysis of mineral specimens.[39,60-70,77] The use of kinetic energy filtering methods for the reduction of molecular ion interferences has been well documented (see references 32, 35, 41, and 59 and the references within). It has also been proposed that high energy ions may be useful for reducing the matrix dependence on secondary ion emission.[35,41,67] However, a mechanism for the emission of high energy secondary ions does not exist.

The emission of secondary ions (low energy) has been discussed in reviews by Williams[2] and Wittmaack.[78] Instrumental factors such as a mass dependence ($M^{1/2}$ or M), and/or a velocity dependence (v^{-1}) are quite often used. A dependence on the first ionization potential has also been proposed. A further description of these ionization theories is found in a publication by Metson et al.[77] Some theories such as the bond breaking model of Slodzian and co-workers[79,80] and the binary system of Shimizu[35,48,81] show remarkable correlation with certain experiments.

However, for many mineral targets it still remains that the quantification of secondary ion yields via ionization theories is quite difficult. An understanding of the influence that the matrix has on secondary ion production is still lacking. Such problems as the modification of the surface due to sputtering and the deposition of electronegative or electropositive elements from the primary beam at the surface contribute further to the effects of the matrix.

Analysis of mineral specimens is somewhat simplified by the high oxygen content of most mineral samples. When using a primary beam of oxygen ions, oxygen saturation levels in the vicinity of the sputtered area are easily reached. Thus, a high and stable positive secondary ion signal is observed. Due to the complex nature of most mineral specimens, the threat of molecular ion interferences generally forces one to use some method of kinetic energy filtering during analysis. As discussed in chapter 2 and the references within, the analysis of high energy ions is not only beneficial for the elimination of molecular ions, but also matrix effects may well be reduced for higher energy ions.

Section 2.2 of chapter 2 dealt with the possible reduction in matrix dependence on the yields of magnesium, iron and silicon for the olivine system presented by Steele et al.[75] Although the effects of the matrix were not completely eliminated when using specimen isolation

conditions, some reduction in matrix effects may have occurred. Since different SIMS instruments were used in the three experiments (Steele et al.,[75] Shimizu and Hart,[35] and this thesis) it is very difficult to assess any reduction or increase in the matrix dependence of the secondary ions at different energies. Ray and Hart[71] however, reported that more consistency in secondary ion intensity was observed when using energy offset voltages greater than that necessary for the removal of molecular ions. In addition, the experiments by Shimizu and Hart[35] comparing low (~0 eV) and high (~80 eV) energy ions do indeed show some energy dependence on secondary ion emission.

Yu and Reuter[46,47] and Shimizu[48,81] have used a binary system to describe the shapes of energy distribution digrams. In the A-B binary alloy where A forms a stronger oxide bond than B, it is said that the presence of A sharpens the energy distribution of B^+, while the presence of B will serve to broaden the energy distribution of A^+. These predictions agree quite well with the results from calcium-aluminum silicate and magnesium-aluminum silicate glasses presented by Shimizu.[48,81] When comparing the FWHM's of energy distributions of $^{40}Ca^+$ from calcite ($CaCO_3$) and feldspar (calcium-aluminum silicate), Slodzian et al.,[82] reported sharper $^{40}Ca^+$ energy distributions for the feldspar matrix where there is an abundance of silicon. Shimizu,[48,81] concluded that these results are in accordance

with the binary alloy since silicon forms the stronger oxide bond.

A number of experimental results have pointed towards a reduction of matrix effects with higher energy ions. From the results of section 2.2 and those of Shimizu and Hart[35] it is apparent that matrix effects are not completely eliminated for high energy ions. This is consistent with Shimizu's[48,81] comments on energy distributions of secondary ions. From Shimizu's work[48,81] the effect of silicon is to sharpen the energy distribution of the other secondary ion signals (those which come from elements that form weaker oxide bonds). This change in the shape of the energy distribution diagrams leads to changes in the high energy as well as the low energy secondary ion yields. It must be emphasized however, that the changes in the secondary ion intensities at higher energies are much more subtle as indicated by common energy distribution plots at these energies. Experiments dealing with the yields of high energy secondary ions are therefore necessary if one is to be able to derive some kind of relationship between elemental concentrations and the emission of high energy secondary ions.

The purpose of this chapter (and a previous publication[77]) is to report the relative ionization yields for a variety of elements under both specimen isolated and conventional energy filtering methods analyzing secondary ion energies of ~500 and 125 eV respectively. A comparison

of these yields and attempts to fit them to some simple model of ionization will also be discussed.

3.2 Experimental

The ion yield results presented in this chapter were obtained from an NBS standard silicate glass (SRM 610). The NBS standard glass was on loan from H.A. Storms of the General Electric Company, Pleasanton, California. The NBS SRM 610 glass contains 61 trace elements at nominal concentrations of ~500 ppm. The composition of this glass (NBS SRM 610) is given in Table 3.2-1. In some cases, measured compositions for certain elements in the glass were somewhat different from the given nominal concentrations (N.D. MacRae, personal communication). These deviations are generally less than 15 % and therefore are not expected to affect any of the conclusions drawn from the presented data.

The isotope of each element chosen for analysis was selected on the basis of natural abundance of the isotope and minimal possibility of any interferences from other isotopes (of different elements) and/or molecular ions. Therefore, the chosen isotopes were generally interference free and in significant abundance.

All of the results presented in this chapter were obtained using a CAMECA IMS 3f secondary ion microscope.[1,23,58] Slight modifications[61,62] had been made to the instrument. A primary beam of mass filtered $^{16}O^-$ ions at a net 15 to 16 kV and 150 to 200 nA was used. For

Table 3.2-1

Nominal concentrations of NBS SRM 610 glass standard.*

Element	Atom %	Weight %
O	59.7191	46.3300
Na	9.3201	10.3900
Al	0.8087	1.0580
Si	24.6972	33.6400
Ca	4.4147	8.5800
Li	0.1486	0.0500
Be	0.1144	0.0500
B	0.0670	0.0351**
F	0.0543	0.0500
Mg	0.0424	0.0500
P	0.0333	0.0500
S	0.0322	0.0500
Cl	0.0291	0.0500
K	0.0243	0.0461**
Sc	0.0229	0.0500
Ti	0.0188	0.0437**
V	0.0202	0.0500
Cr	0.0198	0.0500
Mn	0.0182	0.0485**
Fe	0.0169	0.0458**
Co	0.0136	0.0390**
Ni	0.0161	0.0459**
Cu	0.0144	0.0444**
Zn	0.0137	0.0433**
Ga	0.0148	0.0500
Ge	0.0142	0.0500
As	0.0138	0.0500
Se	0.0131	0.0500
Rb	0.0130	0.0426**
Sr	0.0122	0.0519**
Y	0.0116	0.0500
Zr	0.0113	0.0500
Nb	0.0111	0.0500
Mo	0.0107	0.0500
Ag	0.0049	0.0254**
Cd	0.0092	0.0500
In	0.0090	0.0500
Sn	0.0087	0.0500
Sb	0.0085	0.0500
Te	0.0081	0.0500
Cs	0.0078	0.0500
Ba	0.0075	0.0500
La	0.0074	0.0500
Ce	0.0074	0.0500

Table 3.2-1 continued

Element	Atom %	Weight%
Pr	0.0073	0.0500
Nd	0.0071	0.0500
Sm	0.0069	0.0500
Eu	0.0068	0.0500
Gd	0.0066	0.0500
Tb	0.0065	0.0500
Dy	0.0063	0.0500
Ho	0.0063	0.0500
Er	0.0062	0.0500
Tm	0.0061	0.0500
Yb	0.0060	0.0500
Lu	0.0059	0.0500
Hf	0.0058	0.0500
Ta	0.0057	0.0500
W	0.0056	0.0500
Re	0.0055	0.0500
Au	0.0003	0.0025**
Tl	0.0006	0.0062**
Pb	0.0042	0.0426**
Bi	0.0049	0.0500
Th	0.0040	0.0455**
U	0.0040	0.0462**

* from H. A. Storms.

** analyzed (H. A. Storms).

the measurements under specimen isolated conditions, all of the slits and apertures (including the energy slit) were fully opened such that sufficient secondary ion intensity was available. As for the measurements with conventional energy filtering (CEF) methods a voltage offset of -125 V was used with a energy acceptance (energy slit) of ±10 eV. Depending upon the secondary ion intensity observed, the counting time for each isotope was either 5 or 10 seconds. Each set of elements (generally 7 isotopes and ^{30}Si as an internal reference) was cycled through four or five times for each point of analysis. To check reproducibility and sample homogeneity, two or three points of analysis for each set of elements were obtained on at least two different days. From the data collected, there was no evidence for sample inhomogeneity and the reproducibility was excellent. In general, the standard deviations for the calculated yields were 3 to 6 % but for some of the rare-earth elements, the deviations were up to ~15 %.

The relative ion yields (relative to $^{30}Si^{+}$) were calculated from the following equation:

$$\frac{M^+}{Si^+} = \frac{I_{M^+}}{I_{Si^+}} \times \frac{Ab_{Si}}{Ab_M} \times \frac{C_{Si}}{C_M}$$

where $\frac{M^+}{Si^+}$ = ion yield of element M relative to Si.

$\frac{I_{M^+}}{I_{Si^+}}$ = observed ion intensity of M^+ relative to Si.

Ab_{Si} = natural abundance of the Si isotope used as an internal reference.

Ab_M = natural abundance of the isotope of element M used for analysis.

C_M = concentration of element M in NBS SRM 610.

C_{Si} = concentration of Si in NBS SRM 610.

As in the previous chapter, the specimen(s) for analysis were not coated with any conducting material, thus making specimen isolation conditions possible. The NBS standard silicate glass routinely charged up to a potential some 500 V below that of the secondary accelerating voltage.

3.3 Results and Discussion

The relative ion yield results obtained from the NBS standard silicate glass are presented in Table 3.3-1 as well as Figures 3.3-1 and 3.3-2 for specimen isolation (~500 eV secondary ions) and CEF (125 ± 10 eV secondary ions) conditions respectively. When comparing the ion yields from both forms of energy filtering, the yields appear to be qualitatively similar. In both forms of energy filtering the yields span over a range of approximately three orders

Table 3.3-1

Relative ion yields from NBS SRM 610 measured using specimen isolation and conventional energy filtering (CEF) techniques. See text for explanation of relative ion yields (Ion yields relative to $^{30}Si^{+}$).

Element	Isotope Analyzed	Specimen Isolation	CEF Conditions
Li	7	1.00×10^{0}	1.99×10^{0}
Be	9	2.41×10^{0}	2.34×10^{0}
B	11	1.57×10^{0}	1.01×10^{0}
F	19	2.74×10^{-2}	1.41×10^{-2}
Na	23	8.17×10^{-1}	8.62×10^{-1}
Mg	24	3.09×10^{0}	2.52×10^{0}
Al	27	2.27×10^{0}	2.15×10^{0}
P	31	2.09×10^{-1}	1.21×10^{-1}
S	32	5.78×10^{-2}	7.63×10^{-2}
Cl	35	1.95×10^{-2}	9.61×10^{-3}
K	39	5.58×10^{-1}	8.25×10^{-1}
Ca	40	2.43×10^{0}	2.99×10^{0}
Sc	45	2.22×10^{0}	3.09×10^{0}
Ti	47	1.82×10^{0}	2.49×10^{0}
V	51	1.18×10^{0}	1.49×10^{0}
Cr	52	8.17×10^{-1}	1.00×10^{0}
Mn	55	7.09×10^{-1}	7.71×10^{-1}
Fe	56	5.46×10^{-1}	1.28×10^{0}
Co	59	2.54×10^{-1}	2.67×10^{-1}
Ni	58	1.74×10^{-1}	1.63×10^{-1}
Cu	63	6.47×10^{-2}	7.24×10^{-2}
Zn	66	2.82×10^{-2}	3.04×10^{-2}
Ga	69	1.01×10^{-1}	1.61×10^{-1}
Ge	74	5.90×10^{-2}	9.16×10^{-2}
As	75	1.04×10^{-2}	1.12×10^{-2}
Se	80	2.74×10^{-3}	1.31×10^{-2}
Rb	85	2.54×10^{-1}	3.95×10^{-1}
Sr	88	1.07×10^{0}	1.53×10^{0}
Y	89	1.19×10^{0}	1.85×10^{0}

Table 3.3-1 continued

Element	Isotope Analyzed	Specimen Isolation	CEF Conditions
Zr	90	9.93×10^{-1}	1.49×10^{0}
Nb	93	5.71×10^{-1}	8.69×10^{-1}
Mo	98	3.21×10^{-1}	4.67×10^{-1}
Ag	107	8.62×10^{-3}	1.63×10^{-2}
Cd	114	2.34×10^{-3}	5.58×10^{-3}
In	115	2.43×10^{-2}	5.51×10^{-2}
Sn	120	2.44×10^{-2}	5.38×10^{-2}
Sb	121	1.99×10^{-3}	8.40×10^{-3}
Te	128	1.48×10^{-3}	1.83×10^{-3}
Cs	133	1.19×10^{-1}	1.82×10^{-1}
Ba	138	5.31×10^{-1}	6.94×10^{-1}
La	139	8.10×10^{-1}	1.00×10^{0}
Ce	140	8.00×10^{-1}	1.04×10^{0}
Pr	141	8.47×10^{-1}	1.05×10^{0}
Nd	146	7.85×10^{-1}	9.85×10^{-1}
Sm	152	9.08×10^{-1}	1.08×10^{0}
Eu	153	9.01×10^{-1}	1.08×10^{0}
Gd	158	9.31×10^{-1}	1.10×10^{0}
Tb	159	8.69×10^{-1}	9.61×10^{-1}
Dy	163	7.71×10^{-1}	9.68×10^{-1}
Ho	165	8.00×10^{-1}	8.69×10^{-1}
Er	166	7.26×10^{-1}	8.77×10^{-1}
Tm	169	6.96×10^{-1}	8.25×10^{-1}
Yb	174	6.67×10^{-1}	8.00×10^{-1}
Lu	175	5.41×10^{-1}	6.69×10^{-1}
Hf	178	2.18×10^{-1}	4.27×10^{-1}
Ta	181	1.15×10^{-1}	2.49×10^{-1}
W	184	4.89×10^{-2}	1.30×10^{-1}
Re	187	4.00×10^{-3}	1.02×10^{-1}
Pb	208	1.36×10^{-3}	7.01×10^{-3}
Th	232	1.53×10^{-1}	4.79×10^{-1}
U	238	1.15×10^{-1}	4.08×10^{-1}

Figure 3.3-1

Secondary positive ion yield (M^+) relative to $^{30}Si^+$ for specimen isolated conditions (~500 eV secondary ions) due to bombardment by an $^{16}O^-$ primary ion beam at 15-16 kV and ~200 nA (ordinate) plotted against atomic number of the secondary ion.

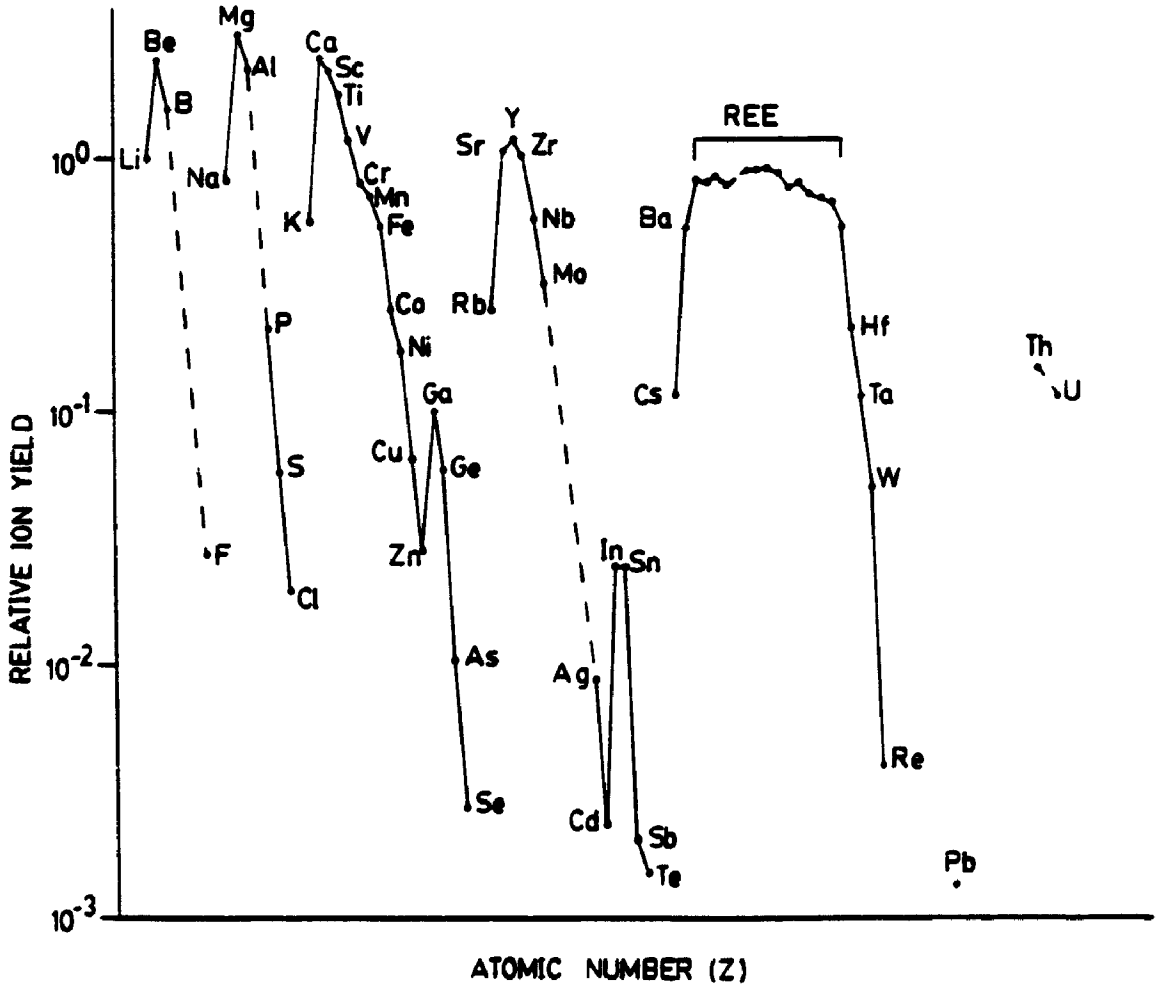
RELATIVE ION YIELD
10^0
10^{-1}
10^{-2}
10^{-3}
ATOMIC NUMBER (Z)
Li
Be
B
Na
Mg
Al
K
Ca
Sc
Ti
V
Cr
Mn
Fe
Co
Ni
Cu
Zn
Ga
Ge
As
Se
Rb
Sr
Y
Zr
Nb
Mo
Ag
Cd
In
Sn
Sb
Te
Cs
Ba
REE
Hf
Ta
W
Re
Pb
Th
U
F
P
S
Cl

Figure 3.3-2

Secondary positive ion yield (M^+) relative to $^{30}Si^+$ for CEF conditions (125 ± 10 eV secondary ions) due to bombardment by an $^{16}O^-$ primary ion beam at 15-16 kV and ~200 nA (ordinate) plotted against atomic number of the secondary ion.

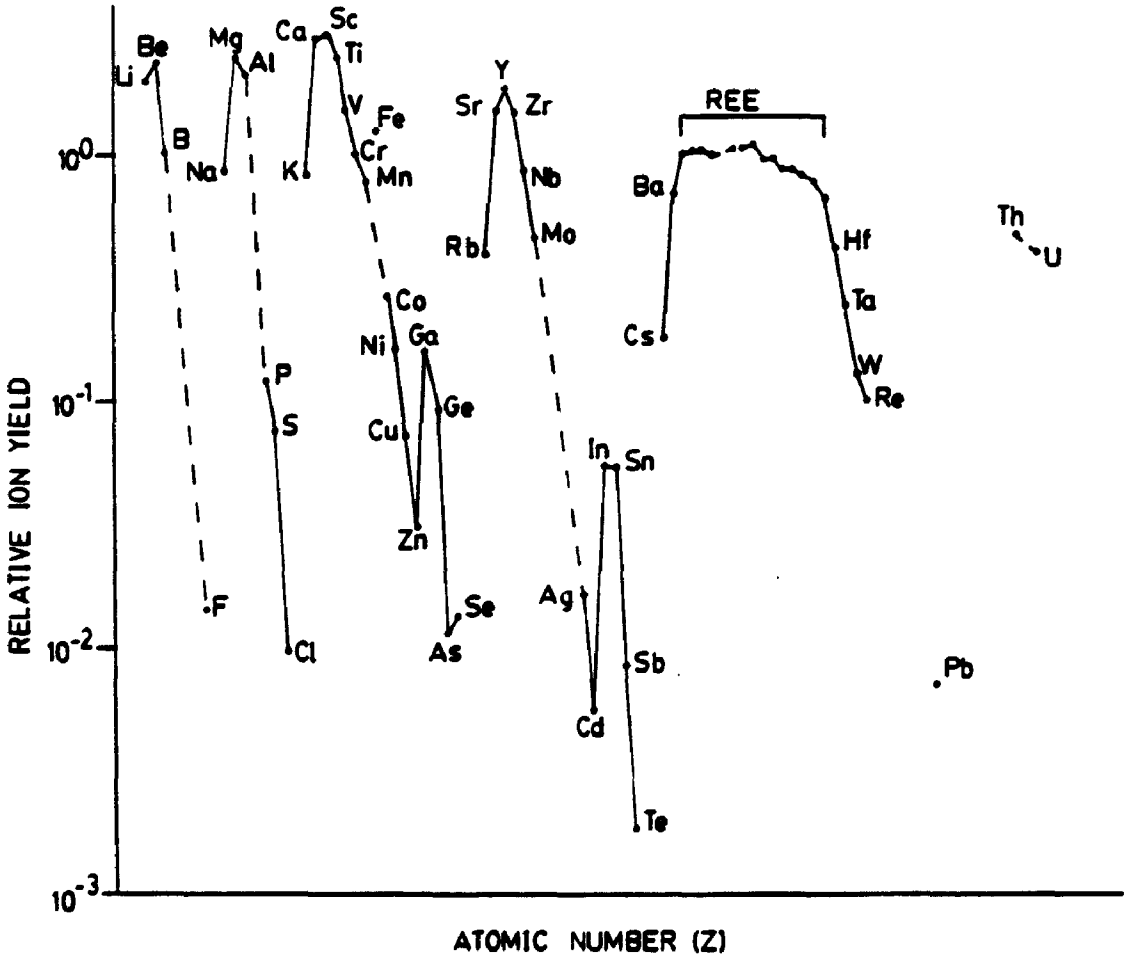
RELATIVE ION YIELD
10^{0}
10^{-1}
10^{-2}
10^{-3}
ATOMIC NUMBER (Z)
Li
Be
B
Na
Mg
Al
Ca
Sc
Ti
V
Fe
Cr
Mn
K
P
S
F
Cl
Co
Ni
Ga
Cu
Ge
Zn
As
Se
Y
Sr
Zr
Nb
Rb
Mo
REE
Ba
Cs
Hf
Ta
W
Re
Th
U
In
Sn
Ag
Sb
Cd
Te
Pb

of magnitude (see Figures 3.3-1 and 3.3-2). This is in marked contrast to similar results presented by Storms et al.[83] for low (~0 eV) energy secondary ions (see Figure 3.3-3). The ion yields at low (~0 eV) energies vary over a range of at least four orders of magnitude. These ion yields at low (0 eV) and high (125 and ~500 eV) energies support the predictions that the production of secondary ions is energy dependent. The results from CEF and specimen isolation conditions suggest that the ionization of sputtered particles is not very dependent upon energy after a certain energy has been reached. The results presented in Table 2.1-5 in chapter 2 also leads to similar conclusions. The later (results in Table 2.1-5) also show little difference in ion yields between glass and crystalline target materials.

Examination of Figures 3.3-1 and 3.3-2 shows the relatively low yield for the alkali metals (compare to the yields for the alkaline earth metals). This fits well with the observations of Shimizu and co-workers[35,48,81] that the energy distributions for the alkali metals (sodium in particular) are generally much sharper than for other elements. Therefore, the positive ion yield of the alkali metals would be greater at lower ion energies, and much lower at higher energies. The bond breaking model of Slodzian and co-workers[79,80] suggests that the emission of alkali metals is quite likely to be from direct ionic emission. This theory also supports the low yields for the

Figure 3.3-3

Relative secondary positive ion yield (M^+) due to O^- bombardment (ordinate) vs. atomic number. H, N, Mg, Ca, As, In, Hg, and Th were determined from compounds, whereas the rest were from the pure element. Taken from reference 83.

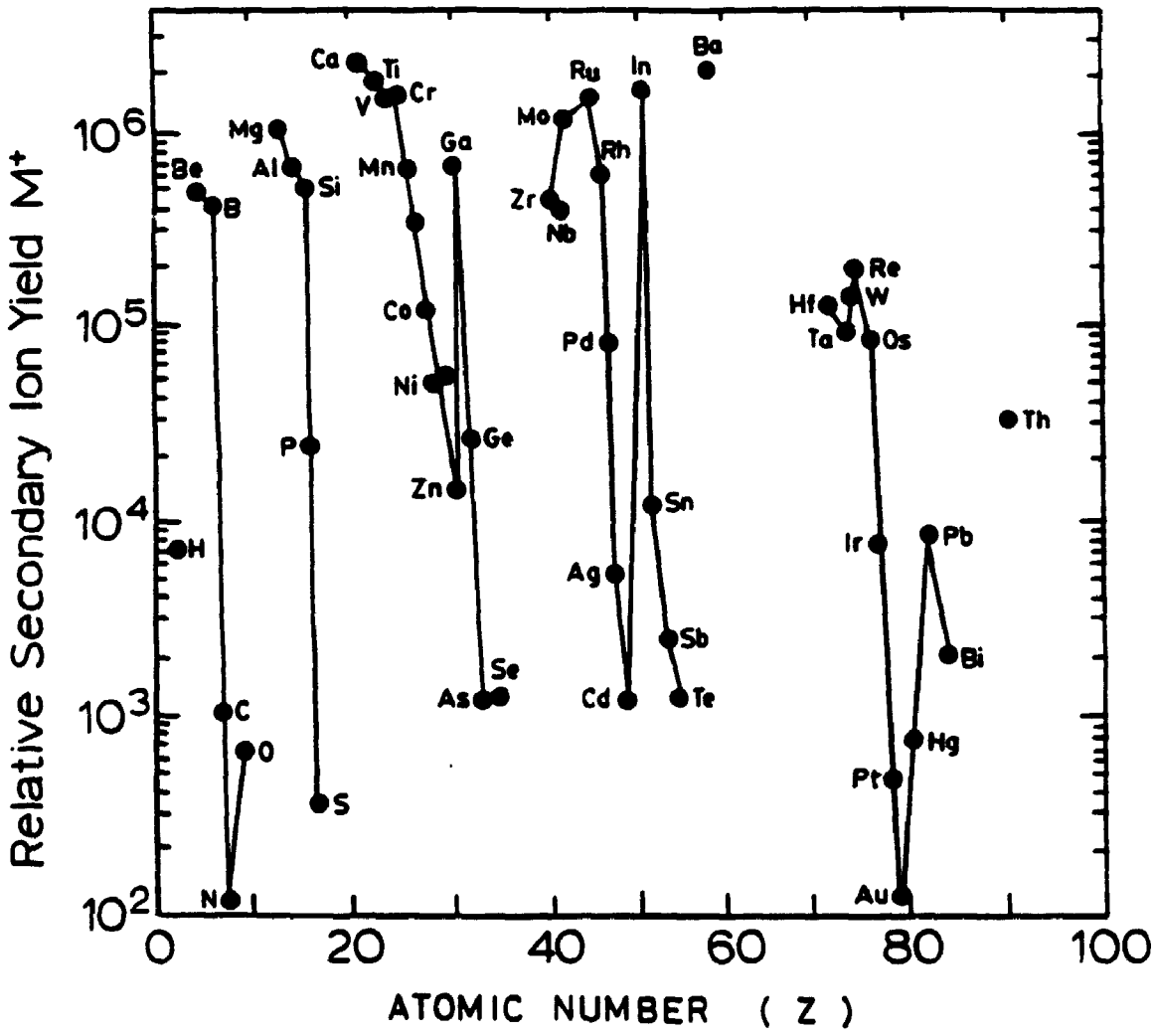
Relative Secondary Ion Yield M+
10^6
10^5
10^4
10^3
10^2
0
20
40
60
80
100
ATOMIC NUMBER (Z)
Ca
Ti
V
Cr
Mg
Al
Si
Mn
Ga
Be
B
Co
Ni
Ge
P
Zn
H
C
O
S
N
Se
As
Ba
In
Ru
Mo
Rh
Zr
Nb
Pd
Sn
Ag
Sb
Cd
Te
Re
Hf
W
Ta
Os
Th
Ir
Pb
Bi
Hg
Pt
Au

alkali metals at the higher ion energies investigated in this study. The yields of low energy ions for lithium, sodium and potassium ions were not presented by Storms et al.[83]

Close examination of Figures 3.3-1 and 3.3-2 show suprisingly high positive ion yields for the halogens (fluorine and chlorine in this study). Lodding et al.[84] have also observed these high yields for the halogens (fluorine and chlorine in his study), however, they offer no mechanism(s), and use this as an example to stress the importance of the use of standards in quantitative determinations.

Although the relative ion yields in specimen isolation and CEF modes are qualitatively similar, it is worth indicating the few anomalies that are present. The yields of the alkali and alkaline earth metals from the first three periods show considerable variance between the two methods of energy filtering (see Figures 3.3-1 and 3.3-2). These differences may be easily explained by subtle changes in the shapes of the energy distribution curves towards higher energies. However, reasons for changes in the shapes of the energy distribution curves are not understood.

Some other discrepancies in the ion yields between the two levels of energy filtering are for iron, selenium and rhenium. It is suspected that the peak observed for iron (mass 56) under CEF conditions may well be contaminated

with molecular ions (possibly $^{28}Si_2^+$), causing the observed intensity to be greater than the actual intensity due to the iron isotope. This may also be the case for selenium and rhenium where the yields in the CEF method are greater than the yields when using specimen isolated conditions. Possible molecular ion interferences at masses 80 (selenium) and 187 (rhenium) are not easily predicted given the matrix composition of the NBS glass. It is also quite likely that some other mechanism(s) may be the cause of these discrepancies. If this is so, these mechanisms are not known at the present.

A similar set of relative ion yield data obtained under specimen isolated conditions were fitted using certain parameters that previous authors have used to explain secondary ion emission at low energies. D.L. Tui of the University of Auckland, Auckland, New Zealand, was responsible for fitting the experimental data. Many authors agree that the yield of positive secondary ions under oxygen bombardment follows an inverse relationship with ionization potential. Wittmaack[78] suggests the following relationship:

$$M^+ \alpha \exp(-AE_{IP})$$

where A = a constant.

E_{IP} = the first ionization potential of M.

If this relationship were to be followed, a semilog plot of the ionization yields (specimen isolation method) versus the first ionization potential should result in a straight line.

However, Figure 3.3-4 illustrates the relatively poor agreement between the high energy positive ion yields and the first ionization potential of each element. Odelius et al.[85] used "corrected ion yields" from the Local Thermal Equilibrium Theory to indicate a relationship between the ionization yield and the ionization potentials of some twenty elements in the low energy region. Also reported, were deviations in this relationship for higher energy (≥60 V) ions. For this reason, similar corrections were not applied to the high energy secondary ions measured using the specimen isolated method in this study.

The next step taken in fitting the experimental ion yields was the application of an "instrument factor", namely a mass or a velocity correction. While some authors have shown a mass dependence ($M^{1/2}$),[86] others have shown a velocity dependence (v^{-1}).[87] Since the secondary ions passing through the electrostatic analyzer are all of similar energy (4500 eV), the two correction factors may then be viewed as somewhat similar. Although not shown here, an attempt at fitting the ion yields from the specimen isolation method using some type of mass correction was made. An $M^{1/2}$ factor did not seem to improve the fit,[77] while the use of an M factor did improve the fit to some extent.[77] Although some mass dependence for the high energy (~500 eV) ion yields was observed,[77] the use of the M factor was not sufficient in correcting over the whole mass range.[77] The successful application of a velocity

Figure 3.3-4

A semilog plot of relative ion yields from NBS 610 under specimen isolated conditions (ordinate) versus first ionization potential. Taken from reference 77.

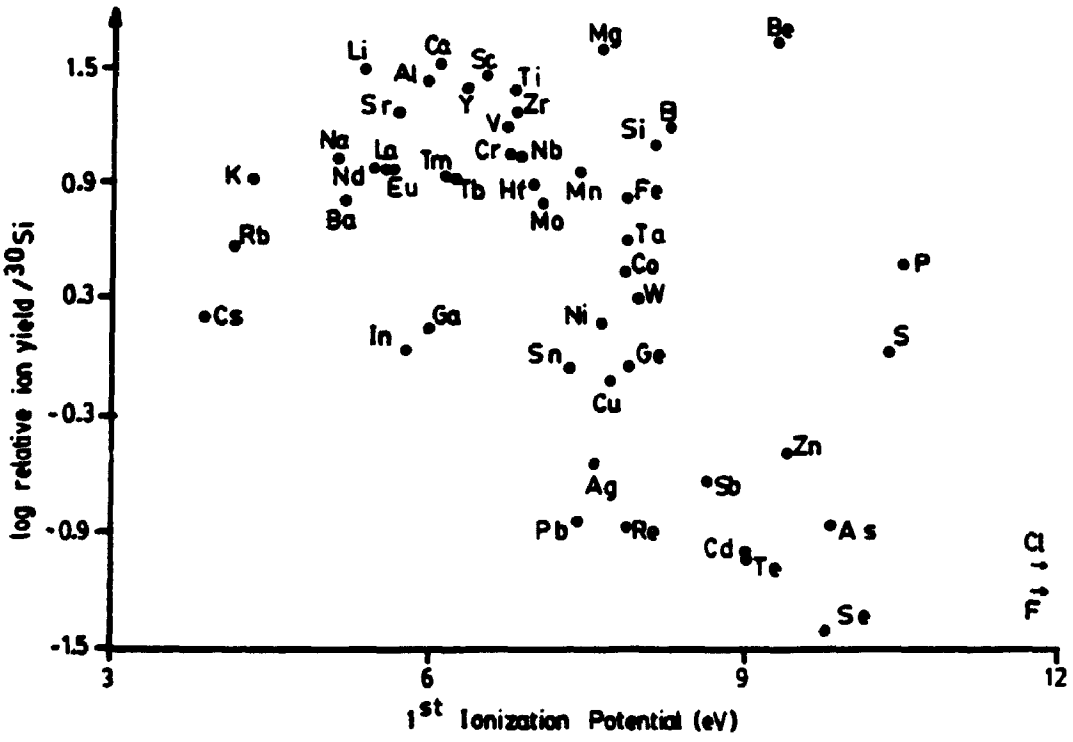
log relative ion yield /30Si
1.5
0.9
0.3
-0.3
-0.9
-1.5
3
6
9
12
1st Ionization Potential (eV)
Li
Ca
Sc
Mg
Be
Al
Ti
Sr
Y
Zr
V
B
Si
Na
La
Tm
Cr
Nb
K
Nd
Eu
Tb
Hf
Mn
Fe
Ba
Mo
Rb
Ta
Co
P
W
Cs
Ga
Ni
In
S
Sn
Ge
Cu
Zn
Ag
Sb
Pb
Re
As
Cd
Te
Cl
F
Se

dependence by Vasile[87] for low energy secondary ions was not used in these attempts to fit the data obtained using specimen isolated conditions. The relationship shown by Vasile[87] was shown to break down at higher energies (>30 eV).

Based upon an improved fit, some authors[86,88] have had success using a mass correction ($M^{1/2}$ and/or M), while Odelius et al.[85] propose a more complex mass correction of $(M/M_{Si})^n$. This correction is again based upon the improved fit of their corrected (LTE theory) data. Attempts to fit high energy (specimen isolation method) ion yields with ionization potentials using the mass dependence suggested by Odelius et al.[85] did not show any systematic variation of n with mass.

The bond breaking model of Slodzian and co-workers[79,80] has also been used as a possible mechanism to explain the yield of secondary ions. In oxygen dominated systems, the bond breaking model implies that secondary ion emission is largely a result of the breaking of a predominantly ionic metal-oxide bond. Therefore the energy necessary for ionization will be reduced by the electron affinity of the oxygen atom. Enhanced ionization yields due to the increasing presence of oxygen are thus readily explained by the bond breaking model. Correlation of the ionization yield data for high energy secondary ions with metal-oxide bond strength is shown in Figure 3.3-5. Again, no systematic relationship is observed, leading one to

Figure 3.3-5

The relationship between oxide bond strength and relative ion yield for the elements in NBS 610. Taken from reference 77.

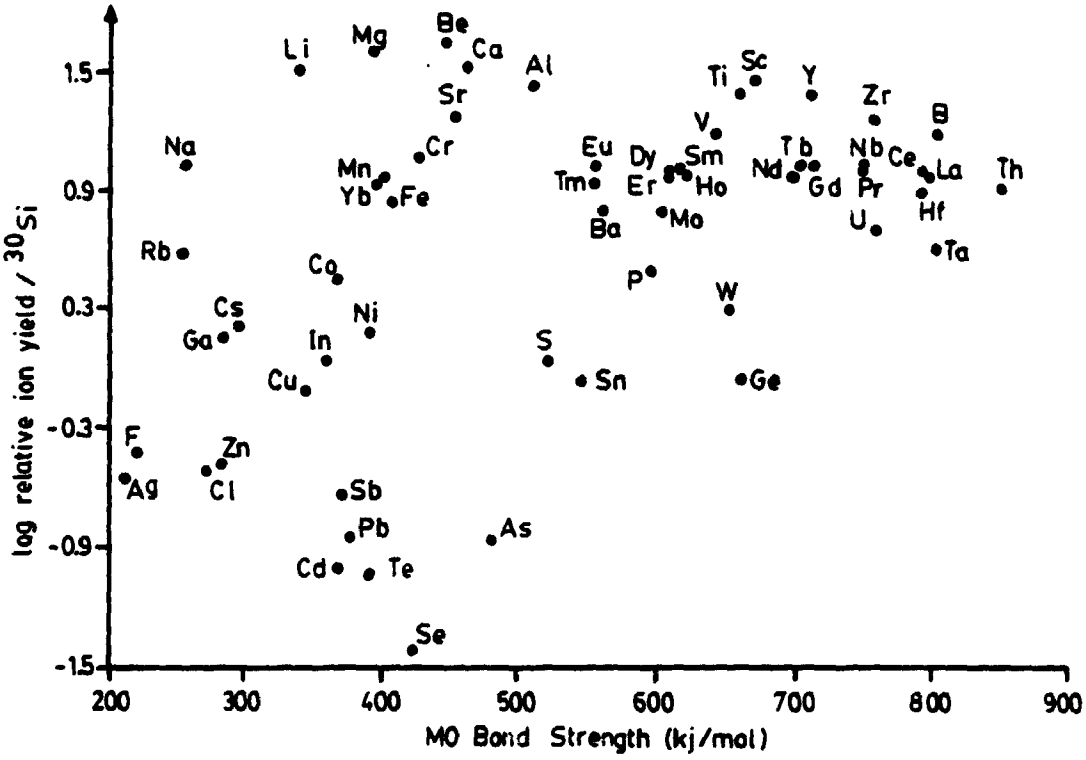
log relative ion yield / ^{30}Si
MO Bond Strength (kj/mol)
1.5
0.9
0.3
-0.3
-0.9
-1.5
200
300
400
500
600
700
800
900
Li
Mg
Be
Ca
Al
Sr
Ti
Sc
Y
Zr
B
V
Na
Cr
Eu
Dy
Sm
Tb
Nb
Ce
La
Th
Mn
Yb
Fe
Tm
Er
Ho
Nd
Gd
Pr
Hf
Ba
Mo
U
Rb
Co
P
Ta
W
Cs
Ni
Ga
In
S
Cu
Sn
Ge
F
Zn
Ag
Cl
Sb
Pb
As
Cd
Te
Se

conclude that there is little connection between high energy ion yields and oxide bond strength. By lowering the energy necessary for ionization, the use of the bond breaking model does not exclude the dependence of ion yields on the ionization potential, and hence the relationship sought earlier between ion yield and ionization potential (Figure 3.3-4), seems more likely.

Without finding any systematic relationship between ion yields and first ionization potential or oxide bond strength, there exists no possible mechanism(s) for explaining the matrix dependence in the production of high energy secondary ions. This results in the inability to predict high energy secondary ion yields using some pre-established ionization model.

Up until this point, comparison of the yields for high energy secondary ions with low energy ionization models has been done assuming that the sputter yield (yield of the total sputtered material) for the high energy population is identical to that for the low energy population. Therefore, a matrix dependence on the energy distribution of the total sputtered population has been omitted. The ion yield can be viewed as the fraction of the sputtered population that is ionized (i.e. the following equation).[77]

$$S^+(E) = N^+(E)/N_0(E)$$

where $S^+(E)$ = ion yield of element S at energy E.

$N^+(E)$ = number of ions ejected at energy E of element S.

$N_0(E)$ = total number of sputtered particles containing S ejected with energy E.

While $N^+(E)$ is easily measured using the mass spectrometer (i.e. what is observed in these experiments), $N_0(E)$ at high energies is very difficult to predict. Assuming that the low energy region is more sensitive to matrix effects, any minor alteration to $N_0(E)$ at low energies (greatest population) may then lead to differences in $N_0(E)$ at higher energies. From this argument, it follows that the high energy ions are not independent of low energy ions and/or sputter yields. Therefore, the prediction of high energy secondary ion yields should in turn be no easier than predicting secondary ion yields from the low energy region.

3.4 Conclusions

The promise of using high energy (~100 eV and greater) secondary ions for quantitative SIMS analysis of geologic materials has been shown by many authors. From the ion yields relative to $^{30}Si^+$ for the two forms of energy filtering it appears that above a certain secondary ion energy, the production of secondary ions becomes less energy dependent or possibly even independent of secondary ion energy. However, between the low (~0 eV) and high

(~100 eV and greater) energy regions this is not the case. A factor of ten difference between the low energy ion yields of Storms et al.[83] and those of higher energy (125 and ~500 eV) energy from this study was observed. The compression of ion yields towards high energy has lead to the proposal that matrix effects may be reduced when analyzing higher energy ions. The ion yields measured under CEF and specimen isolation conditions were fitted to various models in an attempt to describe the ionization process.

Poor agreement was observed between the ion yield and the first ionization potential of the elements. The inclusion of an "instrument factor" (M^n where previous authors have used n = 1/2 or 1) was found to improve the fit somewhat,[77] but a satisfactory fit for all elements was not found. This supports the conclusion of Wittmaack[78] that these parameters are merely "fitting factors" which may or may not even exist. The bond-breaking model of Slodzian and co-workers[79,80] and the binary system of Shimizu[35,46-48,81] are helpful in explaining the low yield of the alkali metals at high energies.

The main conclusion to be drawn from these data is that although matrix effects for high energy ions are somewhat reduced, the matrix effects at the low energy region still remain, and thus still affect the high energy population to some extent. Assuming that the total sputtered population is susceptible to matrix effects, the matrix dependence of the total sputtered yield makes it

exceedingly difficult to model high energy ion yields. Testing this hypothesis is possible by investigating the energy distributions of the total sputtered population over the energy range of 0 to 500 eV. The complete and accurate description of these energy distributions would be a somewhat intimidating experimental task.

As a final comment, the relative stability of the high energy secondary ion signal (yields) should lend itself to some simple ionization model, however this does not appear to be the case since some chemical matrix effects still remain. It seems that since most of the problems with sputtering occur well below say 80 eV, the ion yields would likely be a function of the first ionizaiton potential of the element, or some other process for the decay of the excited sputtered particle to the ion. This type of relationship was not evident from the experiments in this study. As for a satisfactory mechanism(s) for the production of high energy secondary ions, there is nothing available at the present time, and therefore, the use of closely matching standards still remains the prime choice for quantitative analysis by secondary ion mass spectrometry.

CHAPTER 4

ANALYSES OF RARE-EARTH ELEMENTS IN MINERALS BY SIMS

4.1 Introduction

The elemental distribution of the rare-earth elements [REE; defined as Y (Z = 39) and the lanthanides (Z = 57-71)] is of importance to geochemists for obtaining information pertaining to the environment of crystallization or recrystallization.[89] A valuable technique for the in situ analysis of REE would require detection limits in the ppm to ppb range. Neutron activation analysis and mass spectroscopic isotope dilution are the most commonly used methods for REE analysis in rocks and minerals. Both of these techniques are sensitive in the range of a few ppm, however they are almost exclusively used for the analysis of bulk samples.

The application of focussed beam (microprobe) techniques to the analyses of REE has received considerable attention in the literature over the past decade or so. These techniques are, electron probe microanalysis (EPMA), particle (proton)-induced X-ray emission (PIXE), X-ray fluorescence using synchrotron radiation (SXRF), and secondary ion mass spectrometry (SIMS). Due to its poor sensitivity, ~100 ppm, low peak-to-background ratios and the

overlap of peaks in the X-ray continuum, EPMA is usually applicable to the analysis of REE-enriched phases only. The greater signal-to-background ratios and thus increased sensitivity that are available using PIXE have lead to its use for the analysis of REE.[90] Hanson et al.[91] and Rivers et al.[92] are developing a technique using synchrotron radiation to perform XRF analysis for REE in which the theoretical detection limits are in the range of 1 ppm. The major drawback with this technique is the loss of spatial resolution due to the large size of the synchrotron beam. Synchrotron beams are usually >5 mm^2, but Rivers et al.[92] and Smith et al.[93] predict a focussed beam of ~20 μm and detection limits in the ppb range through the use of yet more sophisticated equipment. In a recent publication, Thompson et al.[94] present the details of an X-ray microprobe with a spot size of ~10 μm and femtogram sensitivity when using very thin specimens.

The features that make SIMS a promising tool for in situ analysis of geologic specimens are its ppm sensitivity, complete mass range analysis, and micron scale resolution.[31,35] However, such problems as the occurrence of molecular ions at similar masses as elemental ions, the uncontrolled surface charging of nonconductors, and the influence of the matrix in the production of secondary ions[2,3] have all kept SIMS from reaching its potential.

The two most common approaches in geologic SIMS have been the use of: (a) high mass resolution,[40] or (b) some

form of kinetic energy filtering.[32,35,41,60] Kinetic energy filtering is based on the much narrower energy distribution of the molecular than elemental ions[32,35] such that by analyzing the high energy ion population, the ratio of elemental to molecular ions is increased by a few orders of magnitude. Two different forms of energy filtering have been used to date; conventional energy filtering and the method of specimen isolation. These two techniques have been discussed in previous chapters.

The above forms of SIMS analysis have all been applied to the analysis of REE in geologic specimens. S.J.B. Reed[73,74,95-97] first used high mass resolution to investigate the molecular ion interferences in the REE region of the mass spectrum, and from the information gained, the mass spectra obtained using less mass resolution (such that sensitivity is not sacrificed) were further evaluated. E. Zinner's group[41,72] tend to prefer the use of conventional kinetic energy filtering to remove most of the complex molecular ions from the mass spectra, and then rely on the deconvolution of peaks to evaluate the few remaining molecular ions (oxides of the REE, and in some cases fluorides of the REE, which are generally the most difficult to resolve using conventional kinetic energy filtering techniques). Both of these approaches have been successfully used with detection limits in the sub-ppm range. Using the method of specimen isolation, MacRae and

Metson[66] reported the analysis of REE down to <1 ppm in plagioclase and pyroxene grains without the need for corrections of interfering molecular ions.

This chapter and a previous publication,[68] report the analyses of REE in monazite and an augite grain using the method of specimen isolation and compare these analyses with those obtained using instrumental neutron activation analysis (INAA) (both grains) and the electron microprobe (monazite only). These results show the accuracy and ease of the specimen isolation method for both high (wt %) and trace (~1 ppm) REE concentrations.

4.2 Experimental

A monazite specimen from New Mexico, U.S.A., and an augite sample of unknown locality were used in this study. The monazite specimen was supplied by R.G. Jonasson of the University of Western Ontario, while N.D. MacRae was responsible for supplying the augite sample. The analyses of these two samples are presented in Tables 4.2-1 and 4.2-2 respectively. INNA analyses were obtained from Nuclear Activation Services in Hamilton, Ontario, and the EPMA analysis was carried out at the Geological Survey of Canada in Ottawa, Ontario. These samples were chosen on the basis of a wide variation of major-element chemistry (i.e. one silicate and one phosphate grain), as well as extreme differences in REE concentrations; the augite grain

Table 4.2-1

Elemental analysis (wt% oxides) for New Mexico monazite.

	EPMA*	INAA**
P_2O_5	27.70	27.70†
CaO	1.18	1.18†
ThO_2	11.56	17.07
UO_2	0.55	0.23
Y_2O_3	0.69	0.98
La_2O_3	9.16	9.15
Ce_2O_3	23.91	16.75
Pr_2O_3	3.58	2.46
Nd_2O_3	11.44	9.45
Sm_2O_3	4.55	3.48
EuO	-	0.15
Gd_2O_3	4.88	3.92
Tb_2O_3	-	0.92
Dy_2O_3	1.05	2.30
Ho_2O_3	-	0.16
Er_2O_3	0.13	0.21
Tm_2O_3	-	0.02
Yb_2O_3	0.17	0.07
Lu_2O_3	-	0.01
Total	100.55	96.21

* Analysis by G.S.C., Ottawa, Ontario.

** Analysis by Neutron Activation Services, McMaster Nuclear Reactor, Hamilton, Ontario (conversion from ppm of the element to weight percent of the oxide has been made).

† P and Ca data taken from EPMA since they were not analyzed by INAA.

Table 4.2-2

Elemental analysis for Augite A (major elements are in weight percent oxides and the rare-earth elements are in ppm).

Specimen	Augite A
SiO_2*	49.85
TiO_2	0.07
Al_2O_3	0.47
Fe_2O_3	18.41
MnO	1.76
MgO	5.22
CaO	23.29
Na_2O	0.73
K_2O	0.05
Cr_2O_3	0.07
Total	99.92
La**	1.3
Ce	4.0
Nd	5.0
Sm	1.96
Eu	0.21
Gd	1.9
Dy	2.0
Er	-
Yb	1.85

* Major elements by EPMA.

** REE analysis by Neutron Activation Services, McMaster Nuclear Reactor, Hamilton, Ontario.

containing REE at the ppm level, whereas REE are present in the monazite in the order of as much as 15 wt.%.

A CAMECA IMS 3f secondary ion microscope was used in this study. The sample holder design and pre-amplification system were modified.[61,62] The dead time of the counting circuit was ~70 ns. The maximum count rates were on the order of 10^6 counts per second, and therefore dead time corrections were not necessary. A mass filtered primary beam of $^{16}O^-$ ions at a net 15 to 16 kV and ~100 nA was used. The method of specimen isolation led to a large primary beam diameter (~70 to 100 μm). To achieve sufficient intensity during analysis with specimen isolated conditions, it is also necessary to open up the entrance and exit slits along with the apertures of the secondary column and the energy window (±65 eV energy acceptance), resulting in maximum transmission of the secondary ions with minimum mass resolution. With high primary beam currents and a wide open energy window, intensities under specimen isolation conditions become similar to those obtained under CEF conditions [60-62,67,70] Thus, as reported by MacRae and Metson,[66] sensitivities in the range of <1 to 2 ppm are easily obtained using the method of specimen isolation. However, there are serious restrictions on the in situ analysis for many fine-grained materials, due to the large diameter of the primary beam.

To obtain steady-state charging at the sample surface under specimen isolation conditions an uncoated insulating

sample or a Teflon® insulated conducting sample must be used. The size of the charged aperture just above the sample surface is a primary factor in determining the amount of surface charge.[65] Geologic samples reach a potential of 450 to 600 V below the secondary accelerating voltage when covered by an aperture measuring 3 mm in diameter.[65,70] Thus, it is the resulting large kinetic energy barrier at the surface which gives rise to the extreme form of energy filtering. A more detailed account of the specimen isolation technique is given by Lau et al.[65]

4.3 Results and Discussion

The monazite specimen used in this study was analyzed by EPMA and INAA (see Table 4.2-1). Table 4.2-1 shows the range in concentration of the REE from a few tenths of a weight percent up to 15 to 20 wt. % Ce_2O_3 in the monazite. On the other hand, the analysis of the augite grain is reported in Table 4.2-2, and the concentration of the REE is only in trace amounts with Eu being in the sub-ppm range (0.21 ppm).

In the monazite analysis (Table 4.2-1), it is important to note that phosphorus and calcium were not analyzed by INAA and therefore the concentrations of P_2O_5 and CaO obtained using EPMA were incorporated into the INAA analysis. The INAA results have also been converted from ppm of the element into weight percent of the oxide for the purpose of comparison with the EPMA results. As well as the

totals being different, many discrepancies also occur between the analyses of each element. The difference in ThO_2 concentrations of 11.56 wt. % (EPMA) and 17.07 wt. % (INAA) is significant along with the difference in Ce_2O_3 concentrations of 23.91 wt. % (EPMA) and 16.75 wt. % (INAA), respectively. It is highly unlikely that these major differences are due to sample inhomogeneity (i.e. two different portions of the sample were sent to two different laboratories for analysis; Nuclear Activation Services and the Geological Survey of Canada) as may well be the case for many of the minor differences. Another EPMA analysis done at the Department of Geology at the University of Western Ontraio that is not reported here produced similar Ce_2O_3 and ThO_2 values to those obtained via the electron probe at the G.S.C. in Ottawa (those values reported here). It seems quite possible that improper resolution of spectral interferences in one or both of these techniques (EPMA and INAA) may be the cause of the discrepancy here. Since the lanthanum analyses seem to be relatively constant between the two techniques, lanthanum was chosen as an internal reference[28,32,45] for the SIMS analyses. The values reported in Tables 4.3-1 and 4.3-2 are also referenced to lanthanum for comparative reasons.

From the previous work on ionization yield factors in SIMS (chapter 3 and reference 77) we have seen that the relative ion yields[67,83,84] for the REE are similar. Using a glass standard (NBS standard reference material SRM 610 -

a glass with 61 elements at ~500 ppm) the relative ion yield for an element was obtained by correcting the SIMS intensity for the natural abundance of the isotope chosen for analysis and then normalizing to 100 % of the element. A more detailed description of relative ion yields was given in chapter 3. The relative ion yields for the REE have been normalized to lanthanum and are given in Table 4.3-1. The standard deviations on four measurements of the relative ion yield for each of the REE are <15 %. This, compared to a standard deviation of ~13 % (both specimen isolation and CEF techniques) for the entire group of REE, shows that the relative ion yields for the REE are indeed quite similar. Another point that emerges from Table 4.3-1 is that although the relative ion yields for each element are slightly different between specimen isolation and CEF modes, the relative ion yields when ratioed to La are constant and generally within experimental error when comparing the specimen isolation and CEF modes. These relative ion yields were then used in place of working curves for the analysis of REE.

Tables 4.3-2 and 4.3-3, and Figures 4.3-1 and 4.3-2 represent the correlation of results for the analysis of the REE using SIMS with those obtained by other techniques (CEF SIMS, EPMA and INAA), while Table 4.3-4 presents the specimen isolated SIMS results for the two samples for direct comparison with Tables 4.2-1 and 4.2-2. The SIMS data in Tables 4.3-2 through 4.3-4 have been corrected for

Table 4.3-1

Relative ion yields for the rare-earth elements referenced to La^+ measured in and NBS standard glass (SRM 610, a standard glass containing 61 elements at 500 ppm.)

Element	Specimen Isolation	-125 V Offset with ±10 eV energy acceptance (CEF conditions)
La	1.00	1.00
Ce	0.99	1.03
Pr	1.05	1.05
Nd	0.97	0.98
Sm	1.12	1.08
Eu	1.11	1.08
Gd	1.15	1.10
Tb	1.08	0.96
Dy	0.95	0.87
Ho	1.00	0.87
Er	0.90	0.87
Tm	0.86	0.83
Yb	0.83	0.80
Lu	0.67	0.67

The standard deviations on 4 measurements of the relative ion yield for each element are <15 %.

the natural abundance of the analyzed isotope and the ionization yield factor (obtained from the NBS standard glass SRM 610)[77] of each particular element. The corrected data were then referenced to lanthanum (g g^{-1}La) as they appear in the tables. It is also worth noting that the results from EPMA were recalculated from oxide wt. % before referencing to lanthanum (g g^{-1}La). Constraints on the maximum number of analyzed elements (or isotopes) in the SIMS and EPMA software is responsible for the lack of complete REE analysis in the EPMA and CEF SIMS analyses of the monazite sample and the specimen isolation SIMS analysis of the augite grain. For electron probe analysis, the REE were chosen to avoid overlap of lines within the X-ray spectrum. In the SIMS analyses, isotopes that were in reasonable natural abundance and had minimal potential molecular ion interferences were selected. These isotopes are given with each of the analyses (Tables 4.3-2 through 4.3-4). Here the elements chosen for analysis were sufficient to establish REE abundance patterns.[66] It was only for the purpose of presentation here and to show the lack of interferences on any element that a complete analysis of the monazite sample was carried out.

For the monazite sample (Table 4.3-2), the SIMS results for the majority of the REE were obtained using both forms of kinetic energy filtering. Comparison of the specimen isolation technique and the CEF mode, shows rather good agreement for the light REE (LREE) (lanthanum to

Table 4.3-2

REE analysis referenced to La (g g^{-1} La) for the monazite from New Mexico as performed by SIMS, EPMA and INAA.

Element	Specimen Isolation SIMS*	CEF SIMS**	INAA†	EPMA††
La (139)	1.00×10^{0}	1.00×10^{0}	1.00×10^{0}	1.00×10^{0}
Ce (140)	2.57×10^{0}	2.26×10^{0}	1.83×10^{0}	2.61×10^{0}
Pr (141)	3.48×10^{-1}	-	2.69×10^{-1}	3.91×10^{-1}
Nd (146)	1.46×10^{0}	1.22×10^{0}	1.04×10^{0}	1.26×10^{0}
Sm (152)	6.31×10^{-1}	5.00×10^{-1}	3.85×10^{-1}	5.03×10^{-1}
Eu (153)	2.66×10^{-2}	1.94×10^{-2}	1.79×10^{-2}	-
Gd (158)	4.17×10^{-1}	4.07×10^{-1}	4.36×10^{-1}	5.42×10^{-1}
Tb (159)	6.40×10^{-2}	-	1.03×10^{-1}	-
Dy (163)	2.69×10^{-1}	1.86×10^{-1}	2.56×10^{-1}	1.17×10^{-1}
Ho (165)	2.07×10^{-2}	-	1.79×10^{-2}	-
Er (166)	1.31×10^{-2}	4.05×10^{-2}	2.31×10^{-2}	1.43×10^{-2}
Tm (169)	3.45×10^{-3}	-	1.92×10^{-3}	-
Yb (174)	4.63×10^{-3}	2.47×10^{-2}	7.69×10^{-3}	1.91×10^{-2}
Lu (175)	1.11×10^{-3}	-	7.69×10^{-4}	-

The isotopes of each particular element that were selected for analysis are found in parentheses.

* In the SIMS analysis using specimen isolation conditons each mass unit was counted for 4 s and the masses were cycled through 5 times for each spot. The count rate range from $\geq1\times10^{6}$ counts in 4 s for $^{140}Ce^{+}$ down to ~500 counts in 4 s for $^{175}Lu^{+}$. The standard deviation of all these cycles in <2 to 3 % for each mass unit, thus when taking the ionization yields into account the standard deviations on the analyses are <15 % depending on the element.

** In the CEF SIMS analysis, each mass unit was counted for 5 s and the masses were cycled through 4 times for each spot. The count rates range from $\geq1\times10^{6}$ for $^{140}Ce^{+}$ down to $\geq3\times10^{3}$ counts in 5 s for $^{174}Yb^{+}$. The standard deviation for all of the cycles is <2 to 3 % for each mass unit, and again the standard deviations on the analyses will be <15 % depending on the element.

† Analysis by Neutron Activation Services, McMaster Nuclear Reactor, Hamilton, Ontario.

†† Analysis by G.S.C., Ottawa, Ontario.

dysprosium). However, when examining the heavy REE (HREE) (erbium and ytterbium) the presence of oxides of the LREE in the spectra obtained using CEF conditions is readily seen by the greater Er/La and Yb/La ratios than those found using any of the other techniques (see Table 4.3-2). Apart from this deviation at higher masses, a linear regression analysis of a plot of specimen isolation versus CEF results gave a correlation coefficient (R^2) of 0.99. However, without the use of specimen isolation conditions, it is still necessary to discriminate against the LREE oxides using either high mass resolution[73,74,95-97] or deconvolution of the mass spectra obtained using CEF conditions.[41,72] This makes the specimen isolation method of great value for the analysis of REE if crystals are of large enough dimensions.[60,61,66,70]

Also found in Table 4.3-2 are the results of the REE analysis by EPMA and INAA. This table also shows very good agreement between the three techniques (specimen isolation SIMS, INAA and EPMA). These results are also illustrated in Figure 4.3-1. Figure 4.3-1 shows the results obtained using EPMA (open circles) and INAA (closed circles) versus the results obtained by SIMS using specimen isolated conditions. Figure 4.3-1 also includes a line of slope equal to one, and thus the points in Figure 4.3-1 should fall close to the line if the different techniques are to be creditable.

The plot of INAA versus SIMS results using the specimen isolation technique for the monazite specimen

Figure 4.3-1

Plot of REE ratioed to La obtained by SIMS (specimen isolation conditions) vs. INAA (open circles) and EPMA (closed circles) for the monazite specimen (results shown in Table 4.3-2). The line of slope equal to 1 is where the data points should fall if the techniques are to give similar analyses. Taken from reference 68.

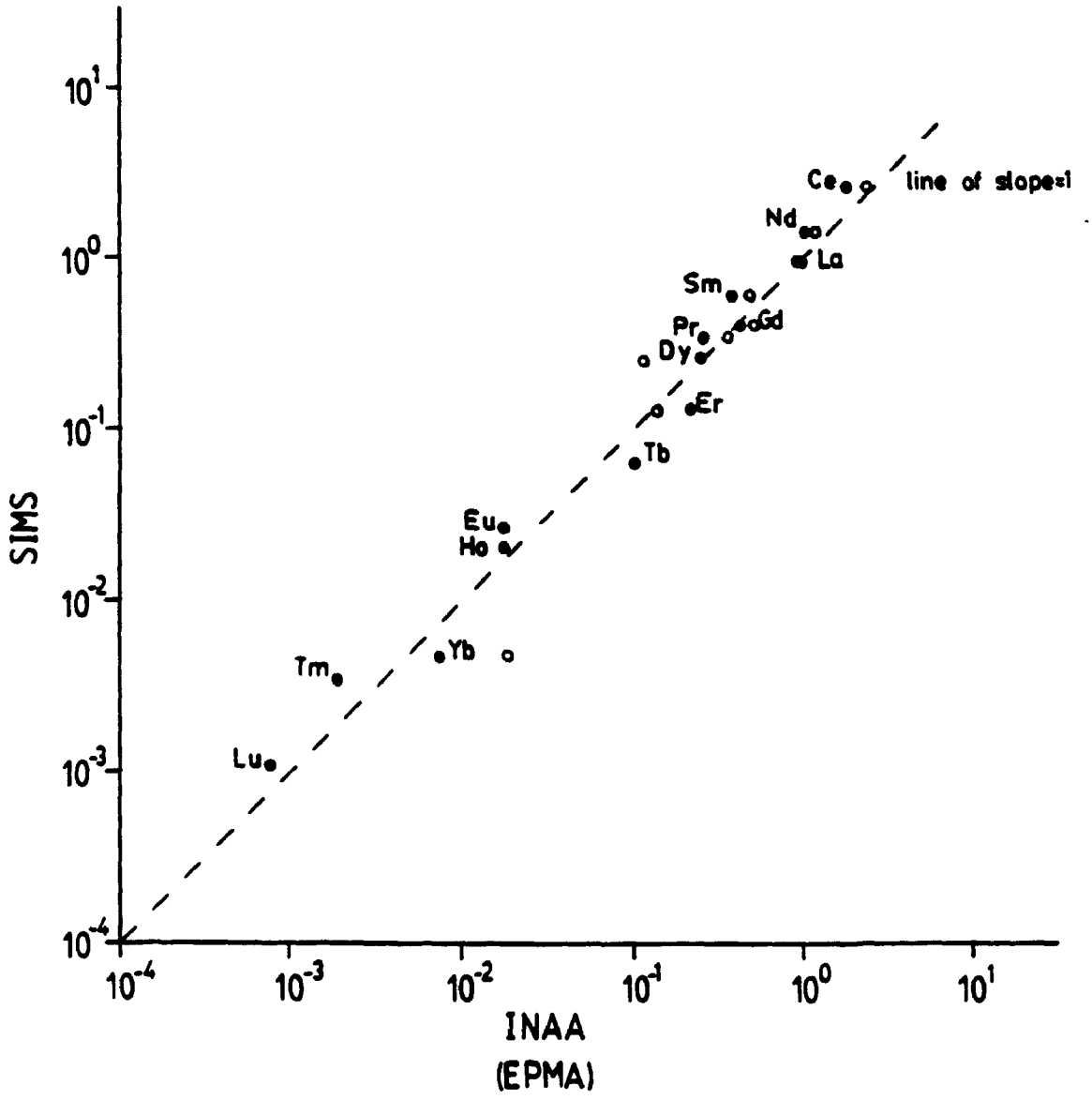
SIMS
INAA
(EPMA)
line of slope=1
Ce
Nd
La
Sm
Gd
Pr
Dy
Er
Tb
Eu
Ho
Yb
Tm
Lu
10^{1}
10^{0}
10^{-1}
10^{-2}
10^{-3}
10^{-4}

(Figure 4.3-1, closed circles) shows good correlation for the analyses obtained with the two techniques. A linear regression analysis gave a correlation coefficient (R^2) of 0.98. The most notable points that fall off the line are terbium, erbium and ytterium. These differences will be discussed along with the EPMA results. A plot of EPMA versus specimen isolated SIMS results for the same monazite specimen (Figure 4.3-1, open circles) again shows excellent agreement between the two techniques. The linear regression analysis also gave a correlation coefficient of 0.98. The only significant discrepancies here are those for dysprosium and ytterbium. To check the results from the INAA and EPMA techniques, a linear regression analysis was performed. The EPMA and INAA results gave a correlation coefficient of 0.97. The anomalous values here are for elements dysprosium, erbium and, again, ytterbium.

The agreement between the three techniques seems to support the credibility of each technique. Since ytterbium does not show any consistency among any of the techniques, a likely source of error may be inhomogeneity of the sample. For the analyses of the elements terbium, dysprosium and erbium, which are inconsistent only within one of the three techniques, the discrepancies are more likely to be due to improper resolution of the peaks and/or backgrounds in EPMA or INAA. However, sample inhomogeneity may also be a minor cause of these differences.

Further support for the reliability of the SIMS technique for REE analysis is presented in the analysis of an augite grain (Table 4.3-3 and Figure 4.3-2). Table 4.3-3 compares the SIMS (specimen isolation technique) results with those obtained from INAA. These results are also shown graphically in Figure 4.3-2. For this case, a linear regression analysis gave a correlation coefficient of 0.92. The lower R^2 may be reflected by the REE being present in only trace amounts such that the concentrations of europium and dysprosium (the two most significant anomalies) are approaching the detection limits of the techniques. The analysis of more of the REE may also help to show better correlation between the two techniques. The anomalous point of dysprosium in Figure 4.3-2 is not present in the monazite analysis (SIMS versus INAA in Table 4.3-2 and Figure 4.3-1) and thus, again it is possible that any minor differences may be attributed to inhomogeneity of the sample. The lower value of dysprosium in the SIMS analysis is a good indication that spectral interferences are not a problem when using the method of specimen isolation.

Consideration of both the augite and monazite results lends support to the use of SIMS for the analysis of REE. The two samples show the range of concentration in which SIMS may be applied. The REE concentrations in the augite sample (a few ppm) are well below the detection limits of the electron microprobe. Therefore, it appears that SIMS, being a focussed beam technique, is an excellent candidate

Table 4.3-3

REE analysis referenced to La (g g^{-1} La) for Augite A performed by SIMS (specimen isolation conditions) and INAA.

Element	SIMS*	INAA**
La (139)	1.0×10^{0}	1.0×10^{0}
Ce (140)	3.5×10^{0}	3.1×10^{0}
Nd (146)	4.1×10^{0}	3.8×10^{0}
Sm (152)	1.3×10^{0}	1.5×10^{0}
Eu (153)	8.7×10^{-2}	1.6×10^{-1}
Gd (158)	1.0×10^{0}	1.5×10^{0}
Dy (163)	4.8×10^{-1}	1.5×10^{0}
Er (166)	5.3×10^{-1}	-
Yb (174)	1.3×10^{0}	1.4×10^{0}

The isotopes of each particular element that were selected for analysis are found in parentheses.

* In the SIMS (specimen isolation) analysis each mass unit was counted for 40 s and the masses were cycled through 4 time. The count rates ranged from ~2×10^{6} counts in 40 s for $^{30}Si^{+}$ (3.09 % natural abundance) down to a few counts in 40 s for the REE depending on the natural abundance of the isotope analyzed. Taking into account the deviations of the counts from each cycle and those from the ionization yields, the standard deviation on the analyses is in the range of 15 to 20 %.

** Analysis by Neutron Activation Services, McMaster Nuclear Reactor, Hamilton, Ontario.

Figure 4.3-2

Plot of REE referenced to La obtained by SIMS (specimen isolation conditions) vs. INAA for the augite grain (results given in Table 4.3-2). Also included is a line of slope equal to 1 for comparison of the two techniques. Taken from reference 68.

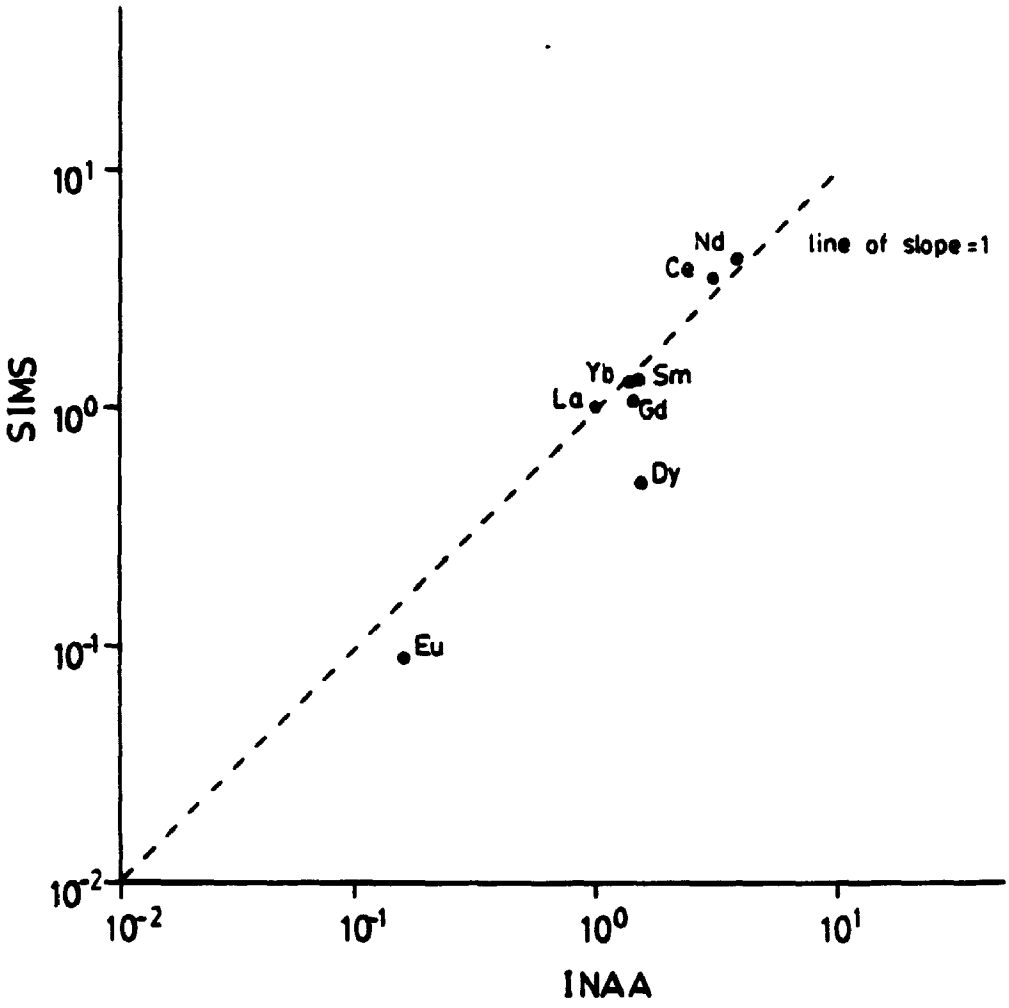
SIMS
INAA
10^{1}
10^{0}
10^{-1}
10^{-2}
10^{-2}
10^{-1}
10^{0}
10^{1}
Nd
Ce
Yb
Sm
La
Gd
Dy
Eu
line of slope = 1

Table 4.3-4

Analysis of the monazite and augite samples using SIMS with specimen isolation conditions.

Element	Monazite (wt. % oxide)*	Augite (ppm)
La (139)	9.16	1.3
Ce (140)	23.51	4.5
Pr (141)	3.18	-
Nd (146)	13.30	5.3
Sm (152)	5.71	1.7
Eu (153)	0.12	0.11
Gd (158)	3.75	1.4
Tb (159)	0.58	-
Dy (163)	2.41	0.62
Ho (165)	0.19	-
Er (166)	0.12	-
Tm (169)	0.03	-
Yb (174)	0.04	1.7
Lu (175)	0.01	-

The isotopes of each particular element that were selected for analysis are found in parentheses.

* The oxides of the trivalent REE are RE_2O_3 whereas Eu is the only divalent REE and its oxide is EuO.

for the analysis of REE. Whether one uses the method of specimen isolation,[66] or conventional energy filtering methods[41,72] will be determined by the size of the specimen since the minimum diameter of the primary beam with specimen isolation conditions is ~70 μm.[60-62] The technique of specimen isolation should be the method of choice for grains ≥100 μm because no corrections are required for any of the REE.

4.4 Conclusions

The results presented here show that accurate REE analysis in various mineral grains may easily be accomplished using SIMS. For the case of high REE concentraions (the monazite sample in this study), the SIMS results obtained through specimen isolation and CEF conditions are comparable to those obtained by either INAA or EPMA, but specimen isolation conditions give accurate values for all REE without corrections for molecular ion interferences. In the augite analysis, the SIMS results are again comparable with those from INAA. The trace amounts of REE in the augite specimen demonstrate the low detection limits available with SIMS. This in turn lends support to SIMS as a valuable technique for the analysis of REE in geologic (and many other) materials. The distinct advantage of using SIMS over INAA is the use of a focussed beam (≥70 μm for specimen isolation and 10 μm for CEF conditions) technique in SIMS compared with the bulk analysis performed

by INAA. The relatively short time needed and the ease of obtaining an analysis by SIMS are also significant advantages over other techniques such as INAA.

The major difference between specimen isolation[66] and CEF conditions[41,72] is the larger primary beam size generated by the specimen isolation method. However, when using CEF conditions an appreciable amount of LREE oxides are still present. These LREE oxides are easily removed through the use of specimen isolated conditions, but can also be removed by deconvolution of the spectra.[41,72] These results strongly suggest that SIMS done with the method of specimen isolation may be routinely used for accurate quantitative analysis of REE of all geologic samples of ≥100 μm; while the CEF SIMS technique should be used for smaller samples.

4.5 Summary of Chapters 1 Through 4

The SIMS technique and the features that make it a valuable instrument for use in many geochemistry studies was introduced in chapter 1. The problems associated with SIMS analysis such as matrix effects and molecular ion interferences were discussed. Kinetic energy filtering methods (conventional and specimen isolation) used to discriminate against molecular ions were introduced in chapter 1 and further discussed in chapters 2 and 3.

Chapter 2 dealt with the increased amount of molecular ion suppression available using the method of

specimen isolation versus conventional energy filtering methods. Similar ion intensities (relative to Si^+) obtained for glass, crystalline and ceramic samples when using some form of energy filtering should allow the use of glass standards in quantitative analysis of mineral specimens by SIMS. Also suggested in chapter 2 was the possible use of higher energy (≥80 eV) secondary ions in order to avoid the severe matrix effects found in the low energy region. A complete removal of matrix effects for the olivine solid solution studied using the specimen isolation method (~500 eV secondary ions) was not evident. However, it still remains that quantitative determinations using closely matching standards is the method of choice.

The application of some established ionization models to high energy secondary ions was presented in chapter 3. Relative ion yields obtained at 125 eV and ~500 eV were comparable with minor exceptions. Attempts to relate the high energy ion yields to established low energy ionization models was unsuccessful. Therefore, at the present, there exists no ionization model(s) for predicting the yield of high energy ions.

Chapter 4 was used to demonstrate the application of the specimen isolation method for the analysis of REE in various mineral grains. Examination of the relative ionization yields in chapter 3 shows that the yield factors for the REE are similar under a given set of energy filtering conditions. These ionization yields were then

used to produce the quantitative REE analyses given in this chapter.

Chapters 2 through 4 have dealt with the advantages and disadvantages of the specimen isolation technique for the SIMS analysis of minerals. The main disadvantages are the large primary beam diameter and the lack of suitable models for the ionization of high energy secondary ions. The main advantage of the specimen isolation technique is the increase in molecular ion suppression. The reduction of matrix effects for higher energy ions (CEF and specimen isolation) allows one to use calibration curves from glass or crystalline standards for quantitative determinations in geologic materials. The material to be presented in the next few chapters uses the method of specimen isolation in order to analyze the surfaces of non-conducting mineral specimens. Since no conductive metal films are necessary for SIMS analysis when using specimen isolated conditions, the depth profiling of leached feldspar surfaces is an excellent application of the SIMS technique.

REFERENCES

1. A. Benninghoven, F. G. Rüdenauer and H. W. Werner, "Secondary Ion Mass Spectrometry: Basic Concepts, Instrumental Aspects, Applications and Trends" (Wiley-Interscience, New York, 1987).
2. P. Williams, *Surf. Sci.*, 90, 588 (1979).
3. A. Havette and G. Slodzian, *J. Phys. Lett.*, 41, 247 (1980).
4. J. J. Thomson, *Philos. Mag.*, 20, 752 (1910).
5. K. S. Woodcock, *Phys. Rev.*, 38, 1696 (1931).
6. J. S. Thompson, *Phys. Rev.*, 38, 1389L (1931).
7. F. L. Arnot and J. C. Milligan, *Proc. Roy. Soc. A*, 156, 538 (1936).
8. F. L. Arnot, *Proc. Roy. Soc. A*, 158, 137 (1937).
9. R. F. K. Herzog and F. Viehöck, *Phys. Rev.*, 76, 855L (1949).
10. R. E. Honig, *J. Appl. Phys.*, 29, 549 (1958).
11. R. C. Bradley, *J. Appl. Phys.*, 30, 1 (1959).
12. H. E. Beske, *Z. Angew. Phys.*, 14, 30 (1962).
13. H. E. Beske, *Z Naturforsch.*, 19A, 1627 (1964).
14. H. W. Werner, *Phillips Tech. Rev.*, 27, 344 (1966).
15. H. W. Werner and H. A. M. de Grefte, *Vakuum-Technik*, 17, 37 (1968).
16. H. Liebl and R. F. K. Herzog, *J. Appl. Phys.*, 34, 2893 (1963).

17. C. A. Evans and J. P. Pemsler, *Anal. Chem.* 42, 1040 (1970).

18. C. W. Magee, W. L. Harrington and R. E. Honig, *Rev. Sci. Instr.*, 49, 477 (1978).

19. A. Benninghoven, *Phys. Status Solidi*, 34, K169 (1969).

20. A. Benninghoven and W. K. Sichtermann, *Org. Mass Spectrom.*, 12, 595 (1977).

21. R. Castaing and G. Slodzian, *J. Microsc.*, 1, 395 (1962).

22. J. M. Rouberol, J. Guernet, P. Deschamps, J. P. Dagnot and J. M. Guyon de la Berge, in "Proc. Fifth Int. Conf. on X-Ray Optics and Microanalysis" edited by G. Mollenstedt and K. M. Gaukler (Springer-Verlag, Berlin, 1968) p. 311.

23. J. M. Rouberol, M. Lepareur, B. Autier and J. M. Gourgout, in "Proc. Eighth Int. Congress X-Ray Optics and Microanalysis" edited by D. R. Beaman, R. E. Ogilvie and D. B. Wittry (Pendell Pub. Co., Midland, MI, 1980) p. 322.

24. H. Liebl, *J. Appl. Phys.*, 38, 5277 (1967).

25. V. E. Krohn and G. R. Ringo, *Appl. Phys. Letters*, 27, 479 (1975).

26. R. Levi-Setti, W. L. Wang and B. Crow, *J. de Phys.*, 45, C9-197 (1984).

27. H. Liebl, *Anal. Chem.*, 46, 22A (1974).

28. C. F. Robinson, in "Microprobe Analysis" edited by C. A. Anderson (Wiley-Interscience, New York, 1973) p. 507.

29. R. E. Honig, in "Secondary Ion Mass Spectrometry (SIMS V)" edited by A. Benninghoven, R. J. Colton, D. S. Simmons and H. W. Werner (Springer-Verlag, Berlin, 1985) p. 2.

30. J. F. Lovering, *Comm. Earth Sci.*, 3, 153 (1973).

31. J. F. Lovering, *Natl. Bur. Std. (U.S.) Spec. Publ.*, 427, 135 (1975).

32. N. Shimizu, M. P. Semet, C. J. Allegre, *Geochim. Cosmochim. Acta*, 42, 1321 (1978).

33. R. Castaing, H. Bizouard, R. Clocchiatti and A. Havette, *Bull. Mineral.*, 101, 245 (1978).

34. S. J. B. Reed, *Scanning*, 3, 119 (1980).

35. N. Shimizu and S. R. Hart, *Ann. Rev. Earth Planet. Sci.*, 10, 483 (1982).

36. S. J. B. Reed, in "Secondary Ion Mass Spectrometry (SIMS IV)" edited by A. Benninghoven, J. Okano, R. Shimizu and H. W. Werner (Springer-Verlag, Berlin, 1984) p. 451.

37. A. Havette, *J. de Phys.*, 45, C2-797 (1984).

38. A. Havette, *Scanning Electron Microsc.*, 1985/II, 585 (1985).

39. J. B. Metson, G. M. Bancroft and H. W. Nesbitt, *Scanning Electron Microsc.*, 1985/II, 595 (1985).

40. J. T. Armstrong, J. C. Huneke and G. J. Wasserburg, in "Microbeam Analysis" edited by K. F. J. Heinrich (Wiley, New York, 1982) p. 202.

41. G. Crozaz and E. Zinner, *Earth Planet. Sci. Lett.*, 73, 41 (1985).

42. C. A. Andersen, H. J. Roden and C. F. Robinson, *J. Appl. Phys.*, 40, 3419 (1969).

43. D. G. W. Smith and J. C. Rucklidge, *Adv. Geophys.*, 16, 57 (1973).

44. C. A. Andersen, *Int. J. Mass Spectrom. Ion Phys.*, 2, 61 (1969).

45. C. A. Andersen, *Int. J. Mass Spectrom. Ion Phys.*, 3, 413 (1970).

46. M. L. Yu and W. Reuter, *J. Appl. Phys.*, 52, 1478 (1981).

47. M. L. Yu and W. Reuter, *J. Appl. Phys.*, 52, 1489 (1981).

48. N. Shimizu, in "Secondary Ion Mass Spectrometry (SIMS V)" edited by A. Benninghoven, R. J. Colton, D. S. Simmons and H. W. Werner (Springer-Verlag, Berlin, 1985) p. 45.

49. G. Slodzian, in "Secondary Ion Mass Spectroscopy (SIMS III)" edited by A. Benninghoven, J. Giber, J. Laszlo, M. Riedel and H. W. Werner (Springer-Verlag, Berlin, 1982) p. 115.

50. N. Shimizu and S. R. Hart, *J. Appl. Phys.*, 53, 1303 (1982).

51. H. E. Beske, Z. *Naturforsch.*, 22A, 459 (1967).

52. J. R. Hinthorne and C. A. Andersen, *Am. Mineral.*, 60, 143 (1975).

53. L. A. Streit, R. L. Hervig, and P. Williams, in "Microbeam Analysis" edited by A. D. Romig Jr. and W. F. Chambers (San Francisco Press, 1986) p. 91.

54. S. L. Chryssoulis, W. J. Chauvin and L. J. Surges, *Can. Met. Quart.*, 25, 223 (1986).

55. S. L. Chryssoulis, L. J. Cabri and R. S. Salter, in "Proceedings of the International Symposium on Gold Metallurgy" edited by R. S. Salter, D. M. Wyslouzil and G. W. McDonald (Pergamon Press, New York, 1987) p. 235.

56. C. A. Andersen and J. R. Hinthorne, *Anal. Chem.*, 45, 1421 (1973).

57. C. A. Andersen and J. R. Hinthorne, *Science*, 175, 853 (1972).

58. M. Lepareur, *Rev. Technol. Thompson-CSF*, 12, 225 (1980).

59. S. J. B. Reed, in "La Microsonda Ionica Nells Scienze Della Terra" (Società Italiana di Mineralogia e Petrologia, Pavia, 1988) p. 20.

60. J. B. Metson, G. M. Bancroft, N. S. McIntyre and W. J. Chauvin, *Surf. Interface Anal.*, 5, 181 (1983).

61. J. B. Metson, G. M. Bancroft, H. W. Nesbitt and R. G. Jonasson, *Nature (London)*, 307, 347 (1984).

62. N. S. McIntyre, W. J. Chauvin, J. B. Metson and G. M. Bancroft, *J. de Phys.*, 45, C2-132 (1984).

63. J. B. Metson, G. M. Bancroft, N. S. McIntyre and W. J. Chauvin, in "Secondary Ion Mass Spectrometry (SIMS IV)" edited by A. Benninghoven, J. Okano, R. Shimizu and H. W. Werner (Springer-Verlag, Berlin, 1984) p. 466.

64. N. S. McIntyre, D. Fichter, J. B. Metson, W. H. Robinson and W. J. Chauvin, *Surf. Interface Anal.*, 7, 69 (1985).

65. W. M. Lau, N. S. McIntyre, J. B. Metson, D. Cochrane and J. D. Brown, *Surf. Interface Anal.*, 7, 275 (1985).

66. N. D. MacRae and J. B. Metson, *Chem. Geol.*, 53, 325 (1985).

67. H. W. Nesbitt, J. B. Metson and G. M. Bancroft, *Chem. Geol.*, 55, 139 (1986).

68. I. J. Muir, G. M. Bancroft, N. D. MacRae and J. B. Metson, *Chem. Geol.*, 64, 269 (1987).

69. N. D. MacRae, *Amer. Mineral.*, 72, 1263 (1987).

70. I. J. Muir, G. M. Bancroft and J. B. Metson, *Int. J. Mass Spectrom. Ion Processes*, 75, 159 (1987).

71. G. Ray and S. R. Hart, *Int. J. Mass Spectrom. Ion Phys.*, 44, 231 (1982).

72. E. Zinner and G. Crozaz, *Int. J. Mass Spectrom. Ion Processes*, 69, 17 (1986).

73. S. J. B. Reed, *Int. J. Mass Spectrom. Ion Processes*, 54, 31 (1983).

74. S. J. B. Reed, *Scanning Electron Microsc.*, 1984/II, 529 (1984).

75. I. M. Steele, R. L. Hervig, I. D. Hutcheon and J. V. Smith, *Amer. Mineral.*, 66, 526 (1981).

76. N. Shimizu, *Earth Planet. Sci. Lett.*, 39, 398 (1978).

77. J. B. Metson, D. L. Tui, I. J. Muir and G. M. Bancroft, *Scanning Microsc.*, 2, 663 (1988).

78. K. Wittmaack, *Nucl. Inst. and Methods in Phys. Res.*, 168, 343 (1980).

79. G. Slodzian, *Surf. Sci.*, 48, 161 (1975).

80. G. Blaise and G. Slodzian, *Surf. Sci.*, 40, 708 (1973).

81. N. Shimizu, *Int. J. Mass Spectrom. Ion Proc.*, 69, 325 (1986).

82. G. Slodzian, J. C. Lorin and A. Havette, *J. Physique*, 23, 555 (1980).

83. H. A. Storms, K. F. Brown and J. D. Stein, *Anal. Chem.*, 49, 2023 (1977).

84. A. R. E. Lodding, H. Odelius and L. G. Petersson, in "Secondary Ion Mass Spectrometry (SIMS IV)" edited by A. Benninghoven, J. Okano, R. Shimizu and H. W. Werner (Springer-Verlag, Berlin, 1984) p. 478.

85. H. Odelius, A. R. E. Lodding, L. O. Werme and D. E. Clark, *Scanning Electron Microsc.* 1985/II, 927 (1985).

86. A. E. Morgan and H. W. Werner, *Anal. Chem.*, 49, 927 (1977).

87. M. J. Vasile, *Nucl. Inst. and Methods in Phys. Res.*, 218, 319 (1983).

88. R. Shimizu, T. Ishitani and Y. Ueshima, *Jap. J. App. Phys.*, 13, 249 (1974).

89. L. A. Haskin, M. A. Haskin, M. A. Frey, and T. R. Wildeman, in "Relative and absolute terrestrial abundances of the rare earths" edited by L. H. Ahrens (Pergamon, New York, 1968) p. 889.

90. J. D. MacArthur, A. J. Anderson, X. P. Ma, G. R. Palmer, and P. Cerny, in "11th International Congress on X-ray Optics and Micro-analysis" edited by J. D. Brown and R. H. Packwood (Univ. of Western Ontario Graphic Services, London, 1987) p. 175.

91. A. L. Hanson, B. M. Gordon and K. W. Jones, *EOS (Trans. Am. Geophys. Union)*, 66, 401 (1985) (abstract).

92. M. L. Rivers, I. M. Steele and J. V. Smith, *EOS (Trans. Am. Geophys. Union)*, 66, 401 (1985) (abstract).

93. J. V. Smith, M. L. Rivers, S. R. Sutton, K. W. Jones, A. L. Hanson, and B. M. Gordon, in "11th International Congress on X-ray Optics and Microanalysis" edited by J. D. Brown and R. H. Packwood (Univ. of Western Ontario Graphic Services, London, 1987) p. 163.

94. A. C. Thompson, J. H. Underwood, Y. Wu, R. D. Giauque, K. W. Jones and M. L. Rivers, *Nucl. Inst. and Methods in Phys. Res. A*, 266, 318 (1988).

95. S. J. B. Reed, in "16th Annual Meeting of the Microbeam Analysis Society" edited by R. H. Geiss (San Francisco Press, San Francisco, 1981) p. 87.

96. S. J. B. Reed, *Chem. Geol.*, 48, 137 (1985).

97. S. J. B. Reed, D. G. W. Smith and J. V. P. Long, *Nature (London)*, 306, 172 (1983).

PART II

CHAPTER 5

INTRODUCTION TO MINERAL WEATHERING

5.1 Introduction

The chemical breakdown of rocks and minerals is an important process by which elements are fractionated at the earth's surface. Thus, it follows that the weathering of rocks and minerals is an integral part of the geochemical cycles of many elements. On a large scale, weathering processes operate at the interface of the earth's endogenic and exogenic cycles, whereas on a microscale, the weathering reactions occur at the interface between solids and solutions. Because of these interfacial reactions, weathering is a complex phenomenon, and therefore any factor influencing the earth's surface may well influence the weathering process.[1]

Studies in weathering are important in such areas as soil science and the buffering of acid precipitation. During weathering, mineral transformations form soil minerals and release nutrient (as well as detrimental) elements to the surrounding soils. Some minerals may weather to form clays or dissolved salts as a result of acid-base neutralization reactions between the dissolved acids and the solid base (minerals). Many natural acids are

present in soils, however, there has been great concern recently over the presence of anthropogenic acids in many natural environments. Rock materials differ substantially in their ability to buffer acidity and therefore the sensitivity to acid precipitation varies over the many different environments. Other topics that relate to weathering studies are the adsorption of anthropogenic metals and organic compounds on clay minerals, the storage of radionuclide wastes, and the capacity of soils to store water and therefore act as a buffer to flash floods.[1] Many characteristics of fossil-fuel reservoir rocks such as sediment composition and porosity and permeability all depend on weathering reactions.[1]

The bulk of the early research on weathering was based upon the chemistry and mineralogy of vertical profiles. One of the major concepts from the early work was the "mineral-stability series in weathering" of Goldich.[2] This weathering series was based upon observations of which minerals weather more rapidly than others. The arrangement of the primary rock forming minerals in the weathering series coincides with Bowen's reaction series.[2] Goldich[2] indicated that results from early experiments of attack by water on silicate frameworks were consistent with his mineral-stability series. Attempts using thermodynamics[3,4] or silicate bond strengths[5] have been unable to produce a theoretical explanation of Goldich's weathering series. Thermodynamic models[3] use data for reactants and products

under standard states, a situation which does not always exists in nature.[1] Problems with using silicate bond strengths, include the prediction of similar stabilities for micas, whereas in nature, biotite and muscovite weather at different rates.[1] The difficulty in explaining the weathering series is an indication of the complex nature of the interactions between the dissolving mineral and the reactant solutions.

Weathering sequences based upon the occurrence of secondary minerals have also been proposed. In this case, the relative amounts of primary and clay minerals in a given environment may be used to determine the degree to which weathering has progressed. An abundance of primary minerals is generally assumed to be indicative of less weathered environments, whereas increasing amounts of clay minerals (smectite and kaolinite) and gibbsite are usually indicative of environments where more extensive weathering has taken place. Similar to the weathering series of Goldich,[2] this type of sequence is again based upon observations of the mineralogy in the weathering profiles.[1] The least amount of weathering is generally found at the bottom of the profiles (where there is an abundance of primary minerals), whereas progression to greater stages of weathering is seen at the top of the weathering profiles (generally an abundance of clay or gibbsite minerals).

It is important to realize that these weathering sequences are merely observations, and that weathering reactions do not necessarily proceed along these pathways.[1] A number of publications have focussed on the inaccuracies that may be developed with these types of weathering sequences. Many authors[6-14] have shown that feldspar minerals (a primary mineral) may form kaolinite and even gibbsite directly.[1] In some cases the direct formation of gibbsite from primary minerals and a subsequent resilication to kaolinite has been observed.[14] It has since been suggested that clay minerals are "environmental" products rather than "end" products of weathering. In other words, weathering is a result of both the environment and duration of weathering rather than just the duration of weathering. Present day studies in weathering have moved towards the importance of understanding the geochemical conditions for breakdown of primary minerals and formation of secondary minerals.[1] Much of the recent work on weathering has dealt with the reactions at mineral surfaces in aqueous solutions.

5.2 Weathering of Silicate Minerals

Silicate minerals break down relatively rapidly during weathering. However, until the past few decades, little was known about their behavior in the weathering process.[15] Laboratory dissolution of silicate minerals may be separated into two distinct processes. The initial stage

is a rapid exchange of alkali ions from the silicate surface with hydrogen ions from solution.[16,17] This is followed by the release of elements from the silicate lattice to solution, a much slower process.[17,18] Early dissolution experiments were carried out by measuring the solution concentration of elements from the feldspar as a function of time. From these experiments, the feldpsar minerals were observed to dissolve incongruently (i.e. the net composition of the solution does not correspond to that of the dissolving species[17,19]), and the reactions exhibited parabolic reaction kinetics. Various dissolution models have been used to explain the incongruent nature of silicate dissolution. These can be grouped into four competing theories. These theories are: (1) the crystalline precipitate hypothesis;[18,20] (2) the amorphous precipitate hypothesis;[21] (3) the leached layer hypothesis;[22-25] and (4) the surface reaction hypothesis.[19,26-29]

The crystalline precipitate[18,20] and amorphous precipitate[21] hypotheses are somewhat similar. In each case a solid phase (crystalline or amorphous) precipitates at the silicate/solution interface and hence acts to control the rate of dissolution. The dissolution rate is controlled by the diffusion of the silicate components through this protective (precipitated) layer. The amorphous precipitate hypothesis proposes an amorphous silica-alumina precipitate, whereas a single-phase or polycrystalline precipitate forms

the protective layer in the crystalline precipitate hypothesis. The leached layer hypothesis,[22-25] requires the formation of some type of leached layer at the silicate surface. Alkali ions from the silicate are exchanged for hydrogen or hydronium ions not only at the silicate surface, but also within the silicate lattice. This exchange results in the formation of a leached layer. The rate of dissolution is then controlled by the rate of diffusion of cations through the residual layer. The leached layer is said to be unstable and is composed of mainly silica and alumina. In the surface reaction hypothesis,[19,26-29] no protective, diffusion limiting layers are proposed. However, a very thin, porous leached zone up to a few monolayers thick may exist between the unaltered silicate and solution. What sets the surface reaction hypothesis apart from the others is that the rate of dissolution is controlled by a reaction(s) at the silicate surface rather than diffusion of cations through a protective layer.

The parabolic reaction kinetics observed in laboratory studies of silicate weathering may be explained using any of the four models of dissolution. In the surface reaction hypothesis, the observation of parabolic kinetics may be a result of the rapid dissolution of fine particles adhering to the silicate surface from the sample preparation stages. For the other three models where a protective layer is present, the parabolic kinetics of the silicate may be

explained using Fick's first law of diffusion. Fick's first law of diffusion

$$J = -D\,(dc/dx)$$

predicts that the flux of the dissolved product (J) may be related to the product of the concentration gradient across the protective surface layer (dc/dx) and the diffusion coefficient (D). As the thickness of the protective layer increases (mechanism dependent upon the model chosen) this will cause a decrease in the diffusion gradient and hence a decrease in the flux of material from the unaltered silicate to the solution. Models for the transport of material from feldspar to solution have been proposed by Wollast[18] and Helgeson.[20,30] Each of their models correlate quite well with the experimental results they obtained.

5.3 Surface Analysis of Weathered Silicate Materials

5.3.1 Introduction

The four theories predict somewhat different compositions at the surface and near surface of the silicate mineral. Detailed surface morphological studies would be valuable for testing these hypotheses. The use of surface analysis cannot tell whether or not the dissolution rate is controlled by diffusion through a protective layer since diffusion will also be dependent on the porosity of the protective layer.[19] However, a precipitated layer (amorphous or crystalline) would certainly be detectable based upon its proposed composition. For the two hypotheses

where no precipitate layer forms, the surface reaction hypothesis predicts very little difference between the surface and bulk material, whereas the leached layer hypothesis would only have concentrations of silica and alumina similar to those of the unaltered silicate.[19] Scanning electron microscopy (SEM)[29,31,32] and X-ray photoelectron spectroscopy (XPS)[19,33,34] have been used to characterize the surfaces of many weathered silicates. Although the majority of the early surface work was done using SEM and XPS, Auger electron spectroscopy (AES)[35-37] and secondary ion mass spectrometry (SIMS)[38-42] have also been used in recent studies in silicate weathering.

5.3.2 X-ray Photoelectron Spectroscopy

The features of XPS that make it particularly useful for the study of mineral surfaces are the use of binding energy data of the photoemitted electrons to determine the chemical nature of the mineral surface, the ability to detect most elements (with the exception of hydrogen), and its extreme surface sensitivity. The binding energy or ionization potential of the electrons is obtained by measuring the kinetic energy of the electrons ejected as a result of the interaction between a photon and the molecule. The Einstein formula:

$$h\nu = B.E. + K.E.$$

applies here, where $h\nu$ is the incident photon energy (known value), K.E. is the measured kinetic energy of the

electrons, and B.E. is the binding energy (difference between the free electron and the orbital energy of the electron) of the electrons.

In an XPS experiment, the x-ray beam penetrates well into the bulk of the sample. However, the effective sampling depth is determined by the escape depth of the photoemitted electron. The electron escape depth is dependent upon such factors as the incident x-ray energy, and the crystal structure and density of the sample. Effective sampling depths on the order of 5 to 50 Å are found for most samples,[43,44] therefore making XPS a technique for surface analysis.[45] With an uncharged x-ray beam coming into the sample and negatively charged electrons leaving the sample, charging problems with non-conducting specimens may cause the ejected electrons to return to the sample. To minimize (almost eliminate) sample charging, a conducting wire grid or mesh covers the sample surface and/or the surface is flooded with low energy electrons.

In the past, the application of XPS to geochemical studies has been used to investigate mineral surface compositions (versus bulk phase analysis), mineral surface dissolution mechanisms, quantitative analysis of adsorbed metal species, the oxidation state of iron in clays, and the bonding of metal ions adsorbed on clay minerals.[45] For a review of XPS and its application to mineral dissolution studies, the reader is directed to Petrovic et al.[19]

5.3.3 Scanning Electron Microscopy (SEM)

SEM has also been widely used for investigations into the weathering of silicate minerals. After sample preparation and prior to dissolution experiments, SEM has been used to determine the nature of the surface before dissolution. SEM is an excellent technique for detecting the presence of fine particles and/or other significant artifacts which are believed to be a major factor contributing to the incongruent dissolution of silicate minerals. SEM analysis after the dissolution experiments has shown the formation and growth of lens-shaped etch pits.[29,46]

5.3.4 Auger Electron Spectroscopy (AES)

Some of the more recent surface work on weathering of silicate minerals has been done using AES. In an AES experiment, the sample is exposed to an electron beam and core electrons (from the atoms in the sample) are removed. The vacancy created by the departure of a core level electron may then be filled by an electron from an outer shell. The energy given off by this transition is enough to emit an electron from an outershell. This is the Auger electron and its energy is characteristic of the element that it originates from. Like photoelectron spectroscopy, the escape depth of the Auger electrons is on the order of a few tens of angstroms, and hence AES is a technique with excellent surface sensitivity. Hochella et al.[36] quote the

surface sensitivity to be on the order of a few tens of angstroms. Other features that make AES attractive to mineral dissolution studies are the excellent lateral resolution (<1 μm), good detection of light elements (except hydrogen) and the ability to produce semiquantitative surface analysis. Sample damage by the electron beam and the surface charging of insulating samples have hampered AES applications to geochemistry in the past. However, by reducing the electron beam voltage (to ~3 keV) and using low beam currents (nanoamps) many of these problems are reduced if not eliminated.

Perry et al.[35] have used AES to investigate the surfaces of feldspar grains prepared for dissolution experiments. Reacted feldspar surfaces have been analyzed using AES by Hochella et al.,[37] and most recently depth profiles by AES have been reported for naturally weathered hornblende grains by Mogk and Locke.[47] For a description of AES applied to mineralogical studies the reader is referred to a publication by Hochella et al.[36]

5.3.5 Secondary Ion Mass Spectrometry (SIMS)

A complete mass range analysis, along with good lateral resolution and low detection limits make SIMS an ideal tool for mineralogical studies. In part I of this thesis, these features and other desirable and not so desirable features of SIMS were discussed. The feature that makes SIMS particularily valuable for analysis of weathered

minerals is the depth profiling ability of the technique. As the primary ion beam impinges on the sample, material is sputtered away and a newly exposed surface is continually formed. The use of the specimen isolation technique described in chapter 1 makes the depth profiles obtained using SIMS somewhat more easily interpreted since no conductive surface coatings are necessary. It is felt that any type of conductive surface coating may have significant effects on the yield of secondary ions as well as the surface charging of the sample. SIMS was first applied to the analysis of altered silicate surfaces by Beusen and Gijbels.[38] Other more recent studies[39-42] have shown the usefulness of SIMS for both surface analysis and depth profiling to characterize the nature and depth of altered layers on weathered silicate surfaces. Further description of the SIMS technique was presented in part I of this thesis. For a description of specimen isolated SIMS applied to the characterization of altered plagioclase surfaces, the reader is directed to a publication by Muir et al.[42] and the final two chapters.

5.4 Review of Past Silicate Dissolution Studies

5.4.1 Methods

Many of the past investigations into the laboratory dissolution of silicate minerals have generally involved similar methods of sample preparation. Silicate grains for dissolution were generally hand selected to avoid

contaminants, crushed, and the size fractions separated by dry sieving.[32-34] Different research groups have employed various size fractions. An investigation into the dissolution rate dependence on the surface area (by size fraction) was recently presented in two publications by Holdren and Speyer.[48,49] A thermodynamic consideration of the effects of particle size relating to dissolution is given by Talman and Nesbitt.[50] Ultrasonic cleaning in acetone, in some cases followed by rinsing with distilled water, was done to remove any remaining fine particles from the silicate surfaces. Some authors (for example see references 32 and 34 and the references within) used a pretreatment with an aqueous mixture of HF and H_2SO_4 to further ensure that no fine particles or surface artifacts were present on samples prior to the dissolution experiments. Using AES, Perry et al.[35] were able to show chemical alteration of K-feldspar surfaces due to this HF/H_2SO_4 pretreatment procedure. However, with the correct ratio of HF to H_2SO_4, no surface alteration is observed (G.R. Holdren Jr., personal communication).

Dissolution experiments have been carried out using solutions of a wide range of pH values. Some experiments were done in batch type reactors where the reactant solution (pH buffered) was not altered throughout the course of the experiment. After dissolution, the sample grains were collected by filtration and analyzed using SEM or XPS. The remaining solutions were analyzed for cations (derived from

the mineral) using methods found in Strickland and Parsons.[52] Recently the use of a "fluidized bed" or continuous flow reactor has been described in the literature.[51] In this case, the solution is continually exchanged with an incoming solution. The continuous flow reactor benefits from the constant set of conditions that are present in the reaction chamber.[51] With a continuous mixing of the solid (fine particles) and solution, there should exist no strong concentration gradients such as those found in the packed column experiments of Correns and von Engelhardt.[22] Another plus of a flow cell type reactor is the lack of secondary precipitates onto the primary mineral surfaces since concentration levels well below saturation for any precipitation reactions are easily maintained. As in the experiments with batch type reactors, the reactant solution is also collected and analyzed for components of the starting material.

The surface analysis of leached silicates has been generally monitored using SEM and XPS. However, AES and SIMS studies have also been recently reported. Surface analysis on both naturally and synthetically weathered silicate minerals has been performed.

5.4.2 Discussion of Past Results

Most experiments report the dissolving of significant amounts of silicate material. In some instances, several hundred angstroms of the surface material was removed.

Analysis of the reactant solutions as a function of time shows incongruent dissolution of the starting material. Holdren and Berner[33] observed that the dissolution kinetics change from parabolic to linear with the passage of time. While linear dissolution kinetics has been used to show the release of cations from the silicate framework, the initial presence of parabolic kinetics has lead to a great deal of controversy over the mechanism of rate control in the dissolution of silicate minerals. In cases where a protective layer is predicted to form, the parabolic reaction kinetics are seen as being due to the formation of a protective layer (as described earlier), while linear kinetics are viewed to be a result of the diffusion of material through the newly formed protective layer.[18,20] In the surface reaction hypothesis, linear kinetics are the result of congruent dissolution at the surface of the fresh, unaltered material. Attempts to rationalize the initial observation of parabolic kinetics have not been too sucessful. The rapid dissolution of fine particles at the surface may be one source of parabolic reaction kinetics. However, after the removal of these fine particles in the sample preparation stages (HF/H_2SO_4 treatment), the experiments still show the initial presence of parabolic reaction kinetics. The presence of a thin "disturbed" layer on the surface[34,53] has also been used to explain the parabolic reaction kinetics. This "disturbed" layer may be

the result of adsorption of CO_2 from the atmosphere onto the sample surface.[34,53]

SEM has been used extensively to study the surface morphology of laboratory and naturally weathered silicate grains.[29,31,46,56] In most naturally weathered samples it was necessary to remove the clay material (weathering products) by sonification to observe the mineral surfaces. In all cases, the most dominant surface features were etch pits (see Figure 5.4-1) that form during the dissolution reactions. These etch pits are believed to form at sites of excess energy resulting from surface defects (for example, dislocations).[54] A complete description of these etch pits and the kinetics of their formation may be found in a publication by Brantley et al.[57] When comparing the naturally weathered silicate grains to those etched in the laboratory, no significant differences were observed (i.e. etch pits formed in both cases). Any minor differences have been attributed to differences in the rate of etching and/or the nature of the etchant in the various experiments.[54]

Since these etch pits are not uniformly distributed over the entire sample surface it would follow that dissolution is not continuous over the entire surface. This lead Berner and Schott[54] (as well as Berner and many other co-workers[15,19,29,32-34,46]) to conclude that rate-control involving a protective layer would not be possible.

The degree of pitting may be used to compare minerals on a relative scale of weathering. For similar minerals,

Figure 5.4-1

SEM photomicrograph of naturally weathered oligoclase showing the presence of etch pits. The oligoclase specimen is from the Plastic Lake Catchment, Ontario.

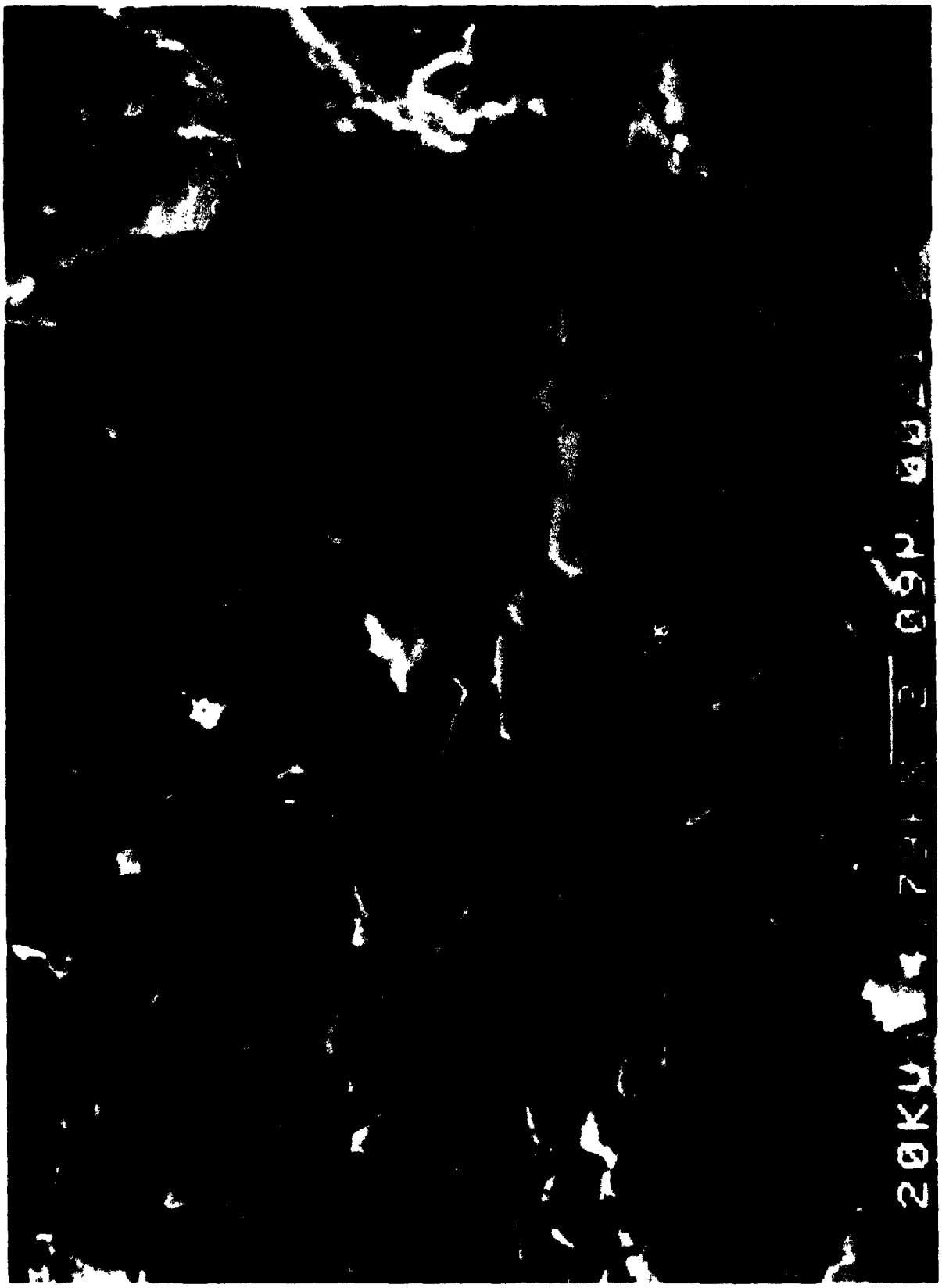
20KV
0.5μ

more pitting would be indicative of more extreme weathering conditions. For different minerals, the extent of pitting may be used to comment on which minerals break down more readily than others under similar conditions. Long term exposure of the silicate grains, and thus further growth of these etch pits may result in the grains becoming rather fragile. These fragile grains would then be more susceptible to breakdown during the physical stages of weathering (i.e. erosion and transport).

Fine grains enriched in aluminum have also been observed on some silicate surfaces.[56] These particles are believed to result from the dissolution process and were also reported to occur at sites of excess energy.[56] However, since these particles are also non-uniformly distributed over the silicate surface it was thought that they would not contribute to the rate-control of dissolution.[56]

To decide which of the hypotheses regarding silicate dissolution is most correct, the analysis of the surface and near surface compositions of the reacted grains should provide the evidence needed. Petrovic et al.[19] report very little difference in XPS spectra for reacted and unreacted (control) feldspar grains. Similar results were also reported for naturally weathered pyroxene and hornblende grains.[54] Although each study found similar compositions for the surface of reacted and unreacted materials, each study also acknowledged a small degree of alteration in the

surface composition. This surface alteration was a depletion in the alkali and alkaline earth elements relative to silicon.[15,54] These XPS results do not suggest in any way the formation of a thick, highly altered, tightly adhering protective layer, but rather suggests the presence of a very thin slightly altered surface layer.[33,54]

Using XPS intensity ratios and mean free paths of the electrons (see reference 19 for the method of calculation), Petrovic et al.[19] calculated the depth of this altered layer to be ~17 Å. Petrovic et al.[19] were able to discount the two hypotheses involving precipitates based upon the surface compositions from XPS and that the thickness of the altered layer (~17 Å) was less than the unit cell dimensions of clay minerals. It should be noted that these results do not rule out the possibility of any fine particles precipitating onto the silicate surfaces during dissolution. Since several hundred angstroms of the starting material are dissolved and the altered layer is only ~17 Å thick, Petrovic et al.[19] concluded that the formation of a leached layer was unlikely, and in turn sided with the surface reaction hypothesis.

Using data obtained using a continuous flow reactor, recent studies[51,55,58] have shown that the surface reaction hypothesis may not apply. Similar to the past work of Correns (and Correns and von Engelhardt),[22-25] Chou and Wollast[51,55] predict that a layer of as much as several tens of angstroms may form on the surface of albite. Surface

analysis using AES by Hochella et al.[37] has shown a significant difference in the composition of the surface versus bulk regions for hydrothermally altered labradorite. Depth profiling studies on natural and laboratory dissolved silicate grains using AES[47] and SIMS[41,42] have shown the presence of surface layers up to several hundred angstroms in thickness. However, better characterization of the nature of this layer and the conditions under which it forms are necessary in order to conclude if the rate of dissolution is controlled by some type of protective layer.

5.4.3 Summary

A few years ago the incongruent nature by which silicate materials break down during dissolution was essentially believed to occur by a surface reaction mechanism. SEM and XPS experiments yielded no evidence for the formation of a highly altered, tightly adhering, diffusion inhibiting protective layer. Recent reports by Chou and Wollast[51,55] have lead to a resurgence in the belief that some type of altered layer forms and hence acts to control the rate of dissolution. This has resulted in a controversy[59,60] over whether or not an altered surface layer operates at the fresh feldspar/solution interface.

Surface studies using AES[37,47] and SIMS[41,42] have reported evidence that some type of surface layer does exist for both laboratory and naturally dissolved silicate materials. Although these results show evidence for the

formation of an altered layer, they in no way determine the role of this layer in the dissolution process. However, when taking into account the results of Chou and Wollast,[51,55] it is likely that this altered zone acts as a protective, dissolution inhibiting layer for the minerals chosen under the conditions chosen for study.

5.5 Future Studies

The controversy over the existence of an altered surface layer that controls the rate of silicate dissolution[59,60] has not been put to rest. The use of surface analytical techniques is obvious and the need for more information regarding the nature of this possible surface layer is necessary. Petit et al.[61] describe the application of an analytical technique based upon a resonant nuclear reaction (RNR) for the depth profiling of hydrogen to studies in silicate weathering. This technique should allow one to monitor the uptake of hydrogen ions during the dissolution process. However, one serious drawback of this technique is that hydrogen in the form of water, hydronium, or hydroxyl ions is not differentiated.

The XPS results of Petrovic et al.[19] for alkali feldspars are different from those presented by Muir et al. (see reference 42 and the following chapter) for plagioclase feldspars under slightly more acidic reaction conditions. Therefore, it is important to consider the laboratory

conditions under which the minerals were reacted, as well as the mineral studied.

The final two chapters present surface and sub-surface analytical data (obtained with SIMS) regarding the dissolution of plagioclase grains in the laboratory (chapter 6) and in nature (chapter 7). These SIMS results are further validated by SEM and XPS results.

CHAPTER 6

CHARACTERISTICS OF ALTERED PLAGIOCLASE SURFACES BY SIMS AND XPS

6.1 Introduction

Four competing theories have been proposed to explain the initial stages of feldspar dissolution. These are: (1) the crystalline precipitate hypothesis;[18,20] (2) the amorphous precipitate hypothesis;[21] (3) the leached layer hypothesis;[22-25] and (4) the surface reaction hypothesis.[19,26-29] The first two postulate that a solid phase precipitates at the interface between the feldspar and solution and acts as a "protective" layer in controlling the dissolution rate. The third requires a leached layer to be formed at the feldspar surface. The fourth hypothesis postulates that feldspar dissolution is a surface reaction, with a porous, very thin leached zone, a few monolayers thick separating the feldspar from the reactant solution. As distinct from the other hypotheses, the surface reaction hypothesis proposes that the reaction at the feldspar surface is rate controlling rather than controlled by diffusion. A more detailed account of these four theories is found in the previous chapter and the references within.

Through SEM studies[29,31,32] coupled with the surface data obtained from XPS[19,33,34] the surface reaction hypothesis was viewed five years ago as the most appropriate of these theories. In order to test these various hypotheses, detailed surface morphological studies were conducted. These results, however, must be placed in the context of other surface studies, and these are briefly reviewed in the remainder of the introduction.

Recent work by Chou and Wollast[51,55] and Holdren and Speyer[58] has shown that the surface reaction hypothesis may not apply. Instead, they predict that a layer several tens of angstroms thick forms at the feldspar surface. Similarly to Correns and von Engelhardt[22] and Correns,[23-25] Chou and Wollast[51,55] propose that the dissolution of feldspars (albite in their study) occurs in three stages. The initial stage deals with the formation of a hydrogen feldspar from the exchange of alkali ions by hydrogen ions, followed by the formation of a layer depleted in sodium and enriched in silicon and/or aluminum. The final process is the slow dissolution of the residual layer at the solid/solution interface accompanied by diffusion of ions from the fresh feldspar boundary leading to a quasi-steady-state dissolution stage.[55]

In order to test these various hypotheses and possibly resolve the controversy[59,60] there is a need for appropriate surface morphological and particularly surface analytical studies of leached solids. Already mentioned are

the SEM[29,31,32] and XPS[19,33,34] studies which have given support to the surface reaction hypothesis. Some recent studies show that scanning Auger microscopy (SAM or AES) and secondary ion mass spectrometry (SIMS) are also very useful for surface analysis of minerals. For example, Hochella et al.[37] have used SAM and XPS to investigate the composition of reacted labradorite surfaces. They report that the surface of hydrothermally altered (300°C and 300 bars) labradorite (finely powdered) differs substantially from that of the unreacted portions, and that there is a leached layer of at least 20 to 30 Å. Recent dissolution studies of titanite[39,40] and feldspars[41,42] demonstrate the usefulness of SIMS for both surface analysis and depth profiling to further characterize the nature and depth of surface layers from tens to thousands of angstroms thick. Hochella et al.[37] draw attention to the need to depth profile reacted mineral surfaces; but Nesbitt and Muir's[41] study is one of the first to depth profile feldspars with any of the XPS, SAM or SIMS techniques. They showed that altered layers from 300 to 800 Å thick had formed on the surface of the naturally weathered oligoclase grains. Such depth profiling studies require macroscopic samples (≥ 4 × 4 mm) rather than fine particles. The layers observed by Nesbitt and Muir[41] were depleted in silicon and hence residually enriched in aluminum. These layers varied in thickness from crystal to crystal in the same rock and

also showed depletion of sodium and calcium in the SIMS profiles (Nesbitt and Muir, unpublished data).

This chapter (and to some extent another publication[42]) deals with the use of SIMS depth profiles along with XPS data for determining the presence of a substantial leached layer depleted in sodium, calcium and aluminum (residually enriched in silicon) for plagioclase samples reacted in water (pH 5.7) and aqueous HCl (pH 3.5) at or near standard temperatures and pressures. A brief explanation for the differences in surface composition between the naturally weathered oligoclase[41] and the plagioclase samples from laboratory dissolution studies is addressed in the following chapter.

6.2 Experimental

6.2.1 Sample Preparation

With the exception of the labradorite sample (supplied by J. Forth, Department of Geology, U.W.O.) the remaining plagioclase samples used in this study were donated by F.J. Wicks of the Royal Ontario Museum. Table 6.2-1 lists the sample localities for each sample studied. Electron probe analyses of these samples are given in Table 6.2-2. For each specimen, randomly oriented sections were cut into small pieces measuring approximately 1 × 2 × 0.5 cm in size and then polished. Sample preparation involved grinding with ultra-fine silicon carbide paper followed by subsequent stages of mechanical

Table 6.2-1

Locality of the plagioclase samples used in the dissolution studies.

Specimen	Locality
Albite	Bathurst Tp., Lanark Co., Ontario.
Oligoclase	North Lepis Luzuli Occurrence on Soper River, Baffin Island.
Andesine	Risor, Norway.
Labradorite	locality unknown
Bytownite	Carton Co., New Mexico

Table 6.2-2

Composition of the plagioclase samples used in the dissolution studies. Determinations were made by electron probe analysis.*

Specimen	Albite	Oligoclase	Andesine	Labradorite	Bytownite
Na_2O	10.04	9.62	10.01	4.98	4.22
Al_2O_3	21.22	21.42	21.30	28.82	30.14
SiO_2	66.70	66.11	64.77	54.57	52.86
K_2O	0.28	0.28	0.44	0.40	0.28
CaO	2.10	2.61	2.32	10.92	12.60
BaO	0.04	0.05	0.03	-	-
Total	100.38	100.13	98.87	99.69	100.10

* Wt. % oxides.

polishing using 6, 1, and 1/ 4 μm diamond pastes. The specimen surfaces were cleaned by boiling in spectral grade acetone, then methanol, followed by ultrasonic cleaning in spectral grade methanol.

6.2.2 Dissolution Experiments

The reactant solutions (either water at pH 5.7 or aqueous HCl, pH 3.5) were prepared from doubly distilled deionized water (conductivity $\sim 10^{-6}\ \Omega^{-1}\ cm^{-1}$). These solutions were stored in 1 L HDPE (high density polyethylene) bottles on a shelf above the sample chambers. The sample chamber, a 100 mL Teflon® jar is connected to the solution storage bottle (input) by a Teflon® tube (5 mm diameter) attached to the bottom of the jar. The sample is suspended in the chamber on a Teflon® mesh to ensure even flow of solution around the sample. The solution exits the top of the sample chamber via an "outlet" tube (Teflon®; 5 mm diameter) where it flows into a collection (output) bottle (1 L HDPE). J. Price (Department of Chemistry, U.W.O.) developed this aparatus. Mixing of the reactant solution was achieved by having the input at the bottom and the output at the top of the sample chamber. This should not permit the existence of any significant concentration gradients in the reaction chamber. The flow rate through the chamber is maintained by a stopcock on the "outlet" tube and was adjusted such that the volume of the reaction chamber was exchanged approximately three times every 24

hours (i.e. 300 mL/24 hrs). This flow rate should be sufficient to keep the concentrations of dissolved species well below saturation. Before each experiment, each apparatus was cleaned with a ~1 M HCl solution, followed by rinsing with deionized doubly distilled water until the pH readings of the outflow solutions were equal to that of the solution entering the apparatus.

Five samples of each specimen were prepared and studied. One sample of each specimen was allowed to react with water (pH 5.7) for 60 days, while another was subjected to identical conditions for a period of 90 days. Two other samples were reacted in aqueous solutions of HCl at a pH of 3.5 for periods of 60 and 90 days. A final sample was saved for a control and was left in a desiccator for the duration of the leaching experiments. In cases where a final sample was not available, an earlier reacted sample was repolished to give a fresh feldspar surface and then used as a control material.

6.2.3 Surface Analysis

The depth profiling capability of the SIMS technique was used to characterize the near-surface composition of the dissolved plagioclase samples. The application of SIMS to geologic problems has been well documented throughout the literature,[62-65] as well as in chapters 1 through 4 of this thesis.

A CAMECA IMS 3f secondary ion microscope was used for these experiments. The method of specimen isolation[66,67] was used in order to clear the spectra of molecular ion interferences. Virtually complete extinction of molecular ions from the mass spectra is one advantage of the specimen isolation technique.[68] However, most important to this study is that the specimen isolation technique requires no conductive surface coating for the analysis of the non-conducting plagioclase samples, hence no surface contamination has been introduced.

A primary ion beam of mass filtered $^{16}O^-$ ions at a net 15 to 16 kV and approximately 100 nA was rastered over a 250 × 250 μm area. Positive secondary ions were detected. To reduce crater edge effects, secondary ions were sampled from an area having a diameter slightly greater than 60 μm (well within the crater) through the placement of an aperture at the entrance to the spectrometer. This area (~60 μm diameter) will be large enough to obscure any local compositional variations.

Correlation of depth of penetration by the primary beam with analysis time was achieved by determining the sputtering rate from freshly polished samples. A highly polished (1/4 μm) labradorite surface was exposed to the primary beam under the given analysis conditions for 45 minutes. The depth of the crater formed as a result of sputtering was then measured using a Sloan Dektak® profilometer. The sputtering rate was found to be on the

order of 2 Å per second per 100 nA of primary beam current. These measurments were repeated using a polished (1/4 μm) albite surface and a cleaved oligoclase face. The sputter rate for albite was ~1.4 Å per second per 100 nA of primary beam current, while the oligoclase was sputtered at a rate of ~1 Å per second per 100 nA of primary beam current. Minor problems with the sputter rate determinations were experienced. Surface irregularities on the albite and labradorite samples were not completely removed by polishing, and some cleavage steps were present on the oligoclase sample. Rough bottoms of the sputter craters resulting from the use of specimen isolation conditions also made the determinations difficult. These problems make the time-depth correlation approximate only. Also, the sputtering rates of the reacted samples may be slightly different, possibly due to small changes in the topography of the surface (i.e. etch pits, and fine particles), or the different chemical composition of the near-surface region. However, it is felt that these differences will not completely account for the depth or presence of the altered layer which is observed. Despite these problems, the quoted depths are accurate to within a factor of two.

To reinforce the SIMS results, studies using X-ray photoelectron spectroscopy (XPS or ESCA, electron spectroscopy for chemical analysis) and scanning electron microscopy (SEM) were also conducted. A Surface Science Laboratories SSX100 ESCA spectrometer was used to obtain the

XPS spectra. An incident photon beam of Al Kα (1486eV) X-rays was used. The area of analysis was elliptical in shape with the minor axis having a diameter of 1000 μm. Again, the analysis spot size is large enough to reduce any effects due to local variations of composition. SEM analysis was performed using an ISI-DS130 secondary electron microscope.

6.3 Results

6.3.1 pH Measurements

pH measurements were taken each day for the input solution and once every fifth day for each exit solution. A Cole Parmer model 5983 pH meter was used. The purpose of these measurements was to ensure that the pH of the input solutions was constant and to see if any change in the pH as a result of mineral dissolution could be detected. In the dissolution experiments with aqueous HCl, the pH readings for the input and output solutions were constant at a pH of 3.5. These pH readings did not vary by any more than ±0.1 pH units. The pH readings for the experiments involving doubly distilled deionized water had much larger deviations. The average of the readings (both input and output soulutions) was 5.7 pH units. The calculated standard deviations for these pH readings ranged between 0.5 and 0.7 pH units. These large deviations may be attributed to the difficulty in measuring the pH of a very dilute solution such that minor fluctuations may have a significant

effect, and/or the low quality of the pH meter electrode used. The pH data obtained for all experiments are inconclusive regarding the uptake of hydrogen ions in the dissolution process.

6.3.2 SEM Results

SEM photomicrographs of the reacted samples show the presence of features resulting from dissolution (for example, see Figure 6.3-1). Observed features such as etch pits and the progression of dissolution reaction(s) (smoothing and rounding) along fractures, cracks and cleavage traces have been shown by many other authors.[29,31,32] These features were not present on the unreacted (control) samples. However, some pits (irregular in shape) were present on the surface of some control samples, and presumably are left over from the polishing process. For the samples undergoing dissolution these pits may then serve as points for attack by the leachant as seen by some degree of smoothing and/or rounding.

The SEM photomicrographs (Figure 6.3-1) contained no evidence for the growth or formation of new phases relating to the dissolution process. However, some type of "organic deposits" were observed on some of the reacted samples (see Figure 6.3-2). Comparison of EDX (energy dispersive x-ray analysis) spectra from a clean area of the feldspar surface and these "organic deposits" show similar ratios for the constituent elements of feldspar minerals (sodium, aluminum,

Figure 6.3-1

a) SEM photomicrograph of albite after 60 days dissolution in water (pH 5.7). Note the etching.

b) SEM photomicrograph of oligoclase after 60 days dissolution in aqueous HCl (pH 3.5). Note the etching and progression of reaction along cleavage traces.

a

b

Figure 6.3-2

a) SEM photomicrograph of albite after 60 days dissolution in aqueous HCl (pH 3.5) showing the presence of some type of "organic deposits." An etch pit is also shown.

b) SEM photomicrograph of andesine after 60 days dissolution in water (pH 3.5) showing the presence of some type of "organic deposits." An etch pit is also shown.

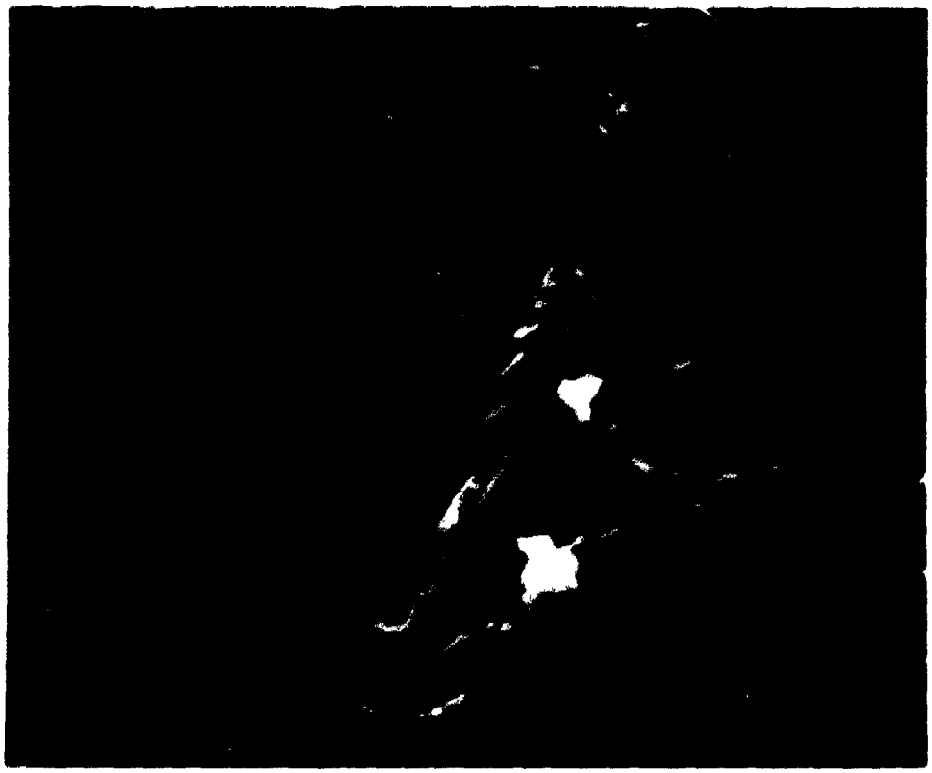

a

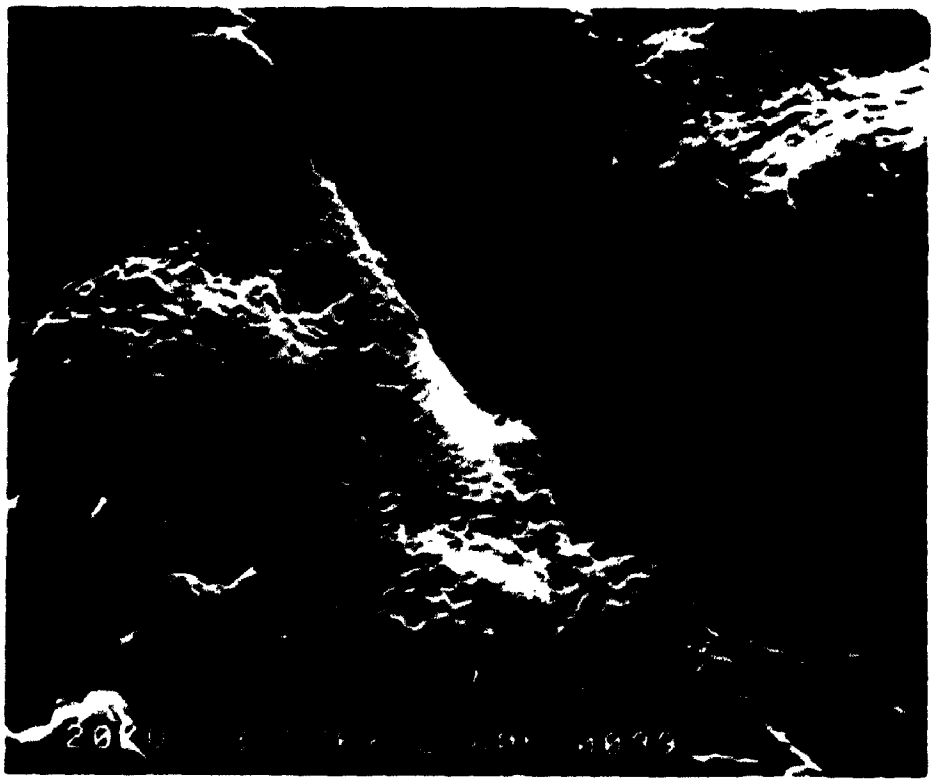

b

silicon and calcium). However, the peak intensities are significantly lower in the spectra from the "organic deposits." Similar results to these are expected for a thin organic film covering a feldspar surface since this would decrease the peak intensities from the elements in the feldspar and not show any intensity for carbon, hydrogen, oxygen and nitrogen since these low energy x-rays are hidden under the x-ray continuum. The source of these "organic deposits" is not known. However, it is suspected that they may be derived from the polymer material of the aparatus. These deposits cover a very small percent of the surface area, and will not affect the dissolution process.

6.3.3 SIMS Results

Normalization of Data

A sample profile of the raw SIMS data is presented in Figure 6.3-3. The results from the SIMS profiles have been normalized and are presented in Figures 6.3-4 through 6.3-14. During SIMS analysis, four spots on each sample (reacted and unreacted) were analyzed. The SIMS data presented in Figures 6.3-4 to 6.3-14 are not quantitative. After normalization of the SIMS data, the profiles merely show the percent change in the secondary ion intensity of each of the measured isotopes.[41]

The initial step of the normalization procedure involves referencing the counts (observed secondary ion intensity) from the isotope of interest (^{23}Na, ^{27}Al, and

Figure 6.3-3

SIMS depth profile of a labradorite sample leached in a solution of aqueous HCl (pH 3.5) for a period of 90 days. The observed secondary ion intensity (counts) are plotted against time of analysis for the following isotopes; ^{23}Na, ^{27}Al, ^{28}Si, and ^{40}Ca.

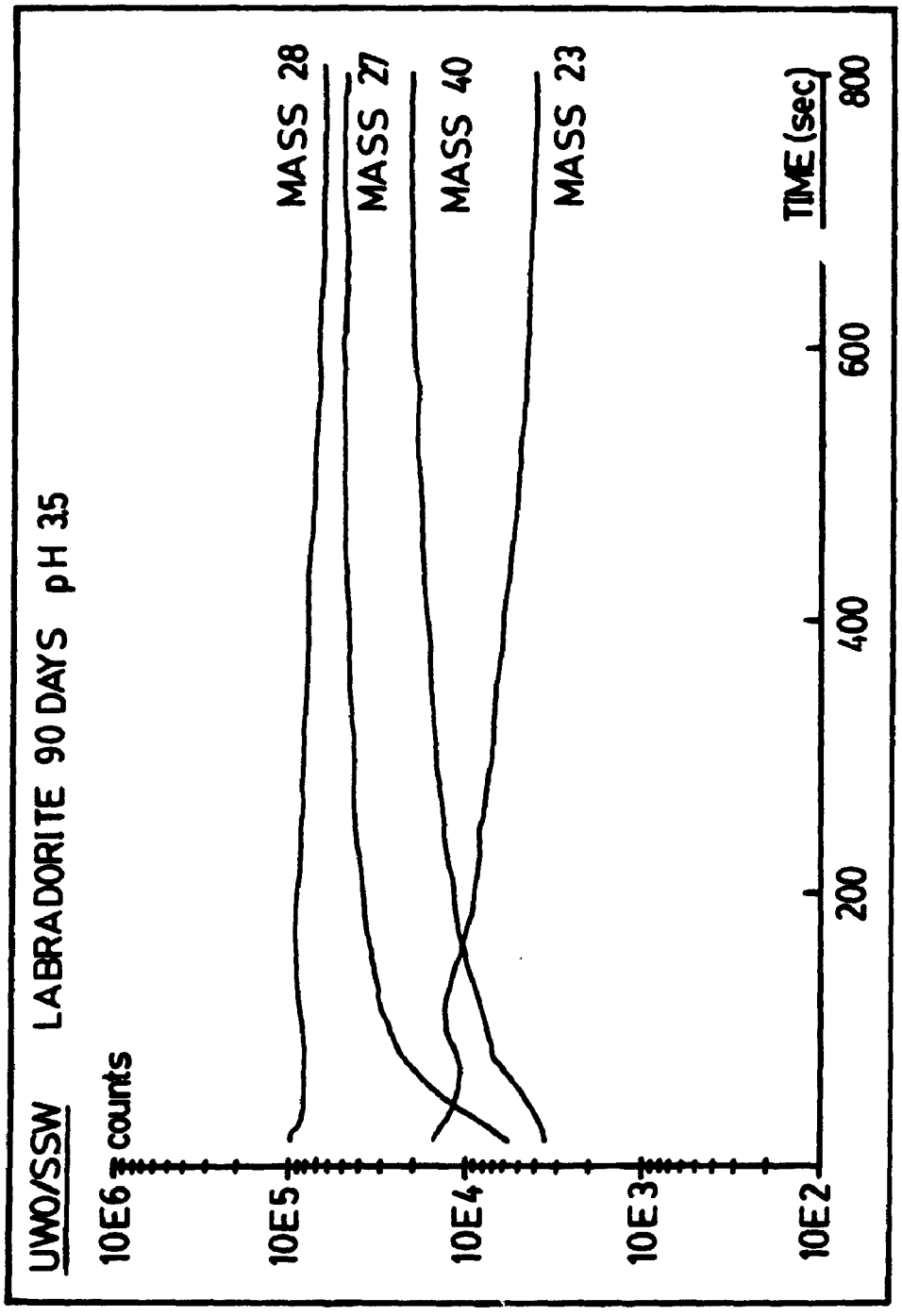
UWO/SSW LABRADORITE 90 DAYS pH 3.5
10E6 counts
10E5
10E4
10E3
10E2
MASS 28
MASS 27
MASS 40
MASS 23
200
400
600
800
TIME (sec)

^{40}Ca) to that for ^{28}Si. Here, ^{28}Si is used as an internal reference, and by referencing to ^{28}Si any variation in sputtering yields during the analyses are minimized. ^{28}Si was chosen as the internal reference because the ^{28}Si signal (secondary ion intensity) is constant throughout each profile. For the second step, the data from each point (cycle) of the profile are normalized to the average of the later cycles (last few hundred seconds) in the profile. The data from the deepest part of the profiles are assumed to represent the original (bulk) composition of the plagioclase samples.[41] Thus, it is now possible to calculate the difference in secondary ion intensity resulting from the dissolution process. The final step is a repeat of the previous step for the control specimen which was analyzed during the same session in order to keep the operating parameters of the SIMS instrument constant. This step is used in an attempt to reduce any effect(s) on the secondary ion signals due to the surface and/or surface charging. The average of the data from the control samples is then subtracted from the reacted sample (at each cycle or point in the analysis) to give the difference in observed secondary ion intensity due to the formation of a leached layer(s) during dissolution. This difference is expressed

as a percent. This normalization procedure may also be given by the following equation:

$$\left[\frac{(^{23}Na/^{28}Si)_{surface}}{(^{23}Na/^{28}Si)_{bulk} \times \left[\frac{(^{23}Na/^{28}Si)_{surface}}{(^{23}Na/^{28}Si)_{bulk}}\right]_{control}} - 1\right] \times 100$$

Where ^{23}Na is replaced with ^{27}Al and ^{40}Ca for each analysis spot (four in total) of the reacted feldspar. The correction factor from the control specimen is obtained from the average of all four analyzed spots. This normalization may also be found in references 41 and 42.

Figure 6.3-4 is presented to show the reproducibility of the SIMS technique in specimen isolated conditions. The percent change in the secondary ion intensity for ^{23}Na, ^{27}Al, and ^{40}Ca relative to ^{28}Si is plotted on the ordinate whereas the time of sputtering (depth) in the profile is plotted on the abscissa. These profiles were taken of a labradorite sample that had been leached in an aqueous solution of HCl (pH 3.5) for 90 days. All four spots show similar profiles. Two of the four spots have been randomly selected to illustrate this point. These two profiles are shown in Figure 6.3-4. Also apparent from Figure 6.3-4, are the unusual results for sodium. It is suggested that these irregualar profiles may be the result of charge induced migration of sodium during the SIMS experiments. This phenomenon has been observed by other authors[69,70] and was also commented on in part I of this thesis.

Figure 6.3-4

SIMS depth profiles for $^{23}Na/^{28}Si$, $^{27}Al/Si^{28}$, and $^{40}Ca/^{28}Si$ after normalization (see text) from two points of analysis (labradorite leached under acidic (pH 3.5) conditions for a period of 90 days) have been plotted in order to show the reproducibility of the SIMS technique (specimen isolation conditions). The percentage change in secondary ion intensity between the reacted and unreacted labradorite (ordinate) is plotted against the time (seconds) of sputtering in the profile (abscissa).

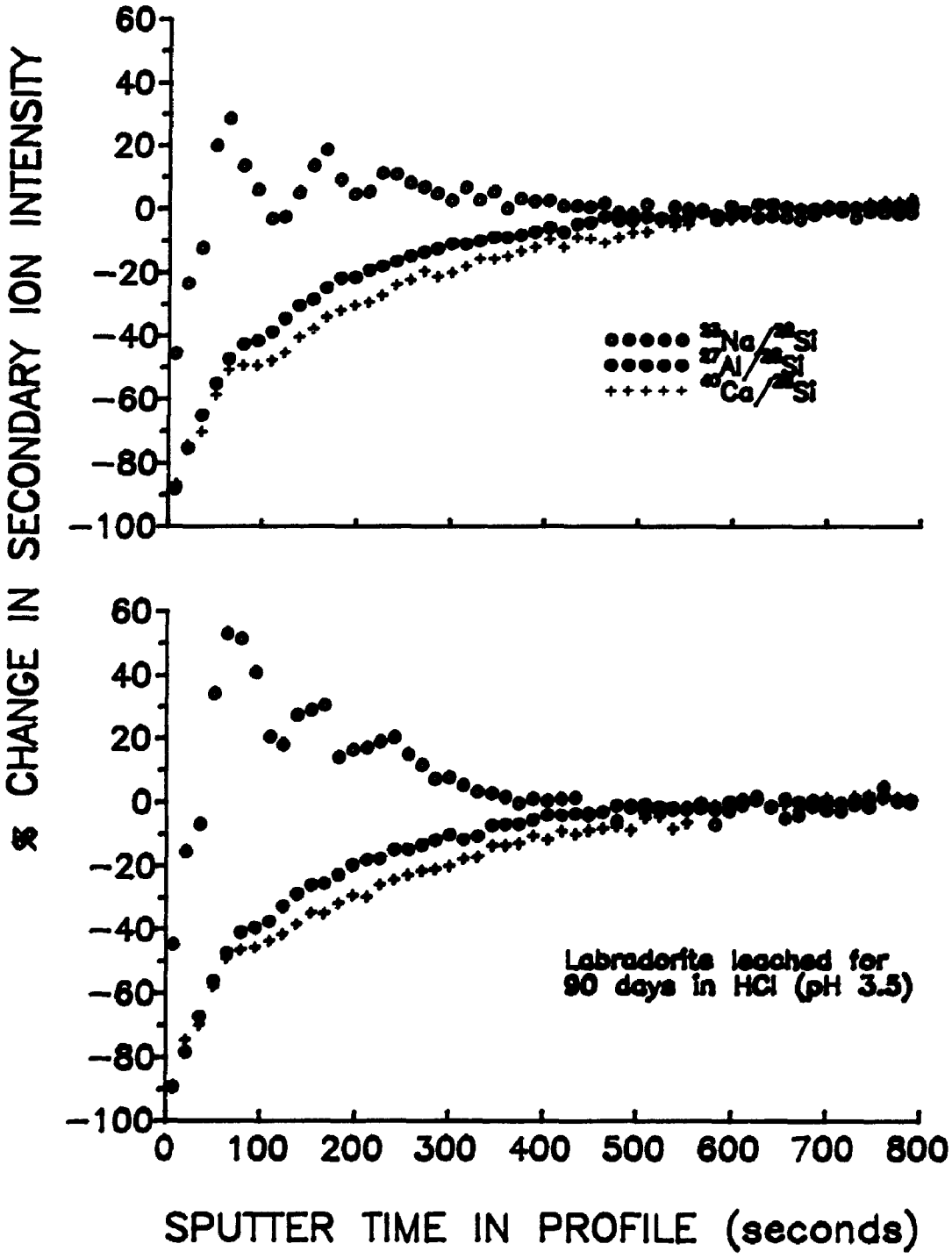
% CHANGE IN SECONDARY ION INTENSITY
60
40
20
0
−20
−40
−60
−80
−100
$^{23}Na/^{28}Si$
$^{27}Al/^{28}Si$
$^{40}Ca/^{28}Si$
Labradorite leached for 90 days in HCl (pH 3.5)
0
100
200
300
400
500
600
700
800
SPUTTER TIME IN PROFILE (seconds)

Dissolution of Plagioclase in Aqueous HCl (pH 3.5)

Figures 6.3-5 through 6.3-9 represent sample profiles obtained for each plagioclase specimen which has undergone dissolution for 90 days in an aqueous solution of HCl (pH 3.5). While four complete analyses for each mineral were conducted, only a sample profile of each is presented. Similar profiles were observed for the experiments lasting 60 days and hence are not reported here. In all five figures, data for the elements of the leached sample have been plotted as closed circles, and the data for the unleached (control) samples have been plotted as open circles. The normalization procedure for the control sample is identical to that for the reacted samples described above.

The SIMS results indicate that a layer depleted in sodium, calcium and aluminum has formed as a result of the reactions between aqueous HCl (pH 3.5) and the plagioclase surfaces (see Figures 6.3-5 to 6.3-9). The presence of this layer agrees quite well with the predictions made by Correns and von Engelhardt,[22] Correns[23-25] and Chou and Wollast.[51,55] The depth of alteration is taken from the surface (beginning of the profile) to the depth where the secondary ion signals of the reacted and non-reacted specimens become somewhat similar. For the bytownite specimen (the most calcium rich), this translates to a zone leached of sodium, aluminum and calcium that is somewhere between 800 and 1600 Å thick (see Figure 6.3-5) (sputter

Figure 6.3-5

SIMS depth profiles showing the percent difference in secondary ion intensity between one spot of analysis for both of the unreacted and reacted samples and the average of four points of analysis from the unreacted sample. $^{23}Na/^{28}Si$, $^{27}Al/^{28}Si$, and $^{40}Ca/^{28}Si$ are all shown separately. The closed circles represent bytownite leached in aqueous HCl (pH 3.5) for a period of 90 days, and the open circles represent the unreacted bytownite sample. The percentage change in secondary ion intensity (ordinate) is plotted against time (seconds) of sputtering in the profile (abscissa).

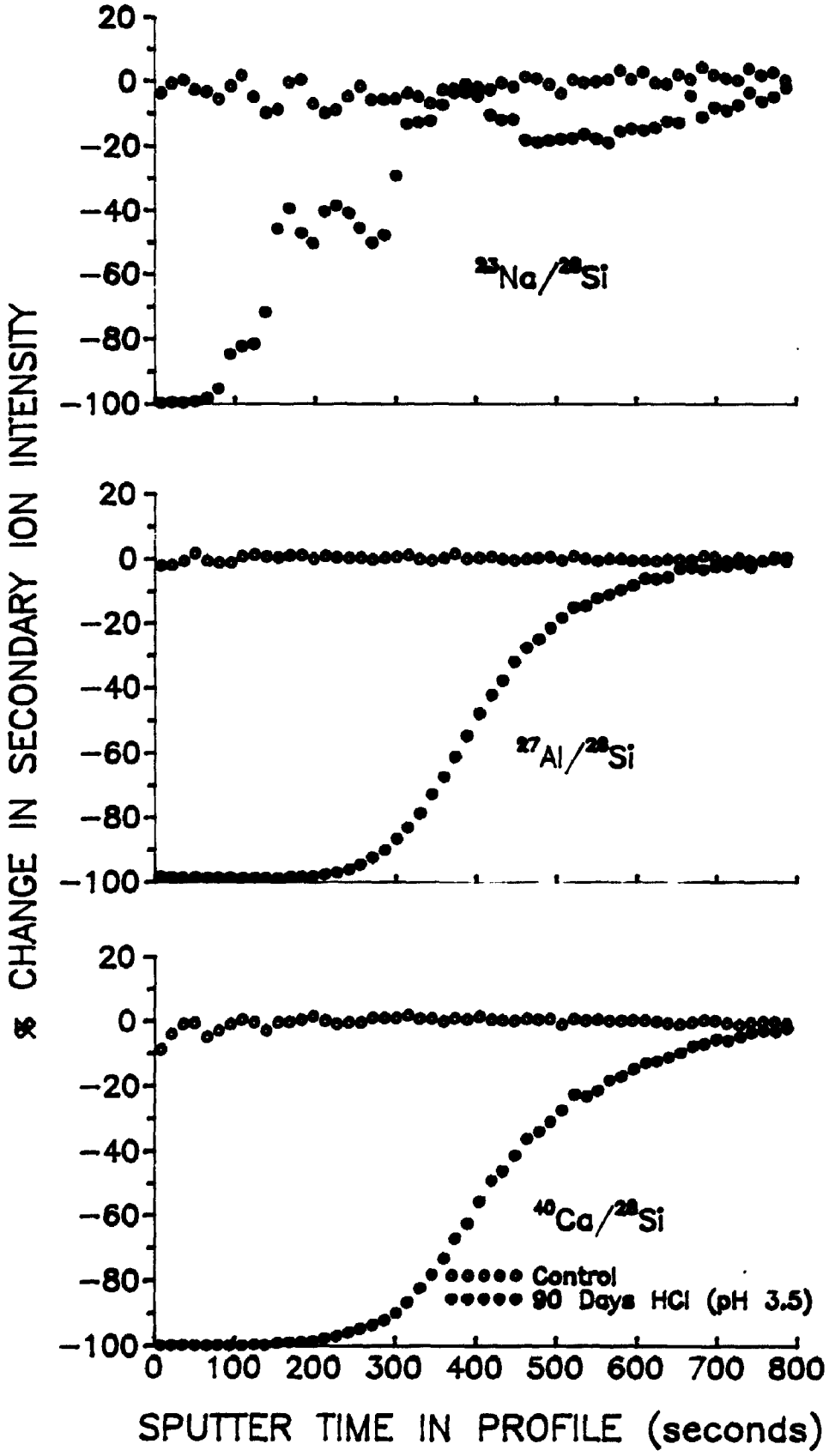
20
0
-20
-40
-60
-80
-100
$^{23}Na/^{28}Si$
$^{27}Al/^{28}Si$
$^{40}Ca/^{28}Si$
Control
90 Days HCl (pH 3.5)
% CHANGE IN SECONDARY ION INTENSITY
0 100 200 300 400 500 600 700 800
SPUTTER TIME IN PROFILE (seconds)

Figure 6.3-6

SIMS depth profiles showing the percent difference in secondary ion intensity between one spot of analysis for both of the unreacted and reacted samples and the average of four points of analysis from the unreacted sample. $^{23}Na/^{28}Si$, $^{27}Al/^{28}Si$, and $^{40}Ca/^{28}Si$ are all shown separately. The closed circles represent labradorite leached in aqueous HCl (pH 3.5) for a period of 90 days, and the open circles represent the unreacted labradorite sample. The percentage change in secondary ion intensity (ordinate) is plotted against time (seconds) of sputtering in the profile (abscissa).

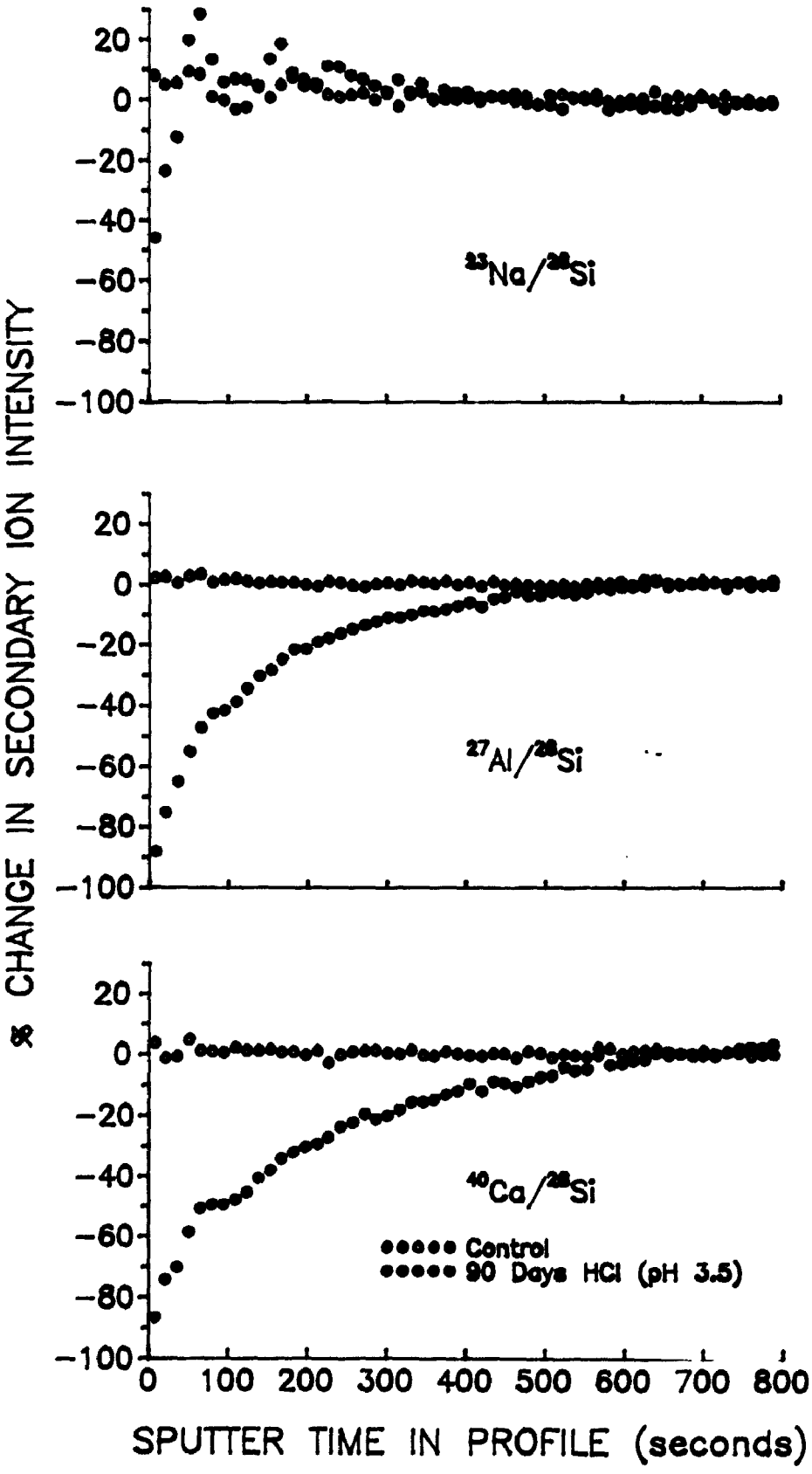
20
0
-20
-40
-60
-80
-100
$^{23}Na/^{28}Si$
$^{27}Al/^{28}Si$
$^{40}Ca/^{28}Si$
Control
90 Days HCl (pH 3.5)
% CHANGE IN SECONDARY ION INTENSITY
0 100 200 300 400 500 600 700 800
SPUTTER TIME IN PROFILE (seconds)

Figure 6.3-7

SIMS depth profiles showing the percent difference in secondary ion intensity between one spot of analysis for both of the unreacted and reacted samples and the average of four points of analysis from the unreacted sample. $^{23}Na/^{28}Si$, $^{27}Al/^{28}Si$, and $^{40}Ca/^{28}Si$ are all shown separately. The closed circles represent andesine leached leached in aqueous HCl (pH 3.5) for a period of 90 days, and the open circles represent the unreacted andesine sample. The percentage change in secondary ion intensity (ordinate) is plotted against time (seconds) of sputtering in the profile (abscissa).

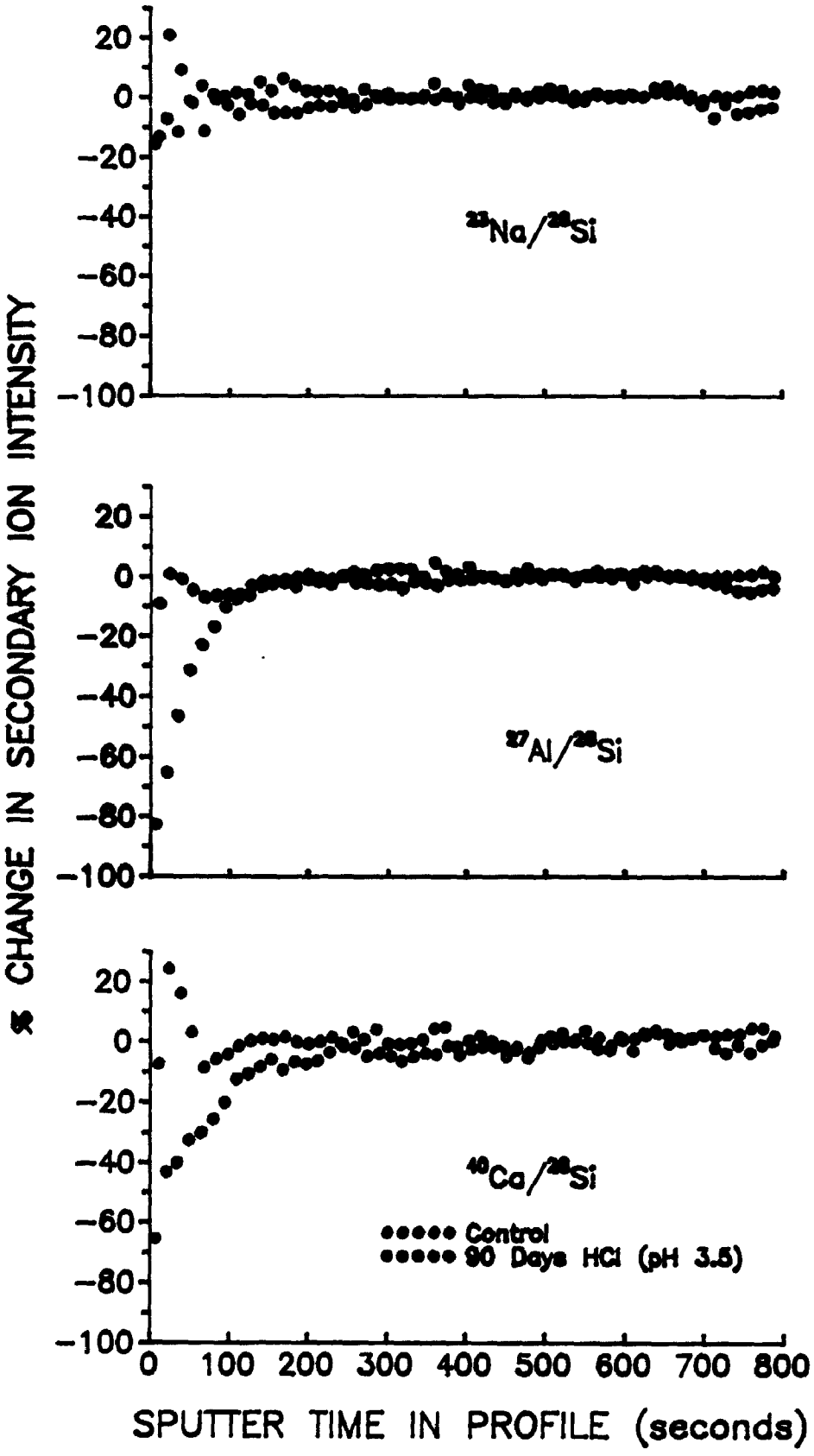
% CHANGE IN SECONDARY ION INTENSITY
20
0
-20
-40
-60
-80
-100
$^{23}Na/^{28}Si$
$^{27}Al/^{28}Si$
$^{40}Ca/^{28}Si$
Control
90 Days HCl (pH 3.5)
0
100
200
300
400
500
600
700
800
SPUTTER TIME IN PROFILE (seconds)

Figure 6.3-8

SIMS depth profiles showing the percent difference in secondary ion intensity between one spot of analysis for both of the unreacted and reacted samples and the average of four points of analysis from the unreacted sample. $^{23}Na/^{28}Si$, $^{27}Al/^{28}Si$, and $^{40}Ca/^{28}Si$ are all shown separately. The closed circles represent oligoclase leached in aqueous HCl (pH 3.5) for a period of 90 days, and the open circles represent the unreacted oligoclase sample. The percentage change in secondary ion intensity (ordinate) is plotted against time (seconds) of sputtering in the profile (abscissa).

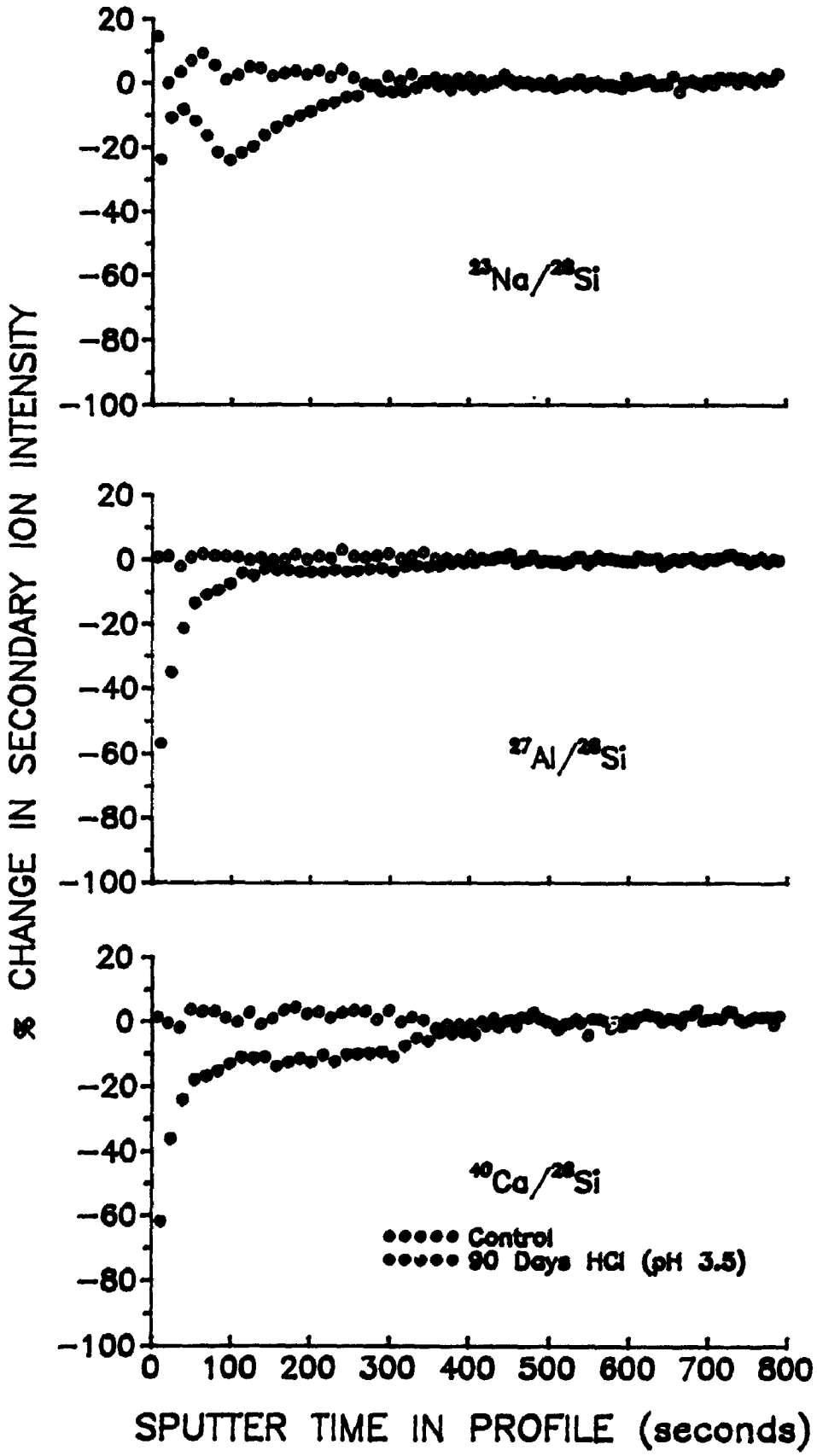
20
0
-20
-40
-60
-80
-100
$^{23}Na/^{28}Si$
$^{27}Al/^{28}Si$
$^{40}Ca/^{28}Si$
Control
90 Days HCl (pH 3.5)
% CHANGE IN SECONDARY ION INTENSITY
0 100 200 300 400 500 600 700 800
SPUTTER TIME IN PROFILE (seconds)

Figure 6.3-9

SIMS depth profiles showing the percent difference in secondary ion intensity between one spot of analysis for both of the unreacted and reacted samples and the average of four points of analysis from the unreacted sample. $^{23}Na/^{28}Si$, $^{27}Al/^{28}Si$, and $^{40}Ca/^{28}Si$ are all shown separately. The closed circles represent albite leached in aqueous HCl (pH 3.5) for a period of 90 days, and the open circles represent the unreacted albite sample. The percentage change in secondary ion intensity (ordinate) is plotted against time (seconds) of sputtering in the profile (abscissa).

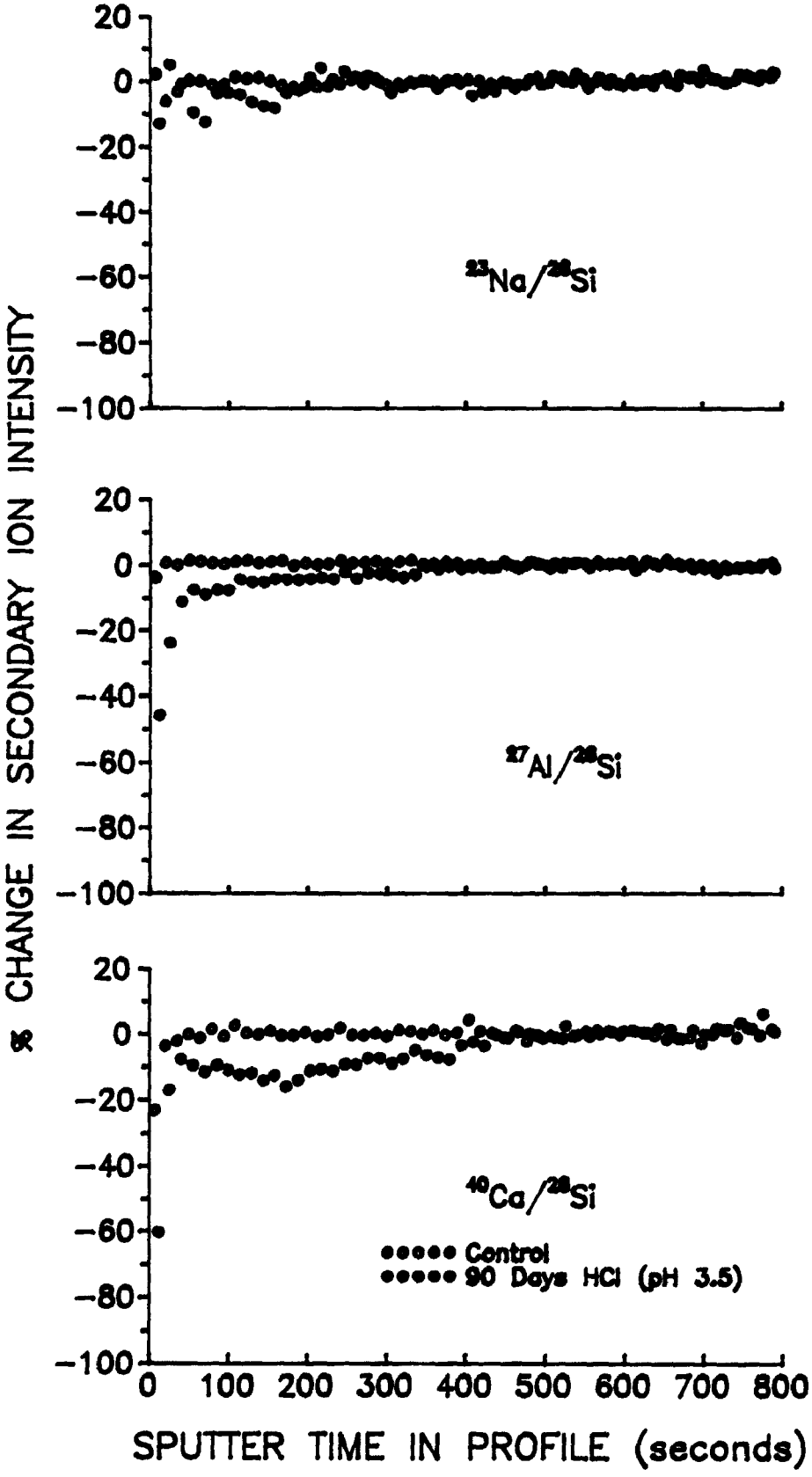
20
0
-20
-40
-60
-80
-100
$^{23}Na/^{28}Si$
$^{27}Al/^{28}Si$
$^{40}Ca/^{28}Si$
% CHANGE IN SECONDARY ION INTENSITY
Control
90 Days HCl (pH 3.5)
0 100 200 300 400 500 600 700 800
SPUTTER TIME IN PROFILE (seconds)

rate = 1 to 2 Å s^{-1} 100 nA^{-1}). As for the albite specimen (the sodium end member), the leached zone is not as readily defined (see Figure 6.3-9). The SIMS profiles for albite show a zone somewhat less leached and on the order of 400 to 800 Å in thickness (Figure 6.3-9). The results for each plagioclase specimen (Figures 6.3-5 to 6.3-9) are summarized in Table 6.3-1. Table 6.3-1 (and Figures 6.3-5 to 6.3-9) show that for the more sodium rich plagioclase samples (albite, oligoclase and andesine) the leached zones are not as depleted and are much thinner than those for the more calcium rich plagioclases (labradorite and bytownite). In most cases, the profiles for sodium are difficult to interpret, but the XPS results (see section 6.3.4) indicate that sodium is apparently depleted near the surface, and thus is believed to behave much like calcium and aluminum.

For the labradorite and bytownite specimens, the shapes of the aluminum and calcium profiles are remarkably similar (see Figures 6.3-5 and 6.3-6). The observed secondary ion intensity is initially very low and then rises sharply during the next few hundred seconds of the profile, suggesting extreme leaching of all elements except silicon from the surface. Deeper within the profiles, the secondary ion signal flattens and approaches values representative of the bulk of the specimen. Elements may diffuse across this zone, both from the unaltered feldspar to solution and in the opposite direction. If steady-state diffusion were the rate-limiting step, a linear profile may be expected only if

Table 6.3-1

Summary of SIMS depth profiles for the plagioclase specimens after 90 days dissolution in aqueous HCl (pH 3.5). Repeated determinations (4 spots) were within 10 % of these values.

a) Percent change in the secondary ion signal between the reacted and unreacted plagioclase sample surfaces.

Specimen	Albite	Oligoclase	Andesine	Labradorite	Bytownite
$^{23}Na/^{28}Si$	-15	-22	-18	-45	-100
$^{27}Al/^{28}Si$	-45	-58	-82	-88	-100
$^{40}Ca/^{28}Si$	-60	-60	-65	-88	-100

b) Thickness in angstoms of the leached zone for each element (sputter rate = 1 to 2 Å s^{-1} 100 nA^{-1}).

Specimen	Albite	Oligoclase	Andesine	Labradorite	Bytownite
$^{23}Na/^{28}Si$	ND*	400-800	ND	ND	800-1600
$^{27}Al/^{28}Si$	400-800	400-800	150-300	600-1200	800-1600
$^{40}Ca/^{28}Si$	400-800	400-800	200-400	600-1200	800-1600

* ND = not determined.

the diffusion coefficients remain constant throughout the altered zone. Although, if the diffusion coefficients vary with composition (i.e. across the layer), the gradients are then expected to be non-linear. However, with respect to feldspar dissolution, the variation of diffusion coefficients with composition has not yet been addressed.

It is necessary to emphasize that the SIMS profiles are only qualitative. In some profiles (see Figures 6.3-4 through 6.3-14) the change in secondary ion intensity is not continuous with the depth of the altered layer. Until more detailed data are available, it would be a serious mistake to imply that concentration gradients within the layer change with the ion intensity observed in the profiles.

Dissolution of Plagioclase in Water (pH 5.7)

The leached zones are not as evident on the plagioclase specimens that were leached with doubly distilled deionized water. The results from the experiments lasting 90 days are similar to those from experiments lasting 60 days. It is for this reason that only the results from the 60 day experiments will be presented here. Sample SIMS profiles for the plagioclase specimens undergoing dissolution in water for 60 days are shown in Figures 6.3-10 through 6.3-14. Again, only one of the four analyses has been presented. These results are also summarized in Table 6.3-2. The uncertainty in the sodium profiles is evident. The altered zones for all specimens

were found to be in the range of 75 to 400 Å thick. The amount of depletion and thickness of the altered zone is not seen to vary with plagioclase composition like the experiments where leaching was done under acidic conditions (pH 3.5). A lack of correlation between the nature of the leached zone and plagioclase composition may be a result of the leached layer not being as easily defined in the SIMS profiles. Again, these estimated depths for the leached layers are within the ranges proposed by Correns and von Engelhardt,[22] and Correns.[23-25]

The estimated thickness of the altered zones formed during dissolution in water (pH 5.7) (Figures 6.3-10 to 6.3-14) and HCl (pH 3.5) (Figures 6.3-5 to 6.3-9) are significantly different. The extent of depletion (sodium, aluminum and calcium) as interpreted by changes in secondary ion intensity is also significantly different in the two experiments. The influence of pH on the thickness and composition of the altered layer has been previously discussed by Helgeson et al.[71] and Chou and Wollast.[55] Helgeson et al.[71] suggest that the order of reaction with respect to the hydrogen ion concentration is greater than one whereas Chou and Wollast[55] prefer an order less than one (fractional). From these results it seems that the pH of the reactant solution has a strong effect on the nature of the altered layer. However, without any data regarding the total flux of material from the feldspar to solution, it is

Figure 6.3-10

SIMS depth profiles showing the percent difference in secondary ion intensity between one spot of analysis for both of the unreacted and reacted samples and the average of four points of analysis from the unreacted sample. $^{23}Na/^{28}Si$, $^{27}Al/^{28}Si$, and $^{40}Ca/^{28}Si$ are all shown separately. The closed circles represent bytownite leached in water (pH 5.7) for a period of 60 days, and the open circles represent the unreacted bytownite sample. The percentage change in secondary ion intensity (ordinate) is plotted against time (seconds) of sputtering in the profile (abscissa).

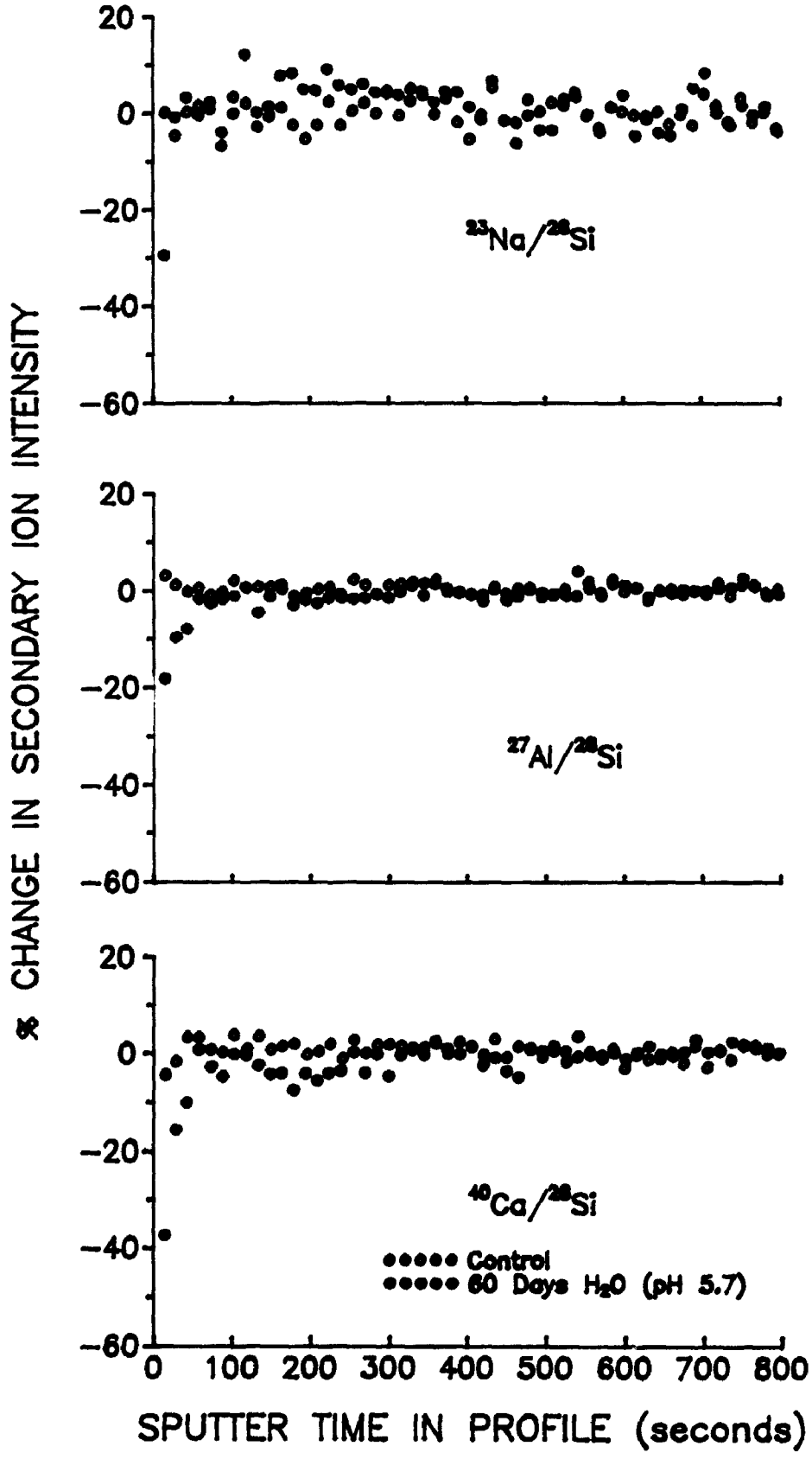
20
0
−20
−40
−60
$^{23}Na/^{28}Si$
$^{27}Al/^{28}Si$
$^{40}Ca/^{28}Si$
% CHANGE IN SECONDARY ION INTENSITY
Control
60 Days H_2O (pH 5.7)
0 100 200 300 400 500 600 700 800
SPUTTER TIME IN PROFILE (seconds)

Figure 6.3-11

SIMS depth profiles showing the percent difference in secondary ion intensity between one spot of analysis for both of the unreacted and reacted samples and the average of four points of analysis from the unreacted sample. $^{23}Na/^{28}Si$, $^{27}Al/^{28}Si$, and $^{40}Ca/^{28}Si$ are all shown separately. The closed circles represent labradorite leached in water (pH 5.7) for a period of 60 days, and the open circles represent the unreacted labradorite sample. The percentage change in secondary ion intensity (ordinate) is plotted against time (seconds) of sputtering in the profile (abscissa).

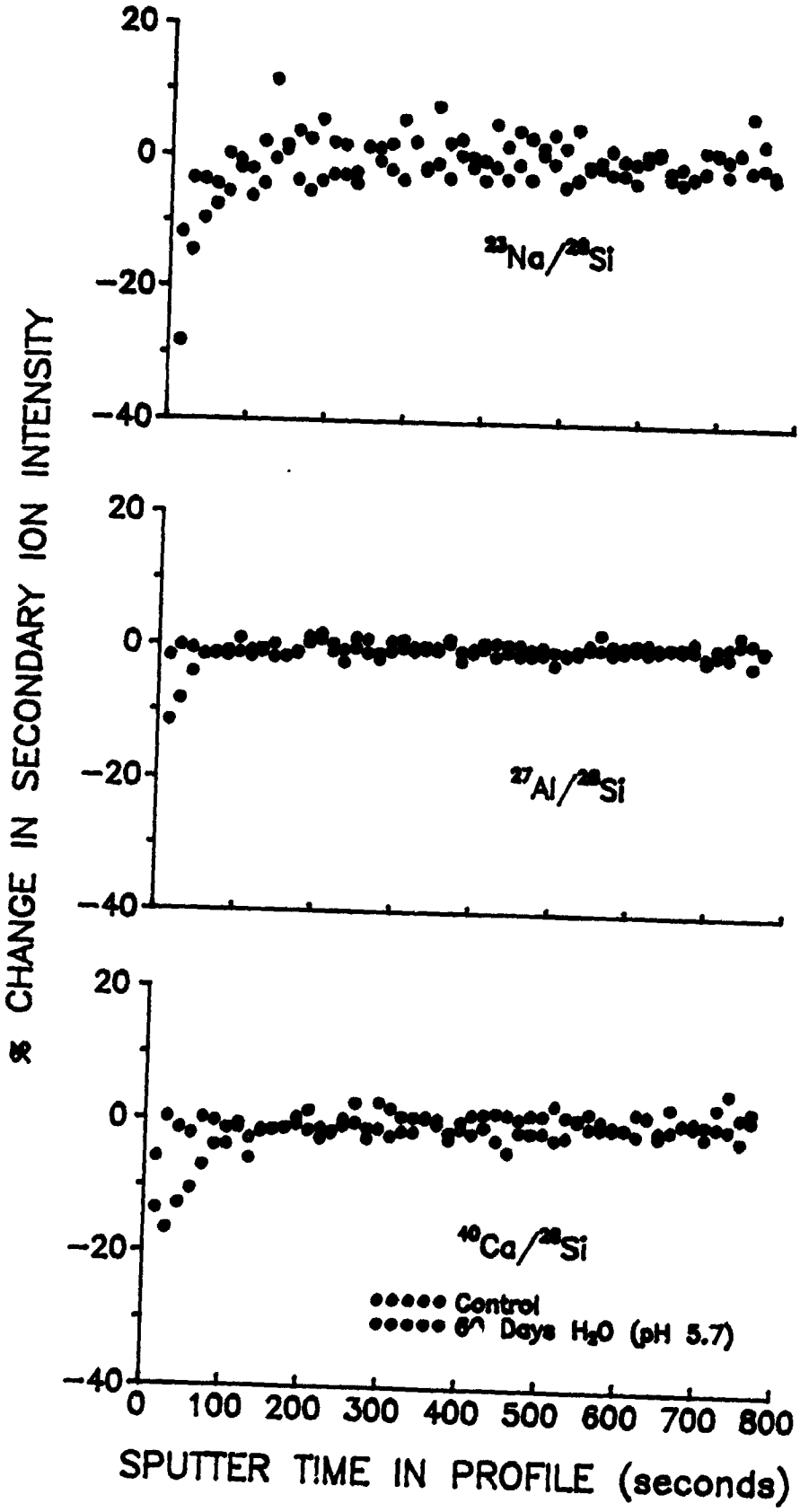
20
0
-20
-40
$^{23}Na/^{28}Si$
20
0
-20
-40
$^{27}Al/^{28}Si$
20
0
-20
-40
$^{40}Ca/^{28}Si$
Control
6^ Days H_2O (pH 5.7)
0 100 200 300 400 500 600 700 800
SPUTTER TIME IN PROFILE (seconds)
% CHANGE IN SECONDARY ION INTENSITY

Figure 6.3-12

SIMS depth profiles showing the percent difference in secondary ion intensity between one spot of analysis for both of the unreacted and reacted samples and the average of four points of analysis from the unreacted sample. $^{23}Na/^{28}Si$, $^{27}Al/^{28}Si$, and $^{40}Ca/^{28}Si$ are all shown separately. The closed circles represent andesine leached in water (pH 5.7) for a period of 60 days, and the open circles represent the unreacted andesine sample. The percentage change in secondary ion intensity (ordinate) is plotted against time (seconds) of sputtering in the profile (abscissa).

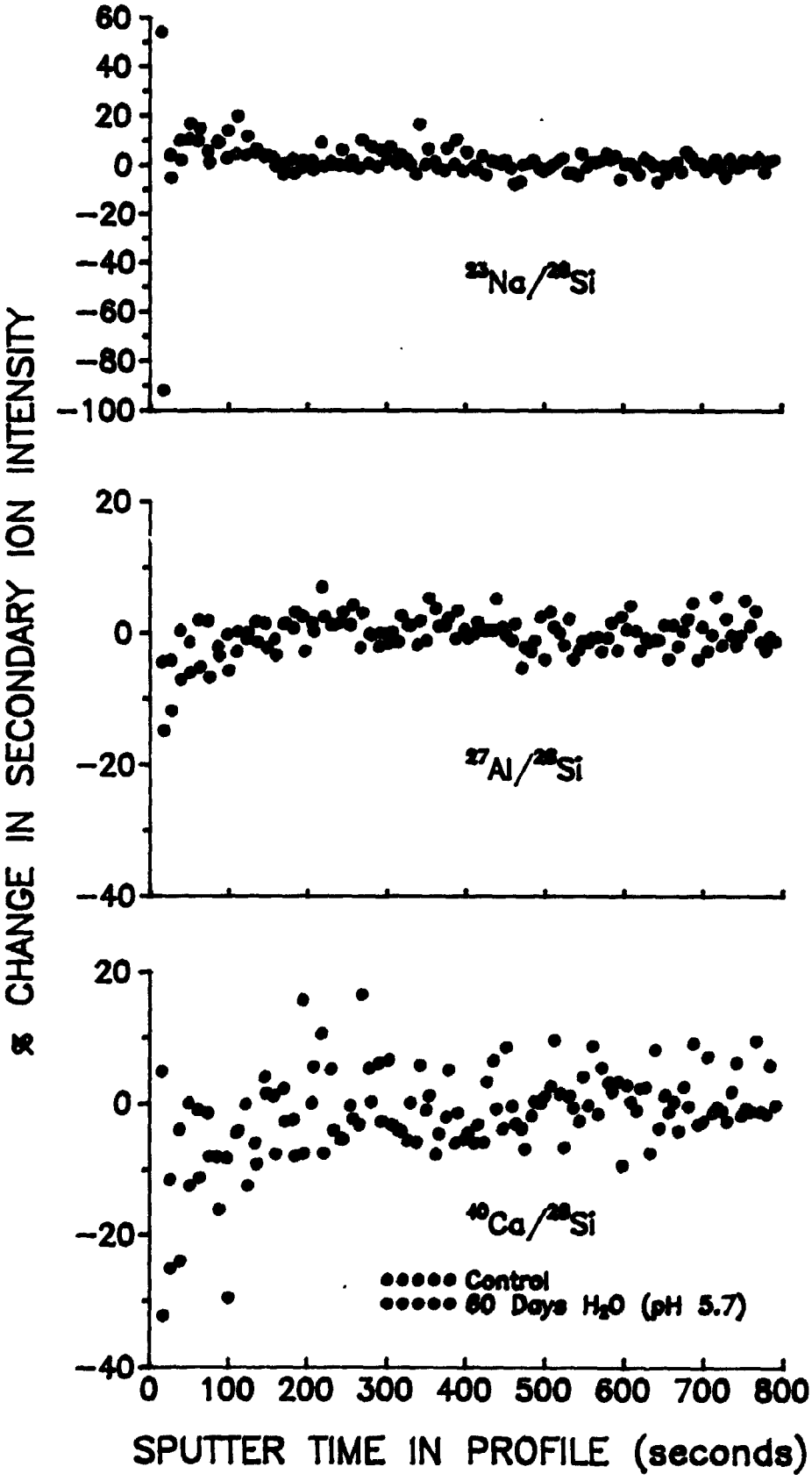
% CHANGE IN SECONDARY ION INTENSITY
60
40
20
0
-20
-40
-60
-80
-100
$^{23}Na/^{28}Si$
20
0
-20
-40
$^{27}Al/^{28}Si$
20
0
-20
-40
$^{40}Ca/^{28}Si$
Control
60 Days H_2O (pH 5.7)
0 100 200 300 400 500 600 700 800
SPUTTER TIME IN PROFILE (seconds)

Figure 6.3-13

SIMS depth profiles showing the percent difference in secondary ion intensity between one spot of analysis for both of the unreacted and reacted samples and the average of four points of analysis from the unreacted sample. $^{23}Na/^{28}Si$, $^{27}Al/^{28}Si$, and $^{40}Ca/^{28}Si$ are all shown separately. The closed circles represent oligoclase leached in water (pH 5.7) for a period of 60 days, and the open circles represent the unreacted oligoclase sample. The percentage change in secondary ion intensity (ordinate) is plotted against time (seconds) of sputtering in the profile (abscissa).

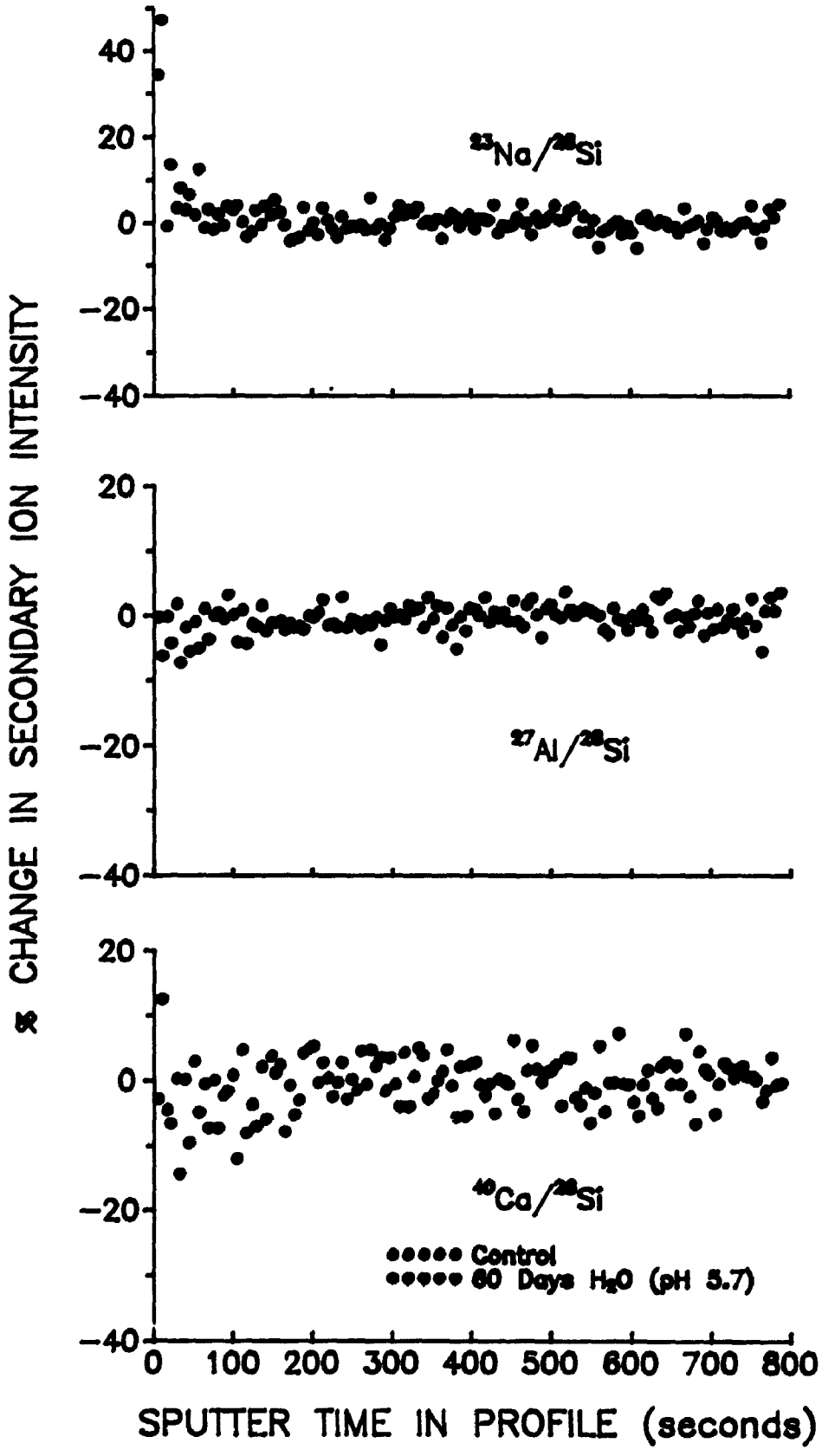
40
20
0
−20
−40
$^{23}Na/^{28}Si$
20
0
−20
−40
$^{27}Al/^{28}Si$
20
0
−20
−40
$^{40}Ca/^{28}Si$
Control
60 Days H_2O (pH 5.7)
0 100 200 300 400 500 600 700 800
SPUTTER TIME IN PROFILE (seconds)
% CHANGE IN SECONDARY ION INTENSITY

Figure 6.3-14

SIMS depth profiles showing the percent difference in secondary ion intensity between one spot of analysis for both of the unreacted and reacted samples and the average of four points of analysis from the unreacted sample. $^{23}Na/^{28}Si$, $^{27}Al/^{28}Si$, and $^{40}Ca/^{28}Si$ are all shown separately. The closed circles represent albite leached in water (pH 5.7) for a period of 60 days, and the open circles represent the unreacted albite sample. The percentage change in secondary ion intensity (ordinate) is plotted against time (seconds) of sputtering in the profile (abscissa).

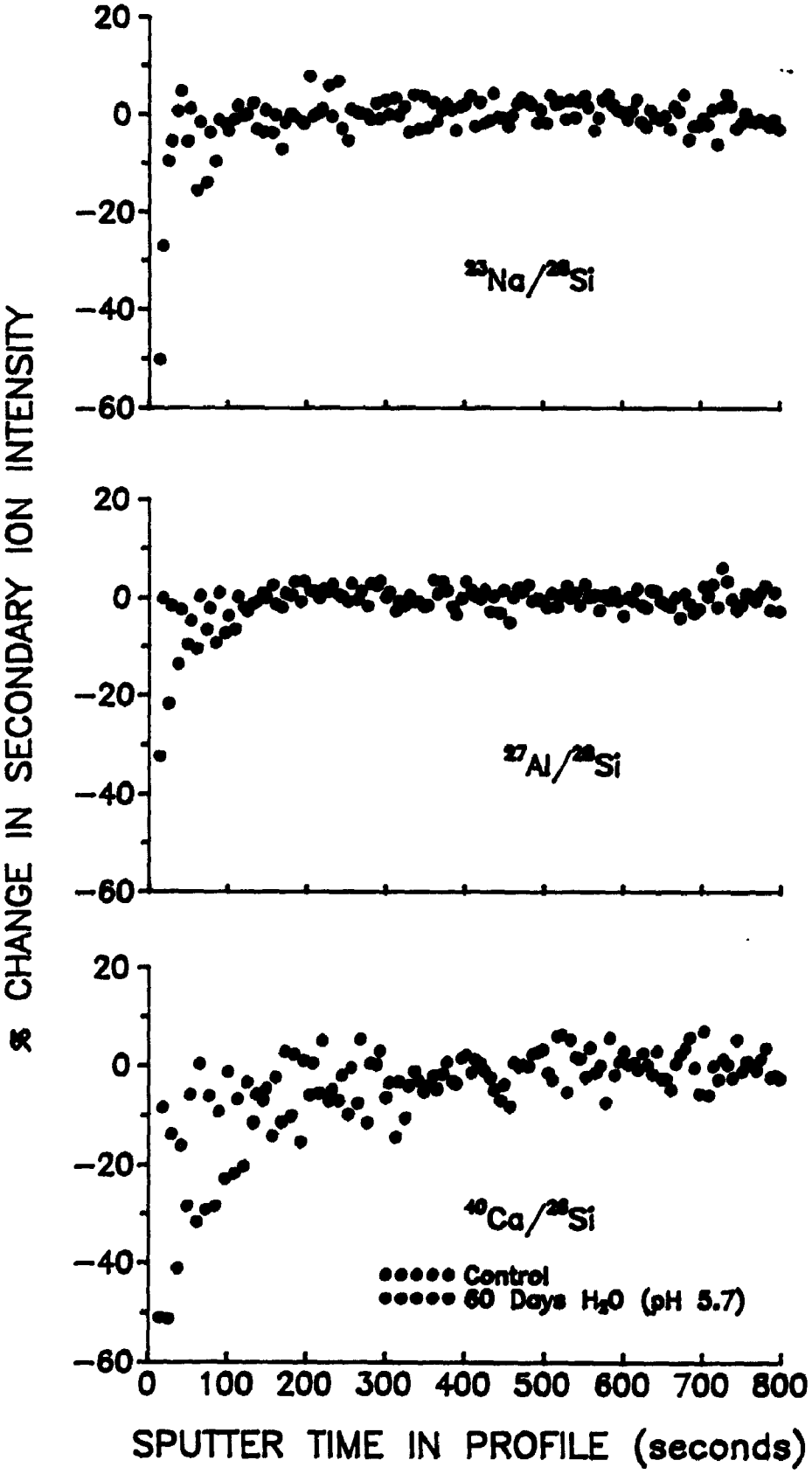
20
0
-20
-40
-60
$^{23}Na/^{28}Si$
20
0
-20
-40
-60
$^{27}Al/^{28}Si$
20
0
-20
-40
-60
$^{40}Ca/^{28}Si$
Control
60 Days H_2O (pH 5.7)
0 100 200 300 400 500 600 700 800
SPUTTER TIME IN PROFILE (seconds)
% CHANGE IN SECONDARY ION INTENSITY

Table 6.3-2

Summary of SIMS depth profiles for the plagioclase specimens after 60 days dissolution in double distilled deionized water (pH 5.7). Repeated determinations (4 spots) were within 10 % of these values.

a) Percent change in the secondary ion signal between the reacted and unreacted plagioclase sample surfaces.

Specimen	Albite	Oligoclase	Andesine	Labradorite	Bytownite
$^{23}Na/^{28}Si$	-10	ND	ND	-20	ND
$^{27}Al/^{28}Si$	-32	-8	-15	-12	-18
$^{40}Ca/^{28}Si$	-50	-10	-30	-15	-30

b) Thickness in angstoms of the leached zone for each element (sputter rate = 1 to 2 Å s^{-1} 100 nA^{-1}).

Specimen	Albite	Oligoclase	Andesine	Labradorite	Bytownite
$^{23}Na/^{28}Si$	ND*	ND	ND	ND	ND
$^{27}Al/^{28}Si$	150-300	150-300	150-300	60-120	75-150
$^{40}Ca/^{28}Si$	300-600	200-400	200-400	100-200	200-400

* ND = not determined.

not possible to comment on the order of reaction with respect to the hydrogen ion concentration.

6.3.4 XPS Results

While XPS spectra of only one specimen (labradorite) are presented (see Figure 6.3-15), the results for all specimens are reported in Tables 6.3-3 and 6.3-4. In Tables 6.3-3 and 6.3-4, the peak areas of the reacted samples have been normalized to Si (2p) from the control sample. In calculating the percentage change in the peak area, the normalized area of the reacted sample was subtracted from that of the control sample. This difference is then expressed as a percentage of the original peak area (i.e. the peak area of that particular element from the control specimen). This may be seen by the following equation:

$$\left\{\left[\left[\begin{array}{c}\text{peak area from} \\ \text{reacted sample}\end{array}\right]-\left[\begin{array}{c}\text{peak area} \\ \text{from control}\end{array}\right]\right]\div\left[\begin{array}{c}\text{peak area} \\ \text{from control}\end{array}\right]\right\} \times 100$$

In Figure 6.3-15, a sample spectrum from the labradorite control specimen is presented along with one spectrum from each of the two reacted samples (60 days in pH 5.7, and 90 days in pH 3.5). After reacting the labradorite (and the other plagioclase specimens) with water for 60 days there is a reduction in the area of the sodium (Auger and 2s) and calcium (2s and 2p) peaks while the silicon (2s and 2p) peaks remain similar in area with those

Figure 6.3-15

X-ray photoelectron spectra (photoelectron counts on the ordinate vs. binding energy of the electrons on the abscissa) for three labradorite samples; (1) unreacted, (2) reacted in water (pH 5.7) for a period of 60 days, and (3) reacted in an HCl solution (pH 3.5) for a period of 90 days. Note the reduction in peak areas for sodium, calcium and aluminum in the reacted compared with the unreacted samples. The presence of fluorine (F) in the control spectra may be accounted for by the use of inert "freon dusters" during sample preparation. The C and N in the spectra are representative of carbon and nitrogen absorbed onto the surface and are easily removed with brief sputtering using an Ar^{+} ion beam.

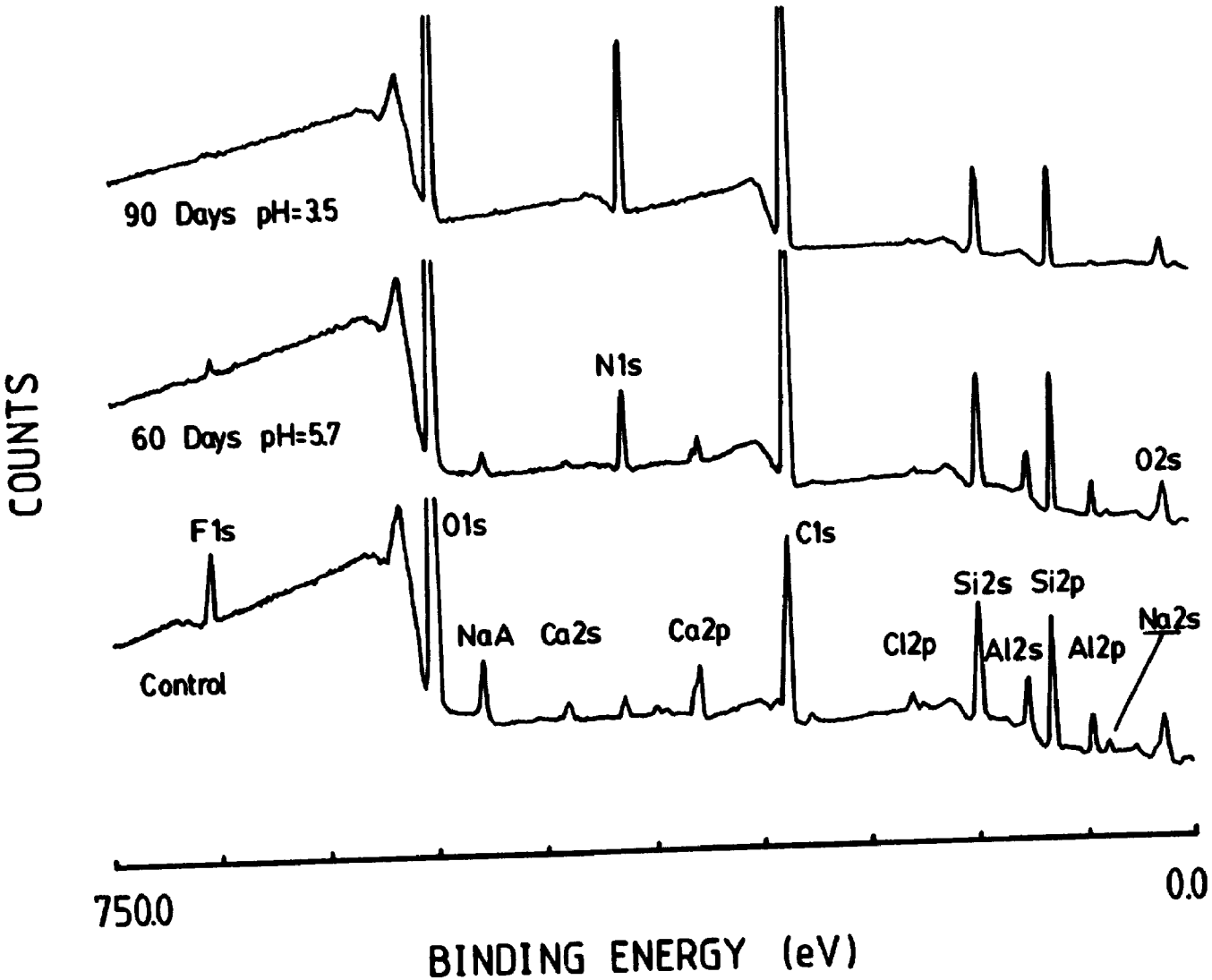
90 Days pH=3.5
60 Days pH=5.7
Control
COUNTS
F1s
O1s
N1s
C1s
O2s
NaA
Ca2s
Ca2p
Cl2p
Si2s
Si2p
Al2s
Al2p
Na2s
750.0
0.0
BINDING ENERGY (eV)

Table 6.3-3

Percent differences in the photoelectron peak areas (relative to Si 2p) between the reacted (60 days in doubly distilled deionized water, pH 5.7) and unreacted plagioclase. Repeated determinations were within 10 % of these values. See text for details of the calculation.

	Albite	Oligoclase	Oligoclase*	Andesine	Labradorite	Bytownite
Na (Auger)	-67	39	-80	-23	-49	-79
Al (2p)	-55	33	-53	-4	-18	-7
Ca (2p)	-100†	-39	-100†	-81	-55	-71

* Oligoclase reacted for 90 under the same conditions (pH 5.7)

† Not detected in the reacted sample.

Table 6.3-4

Percent differences in the photoelectron peak areas (relative to Si 2p) between the reacted (90 days in an aqueous HCl solution, pH 3.5)and unreacted plagioclase. Repeated determinations were within 10 % of these values. See text for details of the calculation.

	Albite	Oligoclase	Andesine	Labradorite	Bytownite
Na (Auger)	-76	-78	-86	-87	-93
Al (2p)	-65	-83	-81	-94	-98
Ca (2p)	-100†	-30	-100†	-98	-97

† Not detected in the reacted sample.

from the control specimen (see Figure 6.3-15). There also appears to be some reduction in the area of the aluminum (2s and 2p) peaks. These reductions in peak area are better represented by the data in Table 6.3-3. The labradorite (as well as the other plagioclase specimens) which has undergone dissolution in aqueous HCl (pH 3.5), displays dramatically reduced areas for the sodium (Auger and 2s), calcium (2s and 2p) and aluminum (2s and 2p) peaks (see Figure 6.3-15 and Table 6.3-4). The photoelectron results for all reacted samples are similar to the corresponding data obtained with the SIMS technique.

The anomalous results for the oligoclase specimen reacted in water (pH 5.7) for 60 days are not understood. Repeated measurements (XPS) have produced similar anomalous results. However, the SIMS results (both 60 and 90 days dissolution in water) and the XPS results for 90 days dissoluion in water show depletion of sodium, aluminum and calcium like the other plagioclase samples studied. The XPS results for 90 days dissolution of oligoclase also appear in Table 6.3-3.

With the use of photoelectron spectroscopy (Figure 6.3-15, and Tables 6.3-3 and 6.3-4) the behavior of sodium during the dissolution reactions becomes apparent. The XPS spectra show that the depletion of sodium from the surface is similar to that observed for aluminum and calcium. It can be concluded that the leached or altered layer is also devoid of sodium, and that the fate of sodium

during dissolution is very similar to that of calcium and/or aluminum. It also becomes apparent that the SIMS analyses for sodium are not reliable, probably the result of charge induced migration.[69,70]

The existence of the altered layer was not observed in earlier XPS studies[19] for the dissolution of alkali feldspars (sanidine). Differences in sample preparation, and charge neutralization and/or mounting techniques in the photoelectron experiments may possibly account for this controversy. It is also felt that without the aid of a computer when fitting the photoelectron spectra the subtle differences observed for dissolution at pH 5.7 may have been missed, and therefore the XPS results of Petrovic et al.,[19] are probably not that much different from those reported here. What must be pointed out, is that when calculating the thickness of the leached layer using photoelectron escape depths, Petrovic et al.[19] make some incorrect assumptions. The leached layer was assumed to be homogeneous throughout, and the composition was assumed to be equal to that of only silicon and aluminum from the parent feldspar. These assumptions are not reasonable, nor are they accomodated by the SIMS results given here. The SIMS data show that the other cations are still present at the surface (although somewhat depleted) and that the composition varies throughout the entire thickness of the altered zone. It is therefore felt that the XPS results given here support the results obtained by SIMS. By using

SIMS, the region below the surface has been analyzed, and thus the presence of a leached or altered layer on reacted feldspar surfaces has been documented. Based on similar profiles obtained from four spots of analysis, and the large sampling area in the SIMS experiments (~60 μm), these layers are believed to be continuous over the whole plagioclase surface.

6.3.5 Comparison with Other Recent Studies

The estimated depth of the altered zone formed due to leaching under acidic conditions (pH 3.5) is in agreement with that obtained for the penetration depth of hydrogen ions in leached diopside.[61] In their experiments, Petit et al.[61] used resonant nuclear reaction (RNR) analysis to depth profile the hydrogen concentration in diopside that had been leached under acidic conditions (pH 2) for ~75 days. A recent publication by Mogk and Locke[47] also reports a depleted layer of ~1200 Å for naturally weathered hornblende. In comparison with the results presented by Hochella et al.,[37] the nature of the altered layer seems to be somewhat similar for labradorite that had been reacted under quite different conditions (room temperature and pressure vs. hydrothermal alteration; 300°C and 300 bars). However, the layers quoted by Hochella et al.[37] (without depth profiling) are substantially thinner than those presented here. It is also worth noting that these results are qualitatively similar to those predicted by Correns and

von Engelhardt,[22] Correns[23-25] and Chou and Wollast[51,55] from the analyses of solutions obtained from the dissolution reactions.

6.4 Discussion and Conclusions

The application of the SIMS technique to the study of altered layers on mineral surfaces has been demonstrated. While techniques such as XPS and SAM are used to obtain surface information, the results obtained from depth profiling techniques (SIMS or RNR, or even depth profiling with an Ar^+ ion gun on an XPS or SAM system) are complementary to those from other surface techniques. Without depth profiling, it is difficult to comment on the near surface (or sub-surface) region of the reacted feldspars. The use of the specimen isolation technique in this study has been especially valuable since no conductive surface coatings were needed. It is felt that the presence of surface coatings (for charge neutralization purposes during SIMS analysis) may mask any information derived from the surface as may have been the case for Schott and Petit.[72] A significant problem with the SIMS technique is the analysis of sodium (and possibly some others). The data presented here provide strong, independent evidence for charge induced migration of sodium during analysis. Throughout the entire profiles (Figures 6.3-4 through 6.3-14) the Na^+ (secondary ion) signal at the begining of each profile appears to be enhanced as a result of charge

induced migration. It is therefore concluded that the percent change in the Na^+ ion signal represents a minimum amount of depletion. This is in qualitative agreement with the XPS data found in Tables 6.3-3 and 6.3-4.

With the SIMS results, it is now possible to identify and better characterize some type of altered layer on weathered feldspar surfaces as predicted by Correns and von Engelhardt,[22] Correns[23-25] and Chou and Wollast.[51,55] Other evidence for this layer has also been presented by Schott and Petit,[72] and Hochella et al.[37] Without some structural information of the first few hundred angstroms (from the surface) of the feldspar surface, it is difficult to reach conclusions regarding the nature of this altered zone. Hochella et al.[37] have made extensive comments on the complexity of mineral dissolution. With the presence of this layer now established, other experiments must follow in order to determine the role of the altered layer in affecting the rates and mechanisms of the dissolution process.

It seems that a brief comment on the process that forms the altered layer is in order. Although the experiments of Petit et al.[61] involve a different mineral and slightly different reaction conditions (diopside in pH 2 for ~75 days) some comparisons with these data can be made. As stated earlier, the depth of hydrogen ion penetration (determined from RNR analysis) is qualitatively similar to the depths reported here for the leaching of sodium,

aluminum and calcium. Although Petit et al.[61] suggest that the hydrogen profiles are the result of water penetrating into the feldspar lattice, it is more likely that there is replacement of Na^+ and Ca^+ ions from the feldspar by H^+ ions from solution (H^+ is preferred over H_3O^+ due to size restrictions; see reference 55) to form a the altered zone. This exchange of H^+ for the Na^+ and Ca^+ seems reasonable since the charge balance of the feldspar remains unchanged.

Finally, it must be noted that the composition of the altered layer found during laboratory dissolution is quite different from that found for weathered oligoclase grains from podzolic soils of the Plastic Lake catchment (see reference 41 and chapter 7). In the naturally weathered oligoclase grains, altered layers were depleted in sodium, calcium and silicon, but enriched (residually?) in aluminum to depths of 300 to 800 Å.[41] These results have since been confirmed by XPS (Nesbitt and Muir, unpublished data). Given this information one must use extreme caution when interpreting results from laboratory studies of mineral dissolution when trying to understand processes occurring in nature. In the laboratory, the reaction conditions are closely monitored and the results obtained are applicable only to mineral dissolution under that specific set of conditions. In this study care was taken to ensure that no appreciable concentration gradients were formed in the reaction chambers, and that concentrations of dissolved species in the sample chamber were kept well below

saturation. In contrast, chemical weathering in nature is a very complex process involving many variables such as changes in solutions (organic acids and ligands), temperatures, biological activity and redox regimes, and flow rates of solutions over a significantly longer period of time. Formation of altered layers on naturally weathered oligoclase surfaces and their detection by SIMS is the subject of the following chapter.

CHAPTER 7

COMMENTS ON THE DISSOLUTION OF PLAGIOCLASE IN NATURAL ENVIRONMENTS

7.1 Introduction

The introduction of many anthropogenic (as well as naturally occurring) acids into the environment is becoming a growing concern. In some cases these acids may be neutralized by reactions with clay and/or feldspar minerals. The breakdown of plagioclase is an important acid consuming reaction. On the basis of congruent dissolution the following reaction (anorthite end member) is observed:

$$CaAl_2Si_2O_8 + 8H^+ \longrightarrow Ca^{2+} + 2Al^{3+} + 2SiO_{2(aq)} + 4H_2O$$

Whereas, if incongruent dissolution is the case and kaolinite is the end-product, the next reaction is observed:

$$CaAl_2Si_2O_8 + 2H^+ + H_2O \longrightarrow Ca^{2+} + Al_2Si_2O_5(OH)_4$$

Therefore, a better understanding of these reactions occurring at the surface of plagioclase during dissolution is necessary in order to evaluate the effects of acid deposition in many environments. Many studies regarding the kinetics of mineral dissolution under laboratory conditions have been presented in the literature. More recently, most efforts have concentrated on investigating the surfaces of

both naturally and laboratory dissolved feldspar minerals with various analytical techniques.

The previous chapter dealt with surface analysis (SIMS, XPS, and SEM) of plagioclase reacted under laboratory conditions. While the presence of some zone of alteration has been established, laboratory dissolution studies using different reaction conditions show differences in composition and depth of alteration (see references 37, 42, 61, 72, and the previous chapter). Weathering in nature is a complex process involving many different chemical reactions as well as physical transport and erosion. Therefore, the extension of laboratory studies to natural environments must be done with extreme care.

In this chapter (and a previous publication[41]) observations of leached layers on naturally weathered oligoclase are presented. These observations are then placed in context with those from chapter 6, and some of the other recent surface studies of mineral dissolution.[37,47,61]

7.2 Experimental

7.2.1 Sample Preparation

The samples used for this study were donated by D. Kirkwood and D. Borré (Department of Geology, U.W.O.). These stones were collected from a thin, 10,000-year-old, till deposited in the Plastic Lake Catchment, Ontario. There is no abundance of clay minerals in this catchment. Specimens containing many plagioclase (oligoclase

composition) grains were cut (2 × 2 × 1 cm) from these stones, then rinsed with tap water for approximately 10 seconds and air-dried. No further cleaning of the sample surfaces was done in an attempt to preserve as many structures resulting from the alteration process as possible. Samples for analysis contained only one weathered face. Electron probe analysis of a sample oligoclase grain is given in Table 7.2-1.

7.2.2 Surface Analysis

SIMS depth profiles were obtained using a CAMECA IMS 3f secondary ion microscope. Instrumentation and application of the CAMECA instrument have already been discussed. The method of specimen isolation[66,67] is an excellent technique for SIMS analysis of non-conductors without the need for conductive (gold) surface coatings. It is suspected that the use of a gold coating would lead to confusing results when analyzing near the gold/plagioclase interface. For this reason the method of specimen isolation was used. The specimen isolation technique also served as a form of kinetic energy filtering for the efficient removal of molecular ions from the mass spectra.

For specimen analysis, a primary beam of mass filtered $^{16}O^-$ ions at a net 15 to 16 kV and ~100 nA was rastered over a 250 × 250 μm area on the sample surface. Secondary ions were sampled from an area slightly greater than 50 μm well within the rastered area to reduce crater

Table 7.2-1

Composition of the oligoclase sample from Plastic Lake Catchment as determined by electron probe analysis.*

	Oligoclase
Na_2O	9.32
Al_2O_3	22.60
SiO_2	62.24
K_2O	0.23
CaO	4.46
TiO_2	0.02
Cr_2O_3	0.14
FeO	0.11
MnO	0.11
Total	99.23

* Wt. % oxides.

edge effects in the depth profiles. Under the above beam conditions, a sputter rate of 1 to 2 Å per second per 100 nA was assumed. Sputter rate determinations are presented in chapter 6. Weathered surfaces are in no way smooth, and it is therefore acknowledged that these sputter rates may be in error by as much as 50 %. This may lead to an uncertainty of up to 50 % for the estimated depths of the altered layers observed.

SEM analysis was also conducted to ensure that the weathered oligoclase faces were free of secondary products and other fine particulate matter. An ISI DS130 scanning electron microscope was used for this purpose. For SEM analysis it is always necessary to use conductive surface coatings (gold) for the analysis of non-conducting samples. These gold coatings may interfere with the SIMS depth profiles. For this reason, SEM analysis was always performed after SIMS analysis. It was not possible to ensure that the same grains were examined by each technique (SEM and SIMS), and hence it was generally assumed that the surfaces examined by SEM had not been exposed to the destructive nature of the SIMS ion beam.

7.3 Results and Discussion

7.3.1 Evidence of an Altered Layer

A sample SEM photomicrograph of the weathered oligoclase is shown in Figure 7.3-1. SEM observation shows that many of the plagioclase surfaces are homogeneous and

Figure 7.3-1

SEM photomicrograph of weathered oligoclase from the Plastic Lake Catchment, Ontario. Note the presence of etch pits and that the surface is fairly free of any secondary precipitates and/or other matter that may interfere with the SIMS analyses.

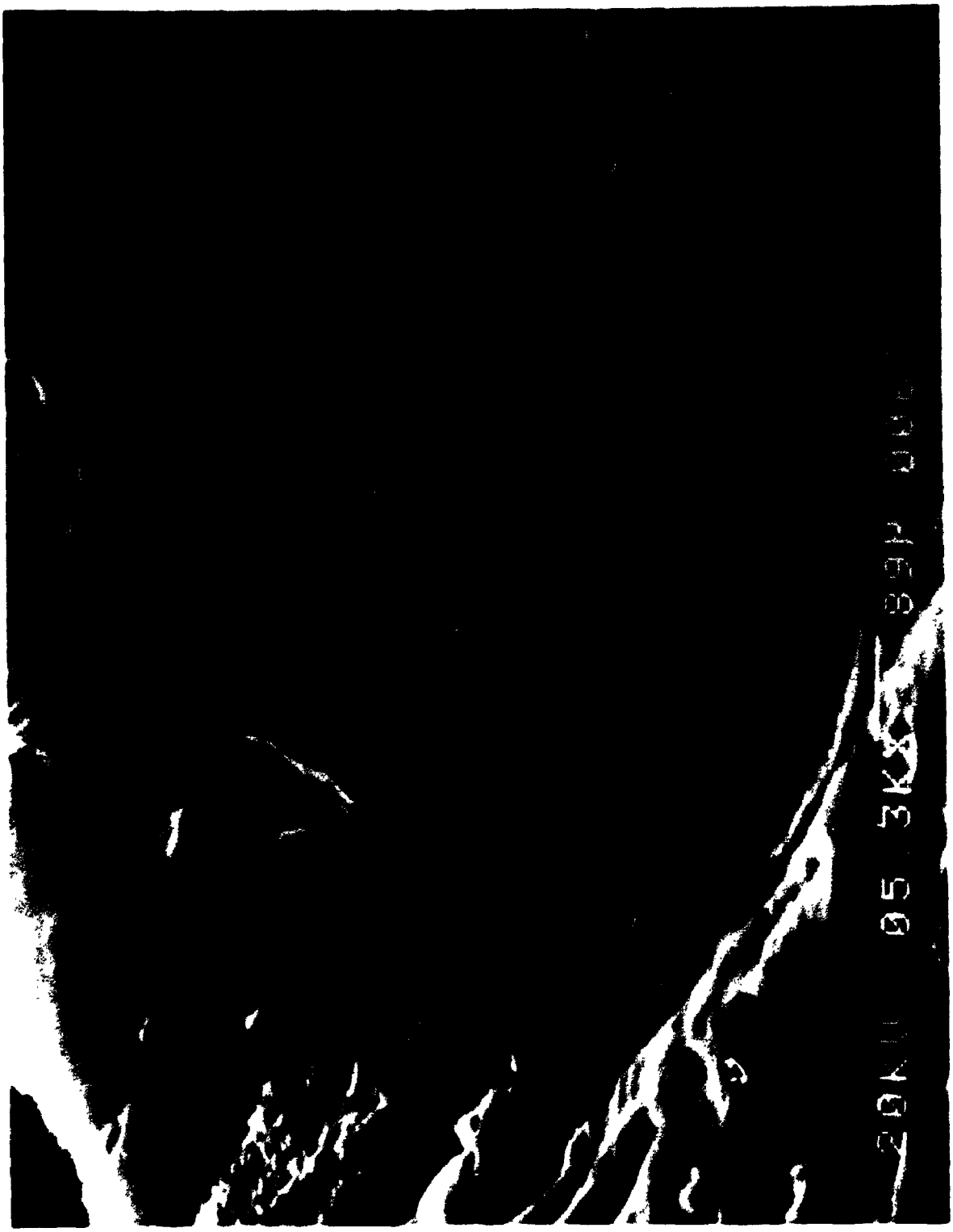
20kV 05 3KX SEM 000

free of significant amounts of particulate matter. Etch pits from the weathering process are also abundant in the SEM photomicrographs.

The raw SIMS data (before normalization) for the main feldspar elements (sodium, calcium, aluminum, silicon, and potassium) are presented in Figures 7.3-2 and 7.3-3 for typical unweathered and weathered oligoclase faces respectively. Unweathered oligoclase faces were obtained by cutting a section through the samples.

For the unaltered surface, (Figure 7.3-2) the enhanced signals for ^{23}Na and ^{39}K in the unaltered material (Figure 7.3-2) were at first somewhat disturbing. Initial enhancement of secondary ion production has been observed by other authors for sodium[69] and potassium,[70] and is believed to be the result of charge induced migration. Thus, the profiles for sodium and potassium are not represetative of the real composition. The signals for ^{27}Al, ^{28}Si and ^{40}Ca are constant throughout the entire profile as would be expected. It is also important to note that the ratio of aluminum to silicon at the surface is identical (deviations less than 3 %) to those from the interior.

In the profile obtained from the weathered face (Figure 7.3-3) the counts for ^{27}Al and ^{40}Ca are constant while the counts for ^{28}Si are depleted at the surface and then rise later in the profile. Although the ratio of aluminum to silicon is quite different at the surface, it is very similar to that of the unaltered sample during the last

Figure 7.3-2

SIMS depth profile of a sectioned oligoclase grain (assumed to be representative of an unleached surface) from the Plastic Lake Catchment, Ontario. The observed secondary ion intensity (counts) are plotted against time of analysis for the following isotopes; ^{23}Na, ^{27}Al, ^{28}Si, ^{39}K, and ^{40}Ca.

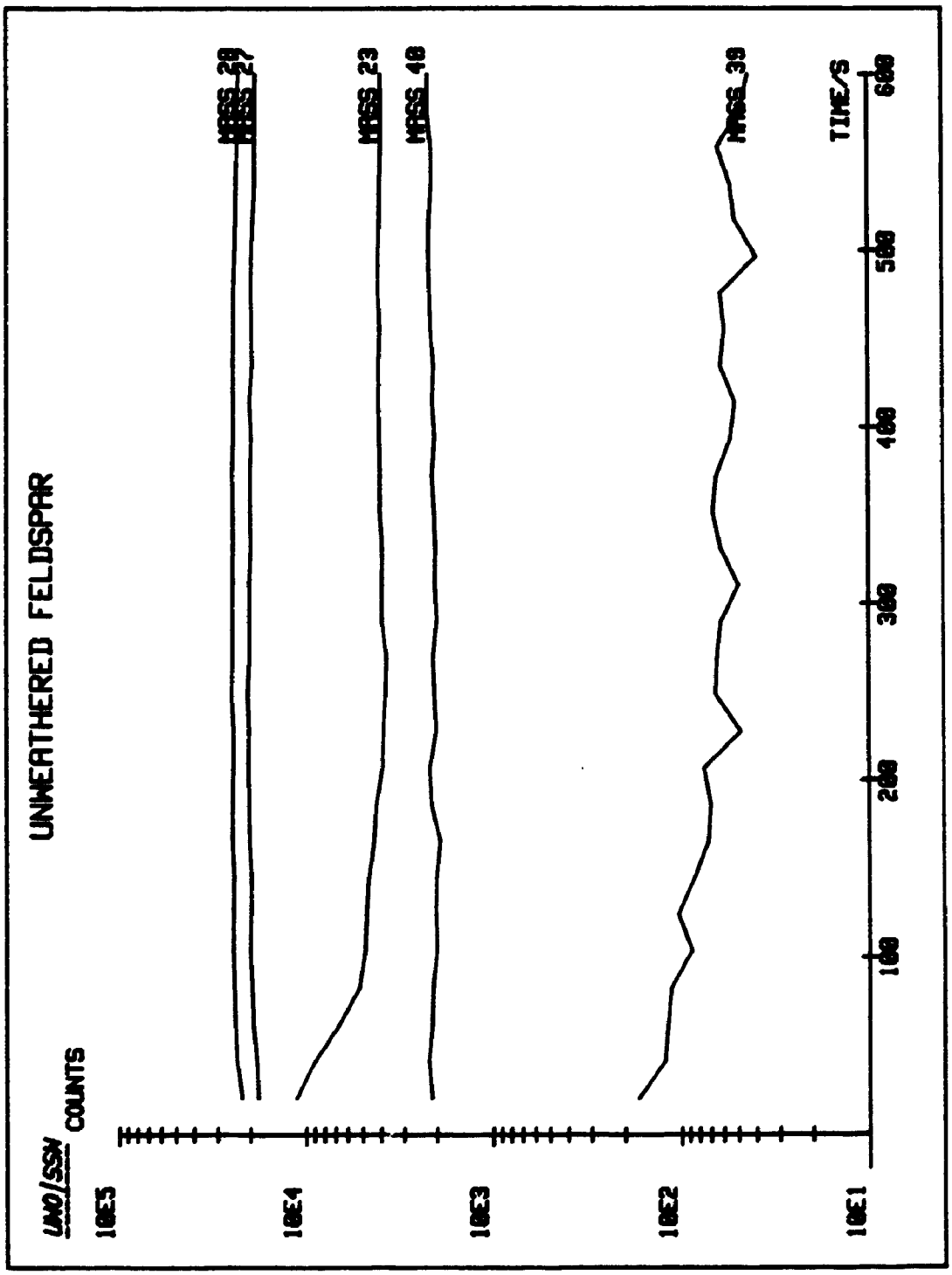
UNWEATHERED FELDSPAR
UNO/SSN COUNTS
10E3
10E4
10E3
10E2
10E1
MASS_29
MASS_27
MASS_23
MASS_48
MASS_39
TIME/S
100
200
300
400
500
600

Figure 7.3-3

SIMS depth profile of a weathered oligoclase grain from the Plastic Lake Catchment, Ontario (sample #3 in Figure 7.3-4). The observed secondary ion intensity (counts) are plotted against time of analysis for the following isotopes; ^{23}Na, ^{27}Al, ^{28}Si, ^{39}K, and ^{40}Ca.

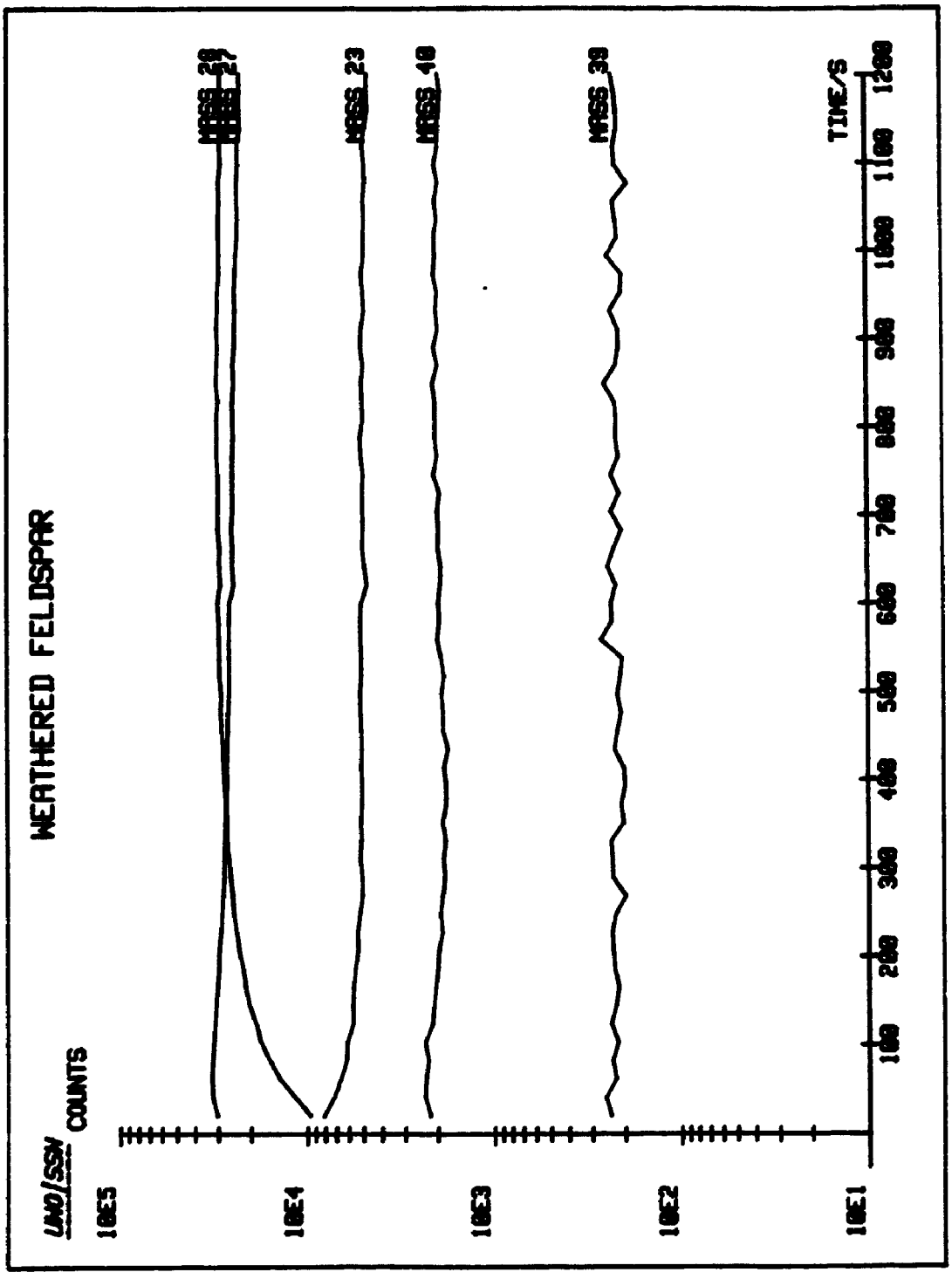
WEATHERED FELDSPAR
UNO/SSW COUNTS
10E5
10E4
10E3
10E2
10E1
MASS 23
MASS 40
MASS 39
TIME/S
100
200
300
400
500
600
700
800
900
1000
1100
1200

few hundred seconds of the profile. In this profile, the ^{23}Na and ^{39}K signals are no longer enhanced at the surface. Since there is no obvious reason to assume that these signals are not enhanced at the surface due to an artifact of the instrument, it must be concluded that there is a net reduction of the ^{23}Na and ^{39}K signals at the surface. These data then suggest that at the surface, the concentrations of such elements as sodium, potassium and silicon are lower than from well within the bulk of the specimen.

These SIMS profiles (Figure 7.3-2 and 7.3-3) have been normalized to reduce as many instrumental artifacts as possible. Four depth profiles for ^{28}Si relative to ^{27}Al that have been normalized are shown in Figure 7.3-4. The normalization procedure involves referencing the ^{28}Si signal to that for ^{27}Al. The ^{27}Al signal was constant throughout all of the SIMS profiles (altered and unaltered samples) and was therefore chosen as an internal reference. The data from each weathered surface were also referenced to those from the interior of the same grain in order to calculate the difference in ion intensity between the weathered surface and unweathered interior of each sample. This normalization procedure is similar to that which is described in detail in chapter 6. The time of sputtering in the profile (abscissa) has been converted to depth of analysis using the sputter rates presented above (sub-section 7.2.2, and chapter 6). Again, the reader is cautioned that the depth of analysis may be in error by as

much as 50 % due to difficulties in determination of a sputter rate for the weathered surfaces.

Figure 7.3-4 shows only the silicon data normalized to aluminum. The data for sodium, potassium and calcium are not presented here. In all profiles, the $^{28}Si/^{27}Al$ signals from the weathered surfaces are low at the surface, and then rise throughout the profile until the characteristic value for the unaltered material (Figure 7.3-4) is attained. This decrease in $^{28}Si/^{27}Al$ and the loss of sodium and potassium near the surface (see Figures 7.3-2 and 7.3-3) have been interpreted as arising from a zone of different composition. It is suspected that this zone was formed during weathering of the till.

Closer inspection of the profiles (Figure 7.3-4) reveals a few interesting trends. Of the three weathered samples presented, the change in secondary ion intensity ranges anywhere from approximately 30 to 80 %, while the depth of alteration varies somewhere between 300 and 800 Å. Also shown is that for the profile with the greatest reduction in the $^{28}Si/^{27}Al$ signal at the surface (sample 3), there is also the thickest layer of alteration. The converse of this is also true. The profile with the least reduction in the $^{28}Si/^{27}Al$ signal (sample 1) has the thinnest layer of alteration. In all the weathered samples analyzed (9 in total, 3 presented here), a relationship between the amount of depletion in secondary ion signal and depth of alteration is apparent. Therefore, it is strongly

Figure 7.3-4

Percentage change in the $^{28}Si/^{27}Al$ ratios versus the depth of analysis for one unweathered and three weathered oligoclase grains from the Plastic Lake Catchment, Ontario. The normalization procedure used tc obtain the $^{28}Si/^{27}Al$ ratios is given in chapter 6. Symbols: +, fresh plagioclase; ◇, ×, and *, three samples (1-3 respectively) of weathered plagioclase.

Si/Al OF FRESH & WEATHERED PLAGIOCLASE

FROM PLASTIC LAKE CATCHMENT

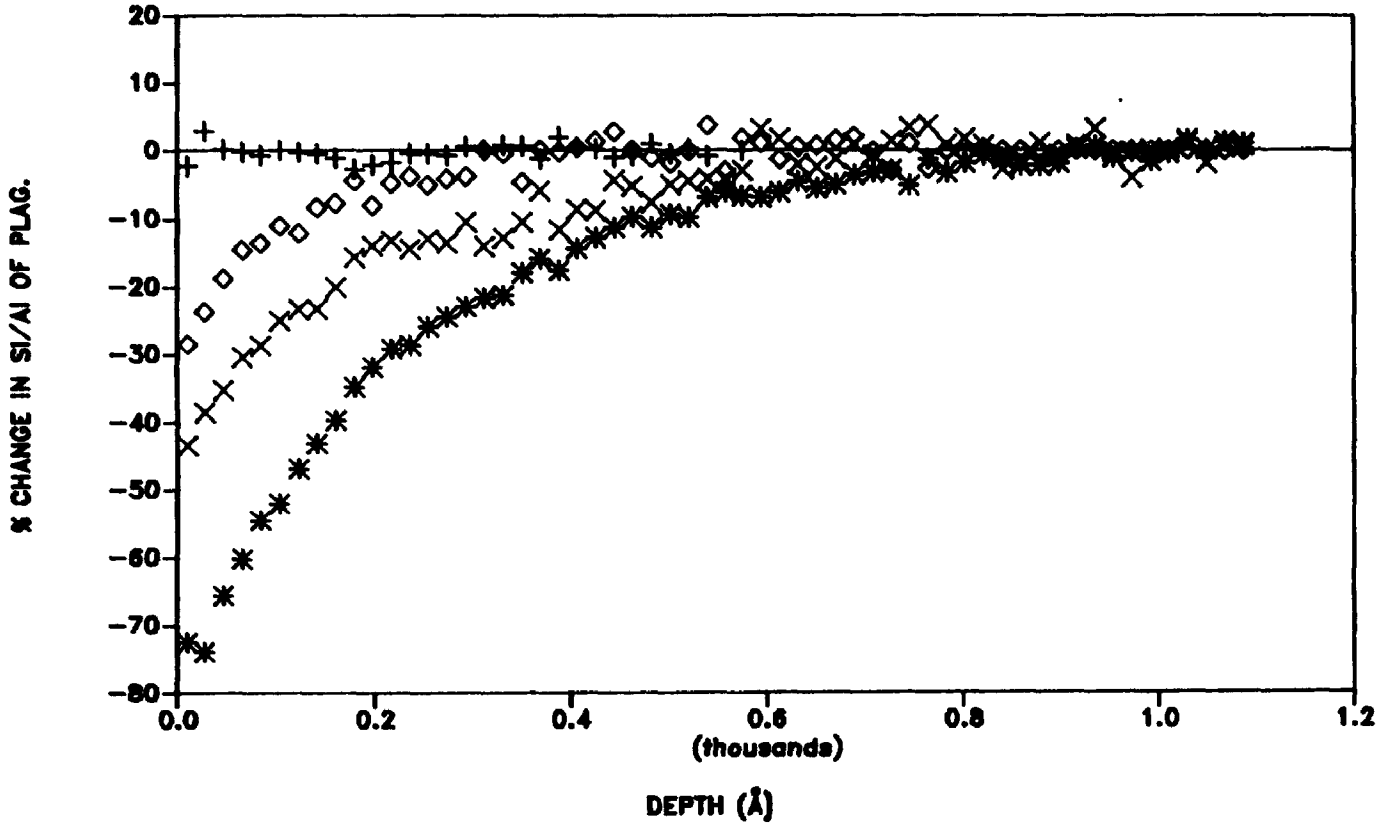

suggested that the various depths of alteration are indeed a result of the extent of the reactions taking place during weathering and not due to different rates of sputtering between samples.

The oligoclase surfaces have been exposed to various weathering processess for approximately 10,000 years. Comparing the profiles from the weathered and unweathered faces (see Figure 7.3-4), it is readily seen that a layer of composition different from that of the parent material exists on the weathered surfaces and not on the surfaces of the unaltered material. It is therefore reasonable to conclude that this altered zone is a result of weathering. Furthermore, this altered zone is more than likely a direct descendant of the plagioclase rather than the precipitation of secondary products from solution. The reasoning behind this is the lack of an abrupt change in the aluminum/silicon ratio between the altered and unaltered zones in the depth profiles (Figure 7.3-4). It should also be noted that within the limits of the SEM instrument used, the presence of crystalline precipitates was not observed. The relationship between composition and depth of the altered layer suggests; 1) that the altered zone originates from the plagioclase, and 2) that the process(es) responsible for the depletion (leaching) of certain elements from the surface is most effective at the mineral surface.

7.3.2 Comparison With Laboratory Dissolution and Other Recent Surface Studies

Depth profiling by SIMS has provided evidence for the formation of an altered layer at the plagioclase/solution interface of both naturally weathered (this chapter) and laboratory dissolved (chapter 6) plagioclase minerals. However, the nature of these altered layers is not consistent within the two sets of specimens analyzed. The layer formed on the naturally weathered samples is depleted in silicon and enriched (residually?) in aluminum, while the layers grown in the laboratory are enriched (residually?) in silicon and leached of aluminum. There is no reason to discredit either study. The results from laboratory dissolution apply to a given set of conditions, while the naturally weathered samples were exposed to an entirely different (somewhat uncertain) set of conditions altogether. The laboratory reactions may simply represent the initial stages of dissolution in nature.

Bond energy data[75] for the oxides of the constituent feldspar cations show that the weakest oxide bonds are for sodium, calcium and aluminum, while the silicon-oxygen bond is the strongest. If the initial rate of the release of elements from the feldspar to solution is to some extent dependent on the strenghts of the various bonds with oxygen, then the formation of a layer depleted in sodium, calcium and aluminum (residually enriched in silicon) is exactly what is expected. This will only hold true if the

concentrations of dissolved species are well below saturation. Thus, the results presented in chapter 6 for the laboratory dissolution of plagioclase are consistent with this theory. This relationship between bond strength and rate of release is easily applied to aluminum and silicon since they both reside in similar tetrahedral sites. Although the sodium and calcium oxide bonds are the weakest, extension of the above relationship is somewhat more difficult since they are bound differently than silicon and aluminum. Once this layer has begun to form, there is no question that the elements released from the fresh, unaltered plagioclase must diffuse through this layer, and Fick's first law of diffusion must hold. However, the question still remains as to whether or not diffusion through this leached layer is rate controlling in mineral (plagioclase) dissolution. This is not obvious from the depth profiles obtained.

It should also be added that this layer may not be thermodynamically stable relative to other crystalline phases. The suggestion has been made (M.F. Hochella Jr., personal communication) that these initial leached layers formed in the laboratory may disappear with time once they have been removed from the reactant solutions. Thus, surface analysis should be done immediately following removal of the specimen from solution (after drying of course; i.e. the sample must be free of moisture before being placed in any high or ultra high vacuum instrument).

As for the naturally weathered plagioclase, an entirely different set of weathering conditions were available during its 10,000 year history. The SIMS profiles do not reveal any evidence of the initial formation of a silicious residual layer. To assume that the aluminous layer is derived from the parent plagioclase material is in direct contradiction to the proposed relationship based on bond strength data. However, if concentrations of dissolved species are near saturation, which is highly probable in nature, then the derivation of this aluminous layer from the original plagioclase material is entirely possible. In fact, since the solubility of aluminum is lower than that for silicon, a layer residually enriched in aluminum should form throughout the course of time. Thus, the laboratory reaction conditions of this study may at best be representative of the very initial stages of dissolution in nature assuming no appreciable concentrations of dissolved species were present.

The ideas presented above regarding the formation of a leached layer are in accord with past data from the solution chemistry of dissolution reactions. That is, the formation of the leached layer may well be responsible for the parabolic reaction kinetics observed. The recently published surface analytical data[37,47,61] also coincide with this study. Although depth profiling was not possible in the experiments reported by Hochella et al.,[37] the surface data presented show evidence for the formation of an altered

layer derived from the parent material. Results from depth profiling studies by Mogk and Locke[47] and Petit et al.[61] also show evidence for the formation of an altered layer on the order of several hundreds of angstroms.

Using AES and depth profiling with an Ar^+ ion gun, Mogk and Locke[47] were able to show cation depleted layers (residually enriched in aluminum) for naturally weathered hornblende on the order of 1200 Å. Their profiles show a smooth progression in composition from the altered surface, through the leached zone and into the bulk of the unaltered mineral. Given these smooth profiles, they conclude that the altered layer is a direct descendant of the parent hornblende material, much like the case in this study. It should also be noted that this hornblende sample was collected from an area without an abundance of clay minerals.

The data presented by Petit et al.[61] support the results of this thesis (obtained by SIMS) as well as those presented by Mogk and Locke[47] (obtained by AES). However, the interpretation provided by Petit et al.[61] is altogether different. Petit et al.[61] used resonant nuclear reaction analysis to depth profile hydrogen in reacted diopside. This diopside was reacted in a solution of pH 2 for ~75 days. The depth of penetration of hydrogen was found to be on the order of 1000 Å. Petit et al.[61] state that the hydrogen is in the form of water, and that the majority of this water is strongly bonded within pores in the mineral.

In a SIMS analysis of the same sample by Schott and Petit,[72] the secondary ion intensity for the cations was reduced at the surface. However, this reduction in secondary ion intensity was not attributed to a cation depleted layer but rather was assigned to an increase in the porosity of the near surface region due to the introduction of water into the lattice (the interpretation is given in reference 61, while the SIMS results are from reference 72). However, for this interpretation to be correct, the secondary ion signal for all elements detected in the SIMS profiles must be reduced at the surface, and the depth that this reduction in signal is observed should be constant for all elements. This was not observed in any of the SIMS profiles in either of chapters 6 or 7. In the laboratory dissolution studies the silicon signal was consistent throughout (see Figure 6.3-3), while for the naturally weathered sample the aluminum signal was observed to be consistent from the surface, and well into the interior of the grain (see Figure 7.3-3). It is for this reason that the interpretation of Petit et al.[61] is not adopted for the results in this study.

7.4 CONCLUSIONS

The main conclusion of this study (chapters 6 and 7) and other recent studies is that altered layers presumably derived from the parent material exist on surfaces of weathered plagioclase (and other silicate) minerals. The

role of this layer in the dissolution process must now be addressed. Future studies in mineral dissolution should involve structural and better compositional characterization of the altered zone. It should be certain that elements released from the fresh plagioclase must diffuse through this layer according to Fick's first law of diffusion. At present, diffusion coefficients for material passing through this leached zone are not available. Whether or not diffusion of the plagioclase components through this layer control the rate of dissolution is yet to be determined. If diffusion through this layer is the rate controlling step, then the role of the layer is to inhibit dissolution and protect the mineral from further breakdown.

The composition and depth of this layer was found to be dependent upon the conditions present in the weathering environment. Laboratory reactions in acidic (pH 3.5) and near neutral (pH 5.7) solutions produced appreciable differences in the amount of cation depletion and thickness of the zone of alteration. More acidic conditions produced thicker layers with greater amounts of depletion. The constant flow reactors used for laboratory dissolution (with a flow rate of ~300 mL per day) do not permit the concentrations of the dissolved cations in solution to approach saturation or the build-up of any appreciable concentration gradients in solution. With these conditions a silicious residual layer was produced at the surface. In natural environments, it is more than likely that

significant concentration gradients were present at the plagioclase/solution interface and that the concentrations of certain species were often near saturation in the various weathering solutions. An aluminous residual layer was observed at the surface of oligoclase specimens from the Plastic Lake Catchment.

The use of surface analytical equipment alone is not sufficient for determining the presence of this layer. This is obvious from the work of Petrovic et al.[19] in which the presence of this leached layer was overlooked due to a few incorrect assumptions when interpreting the XPS data from reacted feldspar minerals (see chapter 6). The use of depth profiling techniques (SIMS, RNR and even AES with an Ar^+ ion gun) in conjuction with surface techniques (XPS and AES) has been able to provide evidence for the formation of an altered zone at mineral/solution interfaces during dissolution. In this particular study, the application of SIMS in conjunction with XPS and SEM has provided substantial evidence that this altered layer does indeed exist.

As a final remark, it is felt that the application of the SIMS technique to analysis of trace elements in minerals and studies in mineral dissolution has been explicitly demonstrated.

REFERENCES

1. M. A. Velbel, in "MAC Short Course Handbook, vol. 10" edited by M. E. Fleet (Selby Young Printing, London, 1984) p. 67.
2. S. S. Goldich, *Jour. of Geol.*, 46, 17 (1938).
3. C. D. Curtis, *Earth Surface Processes*, 1, 63 (1976).
4. Y. Kajiwara, *Annual Report of the Institute of Geosciences, University of Tsukuba*, 6, 81 (1980).
5. W. D. Keller, *Amer. Mineral.*, 39, 783 (1954).
6. W. H. Grant, *Clays and Clay Minerals*, 11, 65 (1963).
7. W. H. Grant, *Clays and Clay Minerals*, 12, 455 (1964).
8. J. P. Bryant and J. B. Dixon, *Clays and Clay Minerals*, 12, 509 (1964).
9. L. R. Gardner, *Amer. Mineral.*, 57, 294 (1972).
10. E. T. Cleaves, *Maryland Geol. Surv., Report of Invest.*, 25, (1974) 38pp.
11. H. Eswaran and W. C. Bin, *Soil Sci. Soc. of Amer. Jour.*, 42, 154 (1978).
12. M. A. Velbel, in "XIth International Congress on Sedimentology, Abstracts" 171 (1982).
13. M. A. Velbel, in "Petrologie des Alteration et des Sols, Volume 1," Memoires Sciences Geologiques, 71, 139 (1983).
14. H. Eswaran, G. Stoops and C. Sys, *Jour. Soil Sci.*, 28, 136 (1977).

15. J. Schott, R. A. Berner, and E. L. Sjoberg, *Geochim. Cosmochim. Acta*, 45, 2123 (1981).

16. R. M. Garrels and P. Howard, *Clays and Clay Minerals*, 6, 68 (1959).

17. E. Busenberg and C. V. Clemency, *Geochim. Cosmochim. Acta*, 40, 41 (1976).

18. R. Wollast, *Geochim. Cosmochim. Acta*, 31, 635 (1967).

19. R. Petrovic, R. A. Berner and M. B. Goldhaber, *Geochim. Cosmochim. Acta*, 40, 537 (1976).

20. H. C. Helgeson, *Geochim. Cosmochim. Acta*, 35, 421 (1971).

21. T. Pa es, *Geochim. Cosmochim. Acta*, 37, 2641 (1973).

22. C. W. Correns and W. von Engelhardt, *Chemie der Erde.*, 12, 1 (1938).

23. C. W. Correns, *Naturw.*, 28, 369 (1940).

24. C. W. Correns, *Clay Min. Bull.*, 4, 249 (1961).

25. C. W. Correns, *Clays and Clay Min.*, 10, 443 (1963).

26. M. Lagache, J. Wyart and G. Sabatier, *Compt. Rend.*, 253, 2296 (1961).

27. M. Lagache, *Soc. Francaise Mineralogy Cristallographie Bull.*, 88, 223 (1965).

28. M. Lagache, *Geochim. Cosmochim. Acta*, 40, 157 (1976).

29. R. A. Berner and G. R. Holdren Jr., *Geology*, 5, 369 (1977).

30. H. C. Helgeson, *Geochim. Cosmochim. Acta*, 36, 1067 (1972).

31. M. J. Wilson, *Soil Sci.*, 119, 349 (1975).

32. R. A. Berner and G. R. Holdren Jr., *Geochim. Cosmochim. Acta*, 43, 1173 (1979).

33. G. R. Holdren Jr. and R. A. Berner, *Geochim. Cosmochim. Acta*, 43, 1161 (1979).

34. J. Schott and R. A. Berner, *Geochim. Cosmochim. Acta*, 47, 2233 (1983).

35. D. L. Perry, L. Tsao and K. A. Gaugler, *Geochim. Cosmocim. Acta*, 47, 1289 (1983).

36. M. F. Hochella Jr., D. W. Harris, and A. M. Turner, *Amer. Mineral.*, 71, 1247 (1986).

37. M. F. Hochella Jr., H. B. Ponader, A. M. Turner and D. W. Harris, *Geochim. Cosmochim. Acta*, 52, 385 (1988).

38. J. M. Beusen and R. Gijbels, in "Leaching and Diffusion in Rocks and Their Weathering Products" edited by S. S. Augustithis (Theophrastus Publications S. A., Athens, 1983) p. 257.

39. G. M. Bancroft, J. B. Metson, R. A. Kresovic and H. W. Nesbitt, *Geochim. Cosmochim. Acta*, 51, 911 (1987).

40. S. Myhra, R. St. C. Smart and P. S. Turner, *Scanning Microsc.*, 2/2, 715 (1988).

41. H. W. Nesbitt and I. J. Muir, *Nature (London)*, 334/6180, 2641 (1988).

42. I. J. Muir, G. M. Bancroft and H. W. Nesbitt, *Geochim. Cosmochim. Acta*, in press (1988).

43. I. Lindau and W. E. Spicer, *J. Electron. Spectrosc. Relat. Phenom.*, 3, 409 (1974).

44. M. Klasson, A. Berndtsson, J. Hedman, R. Nilsson, R. Nyholm and C. Nordling, *J. Electron. Spectrosc. Relat. Phenom.*, 3, 427 (1974).

45. M. H. Koppelman and J. G. Dillard, in "International Clay Conference 1978" edited by M. M. Mortland and V. C. Farmer (Elsevier, Amsterdam, 1979) p. 153.

46. R. A. Berner, E. L. Sjoberg, M. A. Velbel and M. D. Krom, *Science*, 207, 1205 (1980).

47. D. W. Mogk and W. M. Locke III, *Geochim. Cosmochim. Acta*, 52, 2537 (1988).

48. G. R. Holdren Jr. and P. M. Speyer, *Geochim. Cosmochim. Acta*, 49, 657 (1985).

49. G. R. Holdren Jr. and P. M. Speyer, *Geochim. Cosmochim. Acta*, 51, 2311 (1987).

50. S. J. Talman and H. W. Nesbitt, *Geochim. Cosmochim. Acta*, 52, 1467 (1988).

51. L. Chou and R. Wollast, *Geochim. Cosmochim. Acta*, 48, 2205 (1984).

52. J. D. H. Strickland and T. R. Parsons, "A Practical Handbook of Seawater Analysis" (Bull. Fish. Res. Board of Canada, vol 167, 1987).

53. F. Freund, H. Wengeler, H. Kathrern, R. Knoebel, G. Oberheuser, G. C. Maiti, O. Reil, U. Knipping and J. Kotz, *Bull. Mineral.*, 106, 185 (1983).

54. R. A. Berner and J. Schott, *Amer. J. Sci.*, 282, 1214 (1982).

55. L. Chou and R. Wollast, *Am. J Sci.*, 285, 963 (1985).

56. P. C. Fung and G. G. Sanipelli, *Geochim. Cosmochim. Acta*, **46**, 503 (1982).

57. S. L. Brantley, S. R. Crane, D. A. Crerar, R. Hellmann and R. Stallard, *Geochim. Cosmochim. Acta*, **50**, 2349 (1986).

58. G. R. Holdren Jr. and P. M. Speyer, *Am. J. Sci.*, **285**, 994 (1985).

59. R. A. Berner, G. R. Holdren Jr. and J. Schott, *Geochim. Cosmochim. Acta*, **49**, 1657 (1985).

60. L. Chou and R. Wollast, *Geochim. Cosmochim. Acta*, **49**, 1659 (1985).

61. J. C. Petit, G. D. Mea, J. C. Dran, J. Schott and R. A. Berner, *Nature (London)* **334/6180**, 336 (1987).

62. J. F. Lovering, *Natl. Bur. Std. (U.S.) Spec. Publ.*, **427**, 135 (1975).

63. N. Shimizu, M. P. Semet and C. J. Allègre, *Geochim. Cosmochim. Acta*, **42**, 1321 (1978).

64. S. J. B. Reed, *Scanning*, 3, 119 (1980).

65. I. M. Steele, R. L. Hervig, I. D. Hutcheon and J. V. Smith, *Amer. Mineral.*, **66**, 526 (1981).

66. J. B. Metson, G. M. Bancroft, N. S. McIntyre and W. J. Chauvin, *Surface Interface Anal.*, **5**, 181 (1983).

67. J. B. Metson, G. M. Bancroft and H. W. Nesbitt, *Scanning Electron Microsc.*, **1985/II**, 595 (1985).

68. H. W. Nesbitt, J. B. Metson and G. M. Bancroft, *Chem. Geol.*, **55**, 139 (1986).

69. A. Havette, *Scanning Electron Microsc.*, 1985/II, 585 (1985).

70. L. A. Streit, R. L. Hervig and P. Williams, in "Microbeam Analysis" edited by A. D. Romig and W. F. Chambers (San Francisco Press, San Francisco, 1986) p. 91.

71. H. C. Helgeson, W. M. Murphy and P. Aagaard, *Geochim. Cosmochim. Acta*, 48, 2405, 1984.

72. J. Schott and J. C. Petit, in "Aquatic Surface Chemistry" edited by W. Stumm (Wiley, New York, 1987) p. 293.

73. V. E. Nash and C. E. Marshall, *Missouri Univ. Agr. Expt. Sta. Research Bull.*, 613, 36p. (1956).

74. V. E. Nash and C. E. Marshall, *Missouri Univ. Agr. Expt. Sta. Research Bull.*, 614, 36p. (1956).

75. G. V. Samsonov (editor) "The Oxide Handbook" (Plenum, Press, New York, 1973).